Automated Dust Storm Detection Using Satellite Images

ESAM ELMEHDE AMAR EL-OSSTA
BSc, MSc

PhD

2013

Automated Dust Storm Detection Using Satellite Images

Development of a Computer System for the Detection of Dust Storms from MODIS Satellite Images and the Creation of a New Dust Storm Database

By

ESAM ELMEHDE AMAR EL-OSSTA

BSc, MSc

A Thesis Submitted for the Degree of Doctor of Philosophy

2013

Digital Imaging

School of Computing, Informatics and Media

University of Bradford

Abstract

Dust storms are one of the natural hazards, which have increased in frequency in the recent years over Sahara desert, Australia, the Arabian Desert, Turkmenistan and northern China, which have worsened during the last decade. Dust storms increase air pollution, impact on urban areas and farms as well as affecting ground and air traffic. They cause damage to human health, reduce the temperature, cause damage to communication facilities, reduce visibility which delays both road and air traffic and impact on both urban and rural areas. Thus, it is important to know the causation, movement and radiation effects of dust storms. The monitoring and forecasting of dust storms is increasing in order to help governments reduce the negative impact of these storms. Satellite remote sensing is the most common method but its use over sandy ground is still limited as the two share similar characteristics. However, satellite remote sensing using true-colour images or estimates of aerosol optical thickness (AOT) and algorithms such as the deep blue algorithm have limitations for identifying dust storms. Many researchers have studied the detection of dust storms during daytime in a number of different regions of the world including China, Australia, America, and North Africa using a variety of satellite data but fewer studies have focused on detecting dust storms at night. The key elements of this present study are to use data from the Moderate Resolution Imaging Spectroradiometers on the Terra and Aqua satellites to develop more effective automated method for detecting dust storms during both day and night and generate a MODIS dust storm database.

Keywords: Brightness Temperature Difference, Neural Network, Pixel classification, Database, Decision Tree.

Acknowledgments

First of all I would like to praise the **God** who helped me to end this research, and reach this stage.

I would like to express my deepest gratitude and thankfulness to both of my supervisors **Dr Stanley Ipson** and Prof **Rami Qahwaji** for continuing to advise, encourage, suggest and orientate me towards the right path in my study research and to all those who contributed to me completing this thesis.

Thanks go to the University of Bradford and to the school of Computing, Informatics and Media for providing me with the facilities and the research resources required during the period of study.

I also wish to acknowledge the MODIS team for assisting me to understand how to deal with MODIS HDF file format and for much useful information to complete this work.

Also, I would like to record my great thanks and appreciation to my sponsor the **Libyan Centre for Remote Sensing and Space Science**, for affording me the opportunity of study and sponsoring my study.

Especially, I would like to give special thanks to my **parents**, my wife **Wafa**, my daughter **Fatima** and my son **Abd-Assami** and ask them for forgiveness for any inadvertent default on their rights during the period of study.

Dedication

To My Father And My Mother,

My Beloved Wife: Wafa,

My Lovely Daughter: Fatima,

My Lovely Son: Abd-Assami.

Table of Contents

List of Figures

List of Tables

List of Acronyms

AMSU	Advanced Microwave Sounding Unit
AOT	Aerosol Optical Thickness
BT	Brightness Temperature
BTD	Brightness Temperature Difference
DEP	Dust Enhancement Product
DSI	Dust Sand Index
DTC	Decision tree classifier
EDOS	EOS Data and Operating System
EOS	Earth Observing System
FAO	Food and Agriculture Organization
GUI	Graphic User Interface
HDF	Hierarchical Data Format
HDF-EOS	Hierarchical Data Format – Earth Observing System
INeN	Incremental neural network
LAADS	Level 1 and Atmosphere Archive and Distribution System
LWIR	Long-Wave Infrared
MISR	Multi-angle Imaging Spectroradiometer
ML	Maximum Likelihood
MLC	Maximum Likelihood Classifier
MODAPS	MODIS Adaptive Processing System
MODIS	Moderate Resolution Imaging Spectroradiometer
NDDI	Normalised Difference Dust Index
NDSI	Normalized Difference Snow Index
NIR	Near Infrared
NOAA	National Oceanic and Atmospheric Administration

NSIDC	National Snow and Ice Data Centre
OBC	On Board Calibrator
PCA	Principal Component Analysis
PNN	Probabilistic Neural Network
SDS	Sand and Dust Storm
SMIR	Short and Mid-Wave Infrared
SRB	Solar Reflectance Band
TIIDI	Thermal Infrared Integrated Dust Index
TIR	Thermal Infrared Data
TMI	TRMM Microwave Image
TOMS	Total Ozone Mapping Spectrometer
VIS	Visible
WMO	World Meteorological Organisation

List of Publications

- E. El-ossta, R. Qahwaji *and* S. Ipson “A new Approach for the detection of Dust Storms Using Multi-spectral MODIS bands” presented at the Mosharaka International Conference on Communications, Computers and Applications Amman Jordan, 2009.

- E. El-ossta, R. Qahwaji and S. Ipson “Detection of Dust Storms Using MODIS Reflective and Emissive bands”, has been published in the “IEEE Journal of *Selected Topics in Applied Earth Observations and Remote Sensing”.*

- E. El-ossta, R. Qahwaji and S. Ipson “Automatic Detection of Day and Night Time Dust Storms Using MODIS bands”, under preparation for publication in the “IEEE Journal of *Selected Topics in Applied Earth Observations and Remote Sensing”.*

CHAPTER ONE

1. INTRODUCTION

1.1 BACKGROUND AND MOTIVATION

Dust storms are a common natural phenomena that occur widely around the world in arid and semi-arid regions especially in subtropical latitudes, including North Africa, northern China, Australia, the Arabian Desert, and Turkmenistan, which have worsened during the last decade [1, 2]. Desert landscapes and human activities in semi-arid areas are the most important sources of dust storms [3]. Scientifically, soil particles of size about 0.6-1mm are described as sand, while soil particle of size less than about 0.6 mm are described by dust. In practice only those dust particles of size less than 0.1 mm are transported by the wind and dust storms are the product of the collective transport of soil particles by wind [3]. The World Meteorological Organisation (WMO) protocol has classified dust storms according to their visibility into the following categories.

- Drifting Dust: The visibility within these kinds of the dust events is not less than 10 km. This kind of dust is widespread dust and is not raised more than two metres.

- Blowing Dust: This reduces the visibility to between 1 km and 10 km and is caused by a moderate wind which raises dust to a moderate height above the ground.
- Dust Storm: This reduces the visibility to between 200 m and 1000 m and occurs when a strong wind lifts a large quantity of dust particles into the atmosphere
- Severe Dust Storm: This reduce the visibility to less than 200 m and occurs when a very strong wind lifts a very large quantity of dust particles into the atmosphere [4].

Strong winds above dry land are the most important reason for the occurrence of dust storms and the largest source of dust storms in the world is the Sahara region, which is a source of dust deposited over much of Western Europe. Saharan dust storms are also blown westwards, depositing dust in the Atlantic Ocean and as far west as the United States and the West Indies. The arid and semi-arid region around the Arabian Sea is another principal source of global dust and contributes to dust sediment in the Arabian Sea. Many of the dust storms from China contribute to dust deposition in the Pacific Ocean. Fine dust can be transported at altitudes up to 6 km and move over distances up to 6,000 km [3]. Saharan dust storms transport large quantities of material across the African continent and beyond and can be both a cause of extensive disruption and hazard to health and also an important source of nutrients to both land and ocean [5]. Since 1900, 17 dust storms have swept over Great Britain from the Sahara. Each event transported about 10 million tons of dust to

Great Britain, according to research by the Geology Faculty of Oxford University [3].

Dust storms have a number of impacts upon both humans and the environment including the loss of many young plants, resulting in a loss of productivity. However, most of the impacts of dust storms are within the atmosphere, affecting air temperatures by absorption and reflection of solar radiation and affecting cloud formation and convection activity. The spread of the African dust in the air layer over the Sahara desert can cause changes in the intensity of the hurricane peak in the North Atlantic. Large quantities of dust deposited on ice surfaces have the effect of lowering snow reflection and amplifying snowmelt. There are many studies which show that dust transported long distances can affect geochemical conditions at long distances from dust sources. Reducing visibility to a few metres is only one of the most noticeable effects. This loss of visibility can be a major hazard effecting both civilian and military traffic and aircraft [6]. Figure 1-1 shows an Egyptian airplane which crashed near Tunis, Tunisia, killing 18 of the 60 people on board. The cause of this air crash was the Saharan dust storm on May 7th, 2002. Dust storms also reflect sunlight back into space, reducing the amount of energy reaching the surface resulting in cooling.

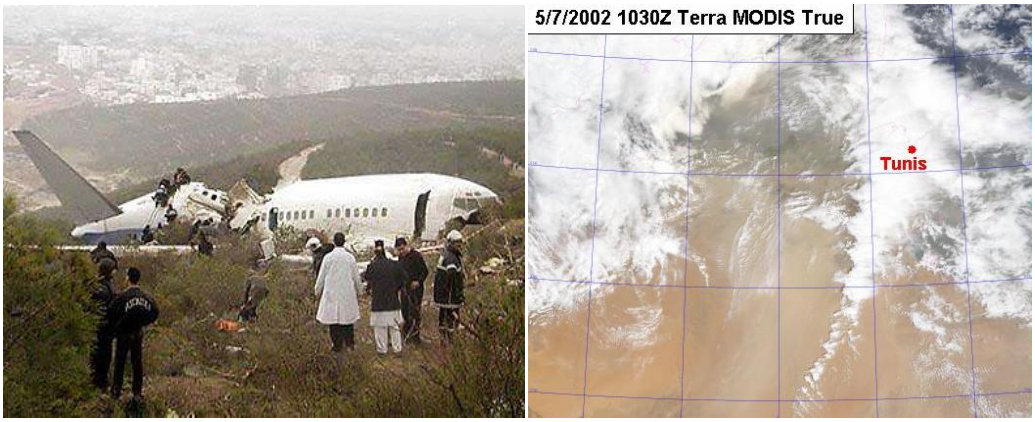

Figure 1-1 Saharan dust storm caused air crash near Tunis

Dust particles impacting on human health, causing a wide range of respiratory disorders including chronic bronchitis and lower respiratory illness. Dust emissions from dried lake basins which introduce fine particles, including salts and chemical herbicides into the atmosphere generate a suite of health impacts and not just respiratory complaints, but also other serious illnesses. Dust storms can transport allergens, including bacteria and fungi, and it could be that an outbreak of meningococcal meningitis in the Sahel region of Africa and the spread of Coccidioidomycosis in the southwest United States are related to dust storm activity [6]. In China, dust storms are considered a risk factor in hospitals for respiratory and cardiovascular complains [6].

Dust storms are considered one of the main causes of desertification [3]. The Middle East, Taklamakan, Southwest Asia, Central Australia, the Etosha and Mkgadikgadi pans of Southern Africa, the Salar de Uyuni of Bolivia, and the Great Basin in the USA are known as dust storm source regions, but the Sahara is the biggest single source of dust storms. The Sahara is the main source of dust sedimentation into the Mediterranean Sea and neighbouring countries [6].

1.2 PROBLEM IDENTIFICATION

While dust storms are only one of many natural hazards, monitoring and tracking them has become very important in recent years to help governments to alleviate the consequences of these storms. At the present time there are only two main methods available for monitoring dust storms. The first is ground-based measurements, and the second is satellite based remote sensing technology, in which interest is increasing [7] because ground based measurements cannot meet the requirements of monitoring and tracking dust storms very well.

Satellite remote sensing is likely to become the primary approach for the detection of dust storms [1] because of the potential advantages to using this technology, including flexible coverage of wide areas and continuous or frequent monitoring of the earth. On the other hand, satellite remote sensing is indirect, and methods based on analysis of true-colour images or calculations of aerosol optical thickness (AOT) by the deep blue algorithm, for example, are limited. However, in principle, the severity of dust storms, the areas they affect and changes in intensities can be monitored using remotely sensed images [7]. For these reasons, many researchers have proposed methods to distinguish dust storms from clouds, ground and water surfaces using images in many different spectral bands obtained from various instruments [1, 2, 7-9]. However, the detection of dust storms is difficult because they share some characteristics with clouds which can make it very hard to distinguish them in some spectral bands [2]. Furthermore, the characteristics of dust storms and ground sand are similar, which makes it difficult to discriminate between them. There is also

difficulty in detecting dust storms during the night. All the previous work on dust storm detection focused on detecting dust storms over one type of ground surface and most concentrated on detecting dust storms during the day.

1.3 OBJECTIVES

The objective here is to address long standing problems in the automatic detection of dust storms and develop techniques and procedures to efficiently recognize dust storms using the Moderate Resolution Imaging Spectroradiometers (MODIS) on board the NASA Terra and Aqua satellites. Furthermore, there is a need for generating a MODIS dust storm database as there is no such database for new further studies, particular for monitoring and tracking dust storms.

To achieve this objective, the following sub-objectives are addressed:

- Statistical analysis for dust storm detection is pursued. The resulting analysis will allow better understanding of suitable MODIS bands for detecting dust storm from sandy land. The analysis could also be utilized in classifications and post-processing.
- The generation of manually detected dust storm data, as there is no dust storm ground truth data available for validating dust storm detection methods.
- The development of a new method for dust storm detection using thresholds. The target technique aims to be simple and produce binary images of dust storms.

- The development of a new method for dust storm detection during the night using a threshold method.
- The development of an efficient detection technique using a neural network to lead potentially to more accurate detection of dust storms during the day.
- The development of an efficient detection technique using a neural network to lead potentially to more accurate detection of dust storms during both day and night time.
- The generation of an automated system to update a MODIS dust storms database. This would involve creating a MODIS dust storm database as there is no such database available. This could then be used for the monitoring and tracking of dust storms.

1.4 OUTLINE OF THE THESIS

The remainder of this thesis is structured as follows. Chapter 2 starts by providing an overview of the relevant properties of the data available from the MODIS instrument and how it can be accessed, which helps to inform the subsequent review. This is followed by a literature review of previous work on dust storm detection, which provides definitions, context, and an understanding of the previous research. The review gives some examples of how different types of techniques are being used in this field. It reviews the state of the art, recent advances and the limitations of dust storm detection.

Chapter 3 presents two threshold based methods for detecting dust storms, starting with an analysis of the emissivities and the brightness

temperatures of objects seen in MODIS images in order to generate the best brightness temperature difference (BTD) to distinguish between dust storms and sandy land. One method is for daytime use only, while the other is for both day and night time use.

Chapter 4 presents two methods for detecting dust storms using Neural Networks. The methods differ in the sets of pixel features which are input into the Neural Networks in order to classify pixels as dust storm or not. The first feature set includes the brightness temperature differences calculated from two pairs of MODIS spectral bands and the reflectances from three other bands. This method is limited to daylight use only and so the second method uses a feature set which includes four brightness temperature differences and one other brightness temperature to achieve both day and night time classification of pixels as to the presence or absence of a dust storm.

Chapter 5 presents and compares two methods for classifying the pixels of MODIS Images into six classes: cloud, dust storm, water, vegetation, land and snow. The first method employs a decision tree method, and the second a neural network. Both methods use the same feature set, which includes two brightness temperatures and three other combinations of spectral bands, defined in previous work.

Chapter 6 presents an automated dust storm database system based on MODIS data which works during both day and night time, using a neural network. The feature vector used for the pixel classification is the one presented in Chapter 4.

The contributions of this research work to the field of dust storm detection are presented in Chapter 7, together with some possible future research directions in related areas.

CHAPTER TWO

2. LITERATURE REVIEW OF EXISTING WORK

2.1. INTRODUCTION

Much of this chapter reviews existing work using data from the Moderate Resolution Images Spectrometer (MODIS). To aid this review, the chapter first continues in Section 2.2 with an overview of the MODIS instrument, its wavelength bands (and their intended uses), the products provided and the MODIS tools provided. The chapter then presents previous work on dust storm detection divided into two parts. Section 2.3.1 includes studies used MODIS data for dust storm detection, and Section 2.3.2 includes studies using data from other instruments. Section 2.4 describes some previous work on classification of the content of satellite images. The chapter ends with some conclusions in Section 2.5.

2.2. OVERVIEW OF MODIS INSTRUMENT

The Moderate Resolution Imaging Spectrometer (MODIS) scientific instrument is part of the NASA Earth observing System (EOS) mission. MODIS was launched onboard the Terra and Aqua satellites in December 1999 and May 2002 respectively. Both satellites have been working well except for band 6 (1.628 µm – 1.652 µm) of the Aqua satellite which is either non-functional or noisy. The MODIS instrument provides calibrated, high radiometric-sensitivity

(12 bit) data, in 36 spectral bands covering wavelengths from 0.4 µm to 14.4 µm in the visible (VIS), near infrared (NIR), short and mid-wave infrared (SMIR), and long-wave infrared (LWIR). Furthermore, the MODIS sensor has three different nadir ground spatial resolutions: 250m (bands 1 and 2), 500m (bands 3 - 7), and 1000m (bands 8 - 36). Table 2-1 provides some information on the MODIS bands and their intended usage. In the long track direction, there are 40 detectors per band for bands 1 and 2, 20 detectors per band for bands 3 - 7, and 10 detectors per band for bands 8 - 36 [10]. A double-sided scan mirror providing ±55-degree scanning pattern at the EOS orbit of 705 km, achieves a 2,330-km swath and provides near-daily imaging capability, complementing the spectral, spatial, and temporal coverage of the other research instruments [11]. MODIS data is intended to help improve understanding of global dynamics and processes occurring on land, in the oceans, and in the lower atmosphere [12]. The Terra satellite orbits the Earth, crossing the equator from north to south in the morning, while the Aqua satellite orbits the earth crossing the equator from south to north in the afternoon. MODIS data are transferred to ground stations in White Sands, New Mexico, and then sent to the Data and Operation System (EOS) at the Goddard Space Flight Centre. The MODIS instrument has been designed to provide improved monitoring for land, ocean, and atmosphere research. Spectral channels for improved atmospheric and cloud characterization have been included to permit both the removal of atmospheric effects on surface observations and the provision of atmospheric measurements [11].

Table 2-1 Properties of the MODIS bands

Band	Wavelength (nm)	Resolution (m)	Key Use	Primary nature
1	620-670	250	Absolute Land Cover Transformation, Vegetation Chlorophyll	Reflectance Solar Bands
2	841-876	250	Cloud Amount, Vegetation Land Cover Transformation	
3	459-479	500	Soil/Vegetation Differences	
4	545-565	500	Green Vegetation	
5	1230-1250	500	Leaf/Canopy Differences	
6	1628-1652	500	Snow/Cloud Differences	
7	2105-2155	500	Cloud Properties, Land Properties	
8	405-420	1000	Chlorophyll	
9	438-448	1000	Chlorophyll	
10	483-493	1000	Chlorophyll	
11	526-536	1000	Chlorophyll	
12	546-556	1000	Sediments	
13h	662-672	1000	Atmosphere, Sediments	
13l	662-672	1000	Atmosphere, Sediments	
14h	673-683	1000	Chlorophyll Fluorescence	
14l	673-683	1000	Chlorophyll Fluorescence	
15	743-753	1000	Aerosol Properties	
16	862-877	1000	Aerosol Properties, Atmospheric Properties	
17	890-920	1000	Atmospheric Properties, Cloud Properties	
18	931-941	1000	Atmospheric Properties, Cloud Properties	
19	915-965	1000	Atmospheric Properties, Cloud Properties	
Band	**Wavelength (μm)**	**Resolution (m)**	**Key Use**	**Primary nature**
20	3.660-3.840	1000	Sea Surface Temperature	Thermal Emissive Bands
21	3.929-3.989	1000	Forest Fires & Volcanoes	
22	3.929-3.989	1000	Cloud Temperature, Surface Temperature	
23	4.020-4.080	1000	Cloud Temperature, Surface Temperature	
24	4.433-4.498	1000	Cloud Fraction, Troposphere Temperature	
25	4.482-4.549	1000	Cloud Fraction, Troposphere Temperature	
26	1.360-1.390	1000	Cloud Fraction (Thin Cirrus), Troposphere Temp.	Reflectance Solar Band
27	6.535-6.895	1000	Mid Troposphere Humidity	Thermal Emissive Bands
28	7.175-7.475	1000	Upper Troposphere Humidity	
29	8.400-8.700	1000	Surface Temperature	
30	9.580-9.880	1000	Total Ozone	
31	10.780-11.280	1000	Cloud Temperature, Forest Fires & Volcanoes, Surface Temp.	
32	11.770-12.270	1000	Cloud Height, Forest Fires & Volcanoes, Surface Temperature	

33	13.185-13.485	1000	Cloud Fraction, Cloud Height	
34	13.485-13.785	1000	Cloud Fraction, Cloud Height	
35	13.785-14.085	1000	Cloud Fraction, Cloud Height	
36	14.085-14.385	1000	Cloud Fraction, Cloud Height	

2.2.1. MODIS PRODUCTS AND APPLICATIONS

From the raw data, MODIS provides over 40 standard data products, in the Hierarchical Data Format – Earth Observing System (HDF-EOS) [13], intended to help scientists studying Earth's land, ocean and atmosphere [14]. MODIS data have several levels of maturity. Scientists have used MODIS products in a great variety of applications, including oceanography, biology, and atmospheric science. The next sub-section provides some details of individual products, where names starting with MO or MY indicate the Terra and Aqua satellites respectively [15].

2.2.1.1. MODIS CALIBRATION PRODUCTS

MODIS Calibration products (Level 1A, Level 1B and geo-location) are a precursor to every geophysical science product [16].

- **Level-1A Radiance Counts (MOD01, MYD01)**

  MODIS Level 1A data is produced by the MODIS Adaptive processing System (MODAPS) and sent to the Level 1 and Atmosphere Archive and Distribution System (LAADS) (http://modis.gsfc.nasa.gov/data/). Level 1A processing includes packaged and reformatted raw instrument data from Level 0 MODIS data received from the EOS data and operating system (EDOS) [17]. Raw Radiance Counts data set includes Level 1A Swath (MOD01 or MYD01) data, raw instrument engineering and spacecraft ephemeris data for all 36 MODIS

channels, which are used as inputs for geo-location, calibration, and processing. For indicating missing or bad pixels and instrument modes, quality indicators have been added. This product includes all MODIS digitized (counts) data for all bands, spatial resolutions, time covered, all detector views, and all engineering and ancillary data [15]. MODIS scan data during Level 1A processing includes eight fields which are used to store the earth location information for each MODIS spatial element. These fields are: geodetic latitude, geodetic longitude, height above the Earth ellipsoid, satellite zenith angle, satellite azimuth, range to the satellite, solar zenith angle and solar azimuth [17].

- **Level – 1B Calibrated Geo-located Radiances**

MODIS Level 1A sensor counts (MOD 01) are used to generate, calibrated and geo-located radiances (in $W/(m^2.\mu m.sr)$) for 36 bands and presented as Level 1B data. MODIS Level 1B calibration code generates four product files: Calibrated Earth View data at 250m resolution MOD02QKM and MOD02QKM for Terra and Aqua respectively; Calibrated Earth View data at 500m resolution including the 250m resolution bands aggregated to 500m resolution MOD02HKM and MOD02HKM for Terra and Aqua respectively; Calibrated Earth View data at 1km resolution including the 250m and 500m resolution bands aggregated to 1km resolution MOD021KM and MOD021KM for Terra and Aqua respectively; and On Board Calibrator (OBC) and Engineering Data MOD02OBC and MYD02OBC for Terra and Aqua respectively which contains on board measurements in the Space View, Black Body, Spectro-Radiometric

Calibration Assembly and Solar Diffuser Sectors, and additional engineering data [18]. The reflectance and the radiance can be generated from the solar reflective bands (1-19 and 26) using the Level 1B scaled integer representation. Quality flags, error estimates, and calibration data are all provided in Level 1B data files. Also, Brightness Temperature (BT) data (that assumes the emitting surface is a black body) can be generated using thermal emissive bands (20-25 and 27-36) [12, 19].

- **Geolocation Data**

The MODIS Geolocation product (MOD03) consists of information on geodetic coordinates (latitude, longitude, and height), and the sun and satellite sensors properties (sensor zenith angles, sensor azimuth angles, slant ranges, solar zenith angle, solar azimuth angles) and geolocation flag values for each MODIS 1-km sample. By comparison, MODIS level 1B 250m and 500m data sample include just information about latitude and longitude. Spacecraft attitude and orbit, instrument telemetry, and a digital elevation model are used to determine the geolocation fields [20].

2.2.1.2. MODIS ATMOSPHERIC PRODUCTS

MODIS atmospheric products include five data products in Level 2 and three data products in Level 3. The level 2 products contain geophysical parameters for aerosols (optical properties and mass concentration), water vapour, clouds (physical and optical properties), atmospheric profiles (temperature, moisture and total ozone and stability indices) and cloud mask. The Level 3 products contain daily, weekly and monthly statistics for the Level 2

science parameters [21]. The MODIS Atmospheric algorithm using twenty six MODIS bands to create atmospheric products [22]. Figure 2-1 summarises the MODIS atmosphere data processing architecture and products. Appendix A shows more details about MODIS atmospheric products

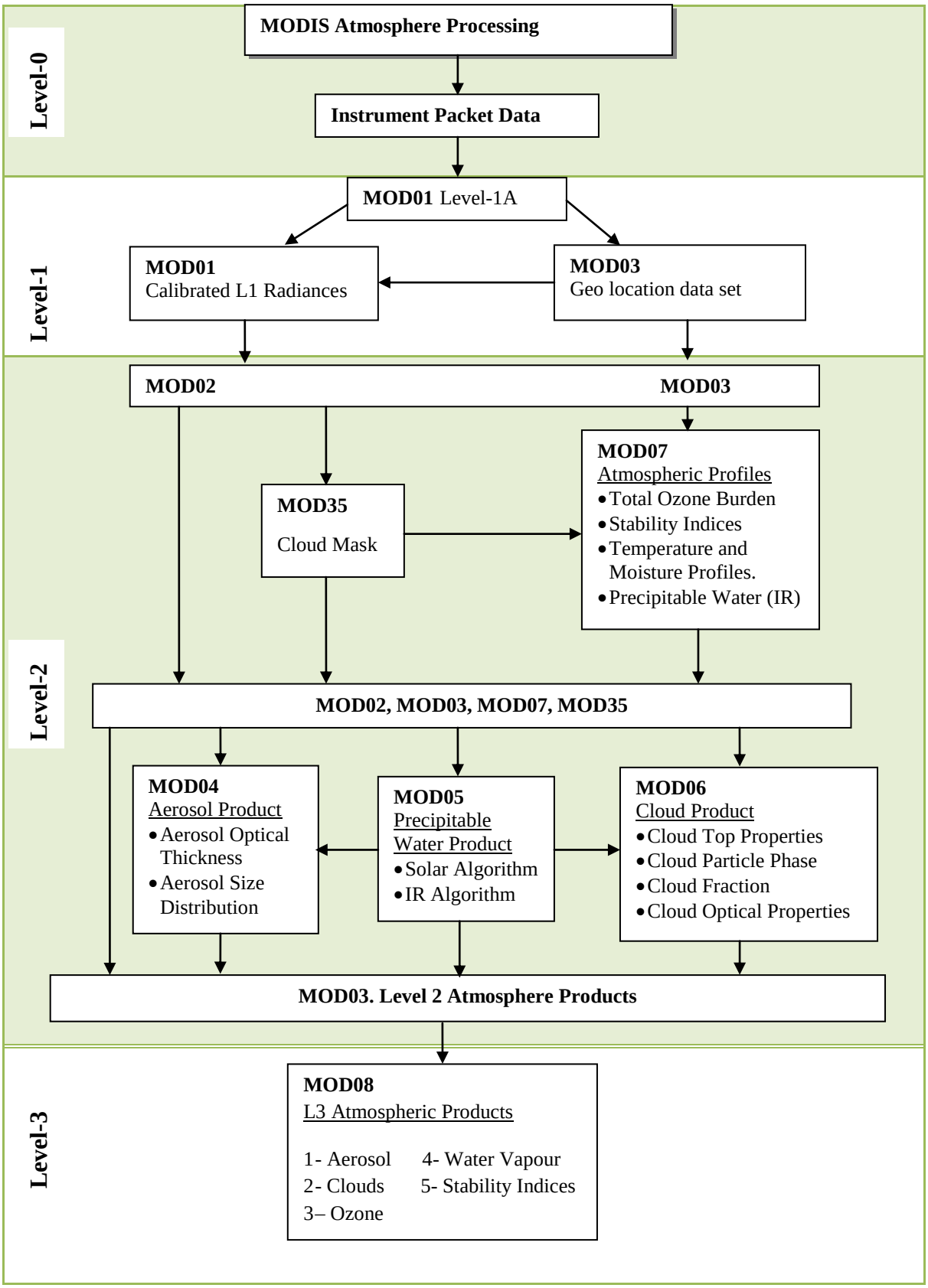

Figure 2-1 MODIS atmosphere data processing architecture and products [22].

- **Cloud Mask (**MOD35 for Terra and MYD35 for Aqua**)**

The goal of the cloud mask (MOD35) algorithm is to classify each pixel as confidently clear, probably clear, probably cloudy, or cloudy. The cloud mask is generated at 250m and 1000m resolutions [23] and consists of 48 bits of output that include information on individual cloud test results. However, there is no need to process all 48 bits when applying the mask; only the first 8 bits may be necessary. Figure 2-2(B) shows an example of cloud mask of MODIS image captured by Aqua satellite over North Africa on 2005 where the red flag pixel is confidently clear, yellow is probably clear, light blue is probably cloud and dark blue is cloud. However, the MODIS cloud mask has some limitations; firstly it is not accurate for detecting cloud when there is a dust storm as can be clearly seen in Figure 2-2(B), secondly the MODIS cloud mask takes two hours to become available, which leads to difficulty monitoring events such as dust storms.

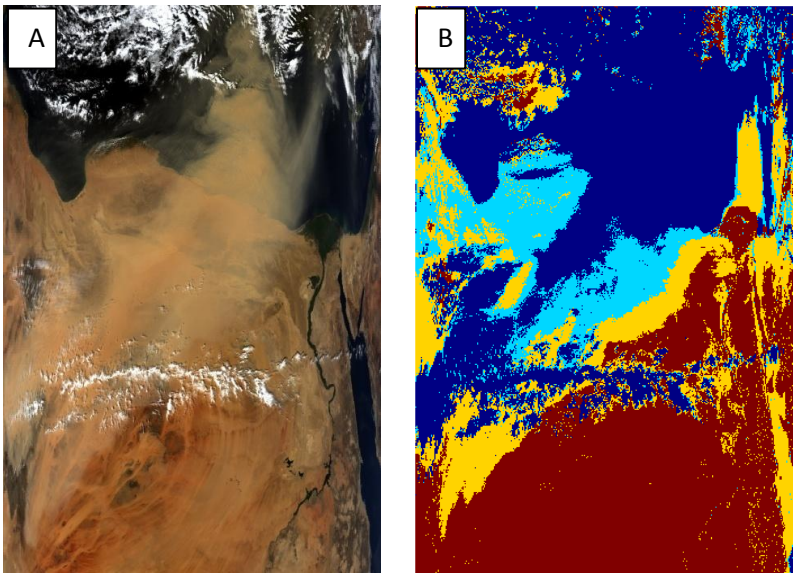

Figure 2-2 (A) is a true colour image captured by Aqua over North Africa and (B) is the relative cloud mask.

The cloud mask algorithm uses a series of threshold tests applied to the 19 MODIS bands 1, 2, 4, 5, 6, 7, 17, 18, 19, 20, 22, 26, 27, 28, 29, 31, 32, 33, and 35 to identify the presence of clouds in the instrument field of view [23]. The cloud mask requires several ancillary data inputs: sun angle, azimuthal angle, viewing angle, land/water map at 1 km resolution and topographic elevation above mean sea level obtained from MOD03 (geolocation fields), and ecosystems global 1 km map of ecosystems based on the Olson classification system, and Daily NISE snow/ice map provided by NSIDC (National Snow and Ice Data Centre), and daily sea ice concentration product from NOAA [23].

The cloud mask is not the only cloud product from MODIS; several Principal Investigators have responsibility to deliver algorithms for various additional cloud parameters, such as water phase and altitude. The specific tests executed are functions of surface type, Including land, coastal, water, snow/ice and desert, and are different during the day and night [22]. The cloud mask output also includes results from particular cloud detection tests. Table 2-2 gives a description of MODIS cloud mask product bits.

Table 2-2 File specification for the 48-bits MODIS cloud mask [23]

BIT	DESCRIPTION KEY	RESULT
0	Cloud Mask Flag	0 = not determined 1 = determined
1-2	Unobstructed FOV Quality Flag	00 = cloudy 01 = uncertain clear 10 = probably clear 11 = confident clear
PROCESSING PATH FLAGS		
3	Day/Night Flag	0=Night / 1= Day

4	Sun glint Flag	0 = Yes / 1 = No
5	Snow / Ice Background Flag	0 = Yes/ 1 = No
6-7	Land / Water Flag	00 = Water 01 = Coastal 10 = Desert 11 = Land
ADDITIONAL INFORMATION		
8	Non-cloud obstruction Flag (heavy aerosol)	0 = Yes / 1 = No
9	Thin Cirrus Detected (near infrared)	0 = Yes / 1 = No
10	Shadow Found	0 = Yes / 1 = No
11	Thin Cirrus Detected (infrared)	0 = Yes / 1 = No
12	Spare (Cloud adjacency) (post launch)	(Post launch)
1km CLOUD FLAGS		
13	Cloud Flag - simple IR Threshold Test	0 = Yes / 1 = No
14	High Cloud Flag - CO2 Threshold Test	0 = Yes / 1 = No
15	High Cloud Flag - 6.7 µm Test	0 = Yes / 1 = No
16	High Cloud Flag - 1.38 µm Test	0 = Yes / 1 = No
17	High Cloud Flag - 3.9-12 µm Test	0 = Yes / 1 = No
18	Cloud Flag - IR Temperature Difference	0 = Yes / 1 = No
19	Cloud Flag - 3.9-11 µm Test	0 = Yes / 1 = No
20	Cloud Flag - Visible Reflectance Test	0 = Yes / 1 = No
21	Cloud Flag - Visible Ratio Test	0 = Yes / 1 = No
22	Clear-sky Restoral Test- NDVI in Coastal Areas	0 = Yes / 1 = No
23	Cloud Flag -7.3-11 µm Test	0 = Yes / 1 = No
ADDITIONAL TESTS		
24	Cloud Flag – Temporal Consistency	0 = Yes / 1 = No
25	Cloud Flag - Spatial Consistency	0 = Yes / 1 = No
26	Clear Sky Restoral test	0 = Yes / 1 = No
27	Cloud Test – Night Ocean Variability Test	0 = Yes / 1 = No
28	Suspended Dust Flag	0 = Yes / 1 = No
29-31	Spares	0 = Yes / 1 = No
250m CLOUD FLAG - VISIBLE TESTS		
32	Element(1,1)	0 = Yes / 1 = No
33	Element(1,2)	0 = Yes / 1 = No
34	Element(1,3)	0 = Yes / 1 = No
35	Element(1,4) 0 = Yes / 1 = No	0 = Yes / 1 = No
36	Element(2,1) 0 = Yes / 1 = No	0 = Yes / 1 = No
37	Element(2,2) 0 = Yes / 1 = No	0 = Yes / 1 = No
38	Element(2,3) 0 = Yes / 1 = No	0 = Yes / 1 = No
39	Element(2,4) 0 = Yes / 1 = No	0 = Yes / 1 = No
40	Element(3,1) 0 = Yes / 1 = No	0 = Yes / 1 = No
41	Element(3,2) 0 = Yes / 1 = No	0 = Yes / 1 = No
42	Element(3,3) 0 = Yes / 1 = No	0 = Yes / 1 = No
43	Element(3,4) 0 = Yes / 1 = No	0 = Yes / 1 = No
44	Element(4,1) 0 = Yes / 1 = No	0 = Yes / 1 = No
45	Element(4,2) 0 = Yes / 1 = No	0 = Yes / 1 = No
46	Element(4,3) 0 = Yes / 1 = No	0 = Yes / 1 = No
47	Element(4,4) 0 = Yes / 1 = No	0 = Yes / 1 = No

2.2.1. WHY MODIS

Many studies have concentrated on the detection, monitoring, mapping and assessment of various natural disasters (fire, snow, dust storm, flood etc) using various instruments and satellites. The MODIS instrument provides calibrated high radiometric sensitivity (12 bit) in 36 spectral bands covering wavelengths from 0.4 µm to 14.4 µm and has three different nadir ground spatial resolutions: 250m, 500m and 1000m. In the long track direction, there are 40 detectors per band for bands 1 - 2, 20 detectors per band for bands 3 - 7, and 10 detectors per band for bands 8 – 36. The MODIS instrument has been designed to provide improved monitoring for land, ocean, and atmosphere two times a day [10]. Table 2-3 illustrates the differences between MODIS satellites and other available satellites.

Table 2-3 Differences between MODIS (Terra/Aqua) and instruments on other satellites

Satellite	Orbital Type	Spatial Resolution	Frequency	Field of View	Number of Bands	Cost to User
MTSAT, FY-2C, METEOSAT	Geostationary	1-5 km	Every 30 minutes	Hemisphere	5 4 12	free
NIAA , FY-2B	Polar	1 km	2 times a day	2500 km	6 14	free
Landsat, SPOT, CBERS	Polar	2-30 m	Every 16 days	60-180 km		costly
IKONS, Quickbird	Polar	0.6-1 m	Every 16 days	11 km	5 4	costly
MODIS Terra/Aqua	Polar	250-1Km	2 times a day	2300 km	36	free

2.2.2. SOFTWARE SYSTEMS TO READ AND VIEW HDF FILES

MODIS data is not just one image file but a set of image files and scientific data files that are saved in hierarchical data format (HDF file type). Therefore, software systems are provided for reading and displaying the HDF

files for the different purposes listed below. There is more information about these software systems in Appendix A.

- **MODIS REPROJECTION TOOL**
- **MODIS REPROJECTION TOOL SWATH**
- **HDF-EOS WEB-BASED SUB-SETTER**
- **SPOT - SUBSETTABILITY CHECKER**
- **MODIS LDOPE TOOLS**
- **HDFLOOK**
- **HDF-EOS TO GEOTIFF CONVERTER**
- **HREPACK**
- **HDF-EOS TO GEOTIFF CONVERTER**
- **HREPACK**
- **MATLAB**

MATLAB is widely used in research, because it includes an enormous number of tools, has a flexible easy to use user interface and has a useful help library. It also provides access to HDF files. In this study the MATLAB HDF, image processing and neural network tools have been used for detection of dust storms as described below.

HDF Tools in MATLAB provide two options for reading HDF files. The first uses a GUI to browse for HDF files, as shown in Figure 2-3.

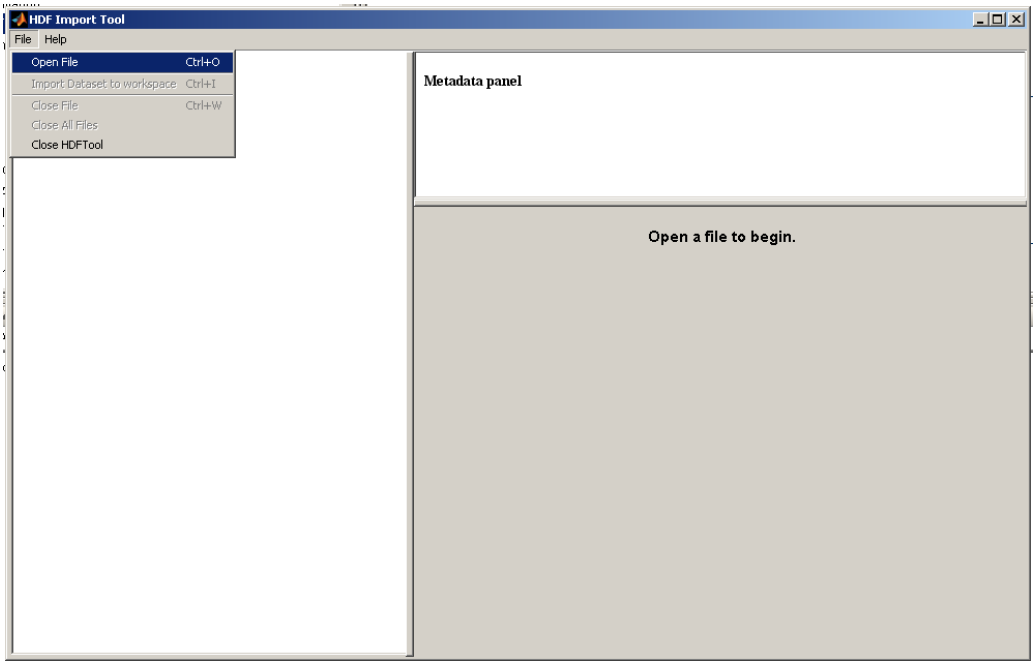

Figure 2-3 HDF GUI Tool

After reading an HDF file, the HDF Tool provides information about the file as shown in Figure 2-4.

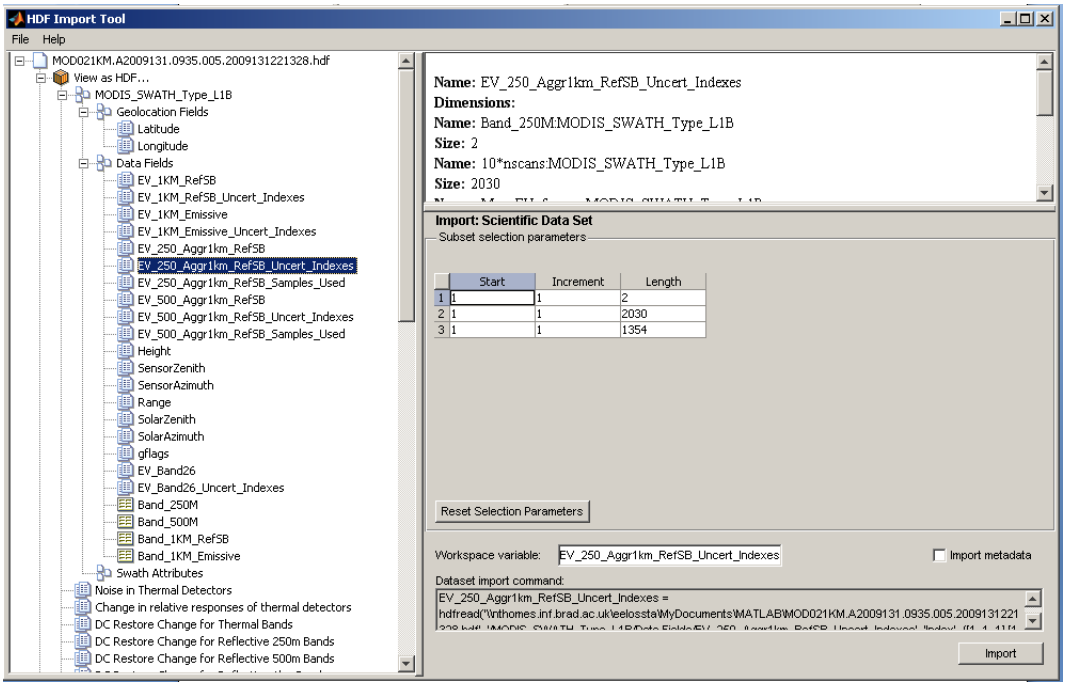

Figure 2-4 HDF Tool reading an HDF file

After the HDF tool has read an HDF file, the individual bands can be imported to MATLAB workspace, for subsequent processing. Alternatively, the command line can be used to read bands from the HDF file using the **hdfread** function.

2.3. OVERVIEW OF PREVIOUS DUST STORM DETECTION WORK

Satellite remote sensing is the common method for monitoring dust storms but its use for identifying dust storms over sandy ground is still limited as the two share similar characteristics. Many researchers have proposed methods aiming to distinguish dust storms from clouds, ground and water surfaces using images from instruments such as MODIS [8, 9], MERIS [8], TOMS [7], SeaWiFS [24], GOES [25] and images from satellites such as NOAA-AVHRR [26], Landsat and GMS [27].

2.3.1. DUST STORM DETECTION USING MODIS DATA

Several methods have been presented for the detection of dust storms based on thresholding some quantity calculated using data from a few of the 36 spectral bands provided by the Moderate Resolution Imaging Spectroradiometers **(**MODIS) on board the Terra and Aqua satellites at pixel resolutions varying from 250m to 1km. Calibrated spectral radiance data provided in the thermal emission bands can be used to calculate a corresponding Brightness Temperature (BT) by assuming the radiation is emitted from a surface behaving like a blackbody with emissivity of 1.0.

Reference [25] describes what was then (2003) a new dust enhancement technique to create the Naval Research Laboratory's 1-km Dust Enhancement

Product (DEP) over land and water during daytime. Compared against standard visible (0.65 μm) images, the DEP over land algorithm provides an improved ability to distinguish areas of dust from water and ice clouds and bright desert backgrounds by using false colour images as an enhancement technique formed using high spatial and spectral resolution digital data from MODIS. To enhance dust storms over land, the DEP technique is based on the following physical attributes: (1) elevated dust produces a depressed BT against the hotter land background temperature; (2) dust can be differentiated from water clouds having the same radiometric temperature by the colouration properties of mineral dust; (3) dust storms often have positive values of Brightness Temperature Difference (BTD) (between 12 μm and 11 μm) and (4) the additional infrared (1.38 μm) information from MODIS enables the dust signal to be separated from the other spectrally similar components of the scene. The DEP over land algorithm is generally applicable to any satellite having the requisite spectral bands. On the other hand, it has some limitations for detecting dust storms: (1) it is useful only during daytime, (2) some parts of cold terrain can appear falsely enhanced; (3) the sun glint area is prescribed, and the true area is a dynamic function of local sea surface state; (4) in terms of Brightness Temperature differences, not all dust pixels have large positive values, depending on opacity and background; (5) dust storms that are viewed at longer optical paths generate stronger enhancements; and (6) DEP is unable to detect dust storms underneath clouds.

Reference [9] presents a method for the Automatic Detection of dust storms in the northwest of China using a decision tree classifier with features comprising the difference between bands 7 and 3, the Normalized Difference Snow Index (NDSI) and the quantity defined in equation 2-1

$$Y2 = 2 * b7 + b1$$ Equation 2-1.

where bn represents a band number. The decision tree discriminates areas of land, dust storms, cloud and snow. A weakness of this study is that the weak dust regions are not easily distinguished from the surface, because the lower dust content in these regions does not cover the surface sufficiently. Furthermore, cloud shadow and surface are mixed up with detected dust, so further improvement is still needed.

Reference [28] describes a method for detecting and separating dust storms from cirrus cloud over the Gobi desert using a combination of reflective and emissive MODIS bands. This method used the D-parameter technique based on equation 2-2

$$\mathrm{D} = \exp\{-[\mathrm{rr} * \mathrm{a} + (\mathrm{BTD} - \mathrm{b})]\}$$ Equation 2-2.

where rr is the ratio of the reflectances at wavelengths of 0.54µm and 0.86µm, a is a scaling factor which is equal 0.8 and b is an offset derived from the wavelength difference 11µm – 12µm related to BTD which is numerically equal to 2. Using the D-parameter makes it possible to separate cirrus clouds from high altitude airborne dust using a threshold of 1.

Reference [29] investigated a method that can distinguish sand and dust from cloud and surface, also determining the scope and intensity of sand and dust storms from MODIS images. The normalized difference snow index (NDSI) and the dust sand index (DSI) were used in this method to detect dust storm from cloud and land surface. The NDSI and DSI are defined in equations 2-3 and 2-4 respectively.

$$NDSI = (b7 - b3)/(b7 + b3) > 0 \qquad \text{Equation 2-3.}$$

$$DSI = (b20 - b29) > 33 \qquad \text{Equation 2-4.}$$

where *Bn* is a band number. This method was applied on the China dust storm event which occurred on 27th of March 2004. The results show this method to be very effective for the detection and scope of dust storms over China, also it can determine the intensity of sand and dust storms using multiple thresholds where the intensity is divided into different levels from weak to heavy. However, this method was less effective when it was applied to dust storm events occurring over sandy land.

Reference [1] proposes a method based on the Normalised Difference Dust Index (NDDI) for the detection of sand dust storms in the north of China by combining the Terra and Aqua MODIS solar reflectance band (SRB) measurements, which is defined in equation 2-5.

$$NDDI = (b7 - b3)/(b7 + b3) \qquad \text{Equation 2-5.}$$

To identify airborne and ground sand and dust, these authors use a threshold of 275K on the BT using MODIS band 31 to detect airborne or ground sand and dust. The NDDI index is effectively a method for separating SDS from water/ice clouds and ground features except sandy ground. Although, this method can be useful for the detection of dust storms over non-sandy ground, it does not give good results over sandy ground such as the Sahara desert, even when enhanced using the BT calculated from band 31. So, if this technique is to be used successfully over surfaces such as the Sahara, it seems likely that extra bands will be needed.

Reference [2] describes the use of Terra and Aqua MODIS level 1B thermal infrared data (TIR) at wavelengths of 8.5μm, 11μm, and 12μm for detecting and monitoring dust storms in the north of China. It is found that combining the BTD between 8.5μm and 11μm with the BTD between 11μm and 12μm can be used to detect dust storms in northern China during both day and night. However, this method is less effective for detection of dust storms over sandy land.

Reference [30] describes an investigation of the dust storm which occurred on 7 April 2001 in the north of China using the MODIS thermal infrared bands 29, 31 and 32. A dust storm mask algorithm was developed to identify dust storms using the BTD between bands 29 and 31 and the BTD between bands 31 and 32. BTD values between bands 31 and 32 of less than -0.5 and BTD values between bands 29 and 31 of greater than 0 represent a strong dust region, while BTD values between bands 31 and 32 of less than -0.5 and BTD

values between bands 29 and 31 of less than 0 represent a weak dust region. Other cases represent cloud, or other unknown surface. This algorithm can be used to identify dust storms, such as the one investigated, during both day and night over non sandy areas.

Reference [31] describes the use of a BTD technique to detect and monitor desert dust using infrared MODIS and SEVERI data. The BTDs used in this study are from bands 20 and 31, bands 29 and 31 and bands 31 and 32. Several thresholds were created to classify a data pixel as dusty or not dusty. The BTD between 31 and 32 for dust storm is generally negative over land and smaller than -0.5K over sandy land. The BTD between 20 and 31 for dust storm during the day is positive, while the BTD between 29 and 31 is also negative. The results show that more work is needed to improve the quality of dust storm detection. However, this method can be used for monitoring dust storms.

Reference [32] describes an integrated approach for separating dust from clouds during both day and night using MODIS thermal infrared bands. This method is based on the spectral variability of dust emissivity in bands 20, 29, 31 and 32. A combination of three methods was used to identify dust and cirrus cloud. The first method used the *D**-parameter (defined by equation 2-6) test for detecting dust storms at night

$$D^* = \exp\{[(BTD_{31-32}) - C]/[(BTD_{29-31}) - E]\} \qquad \text{Equation 2-6.}$$

where *C* and *E* are the thermal offsets for BTDs between bands 31 and 32 ($BTD_{31\text{-}32}$) and bands 29 and 31 ($BTD_{29\text{-}31}$), respectively. Dust storm and cloud correspond to *D** values greater or less than one respectively. The second

approach uses the slope of the best-fit line ($\Delta BTD_{29\text{-}31}/\Delta BTD_{31\text{-}32}$) to identify dust and cloud, where Δ denotes a differential change of the parameter. If the slope is negative, the domain pixels are identified as dust. The third approach uses $BTD_{20\text{-}31}$ to detect dust storm from cloud over water.

Reference [33] (Huang et al.) describes the use of the BTD between the MODIS channels at 11μm and 12μm and the microwave polarized index (MPI defined in equation 2-7) for the 89GHz and 23.8GHz channels of the Advanced Microwave Scanning Radiometer (AMSA-E) on board the Aqua satellite

$$MPI = \Delta T_{b89} - \Delta T_{b23.8} \qquad \text{Equation 2-7.}$$

where ΔT_{b89} and $\Delta T_{b23.8}$, the microwave polarized brightness temperature differences of the 89GHz and 23.8GHz channels respectively, are defined as follows

$$\Delta T = T_{bv} - T_{bh} \qquad \text{Equation 2-8.}$$

T_{bv} and T_{bh} are the vertical and horizontal polarized radiation measurements respectively. Huang's results showed that a BTD with threshold -2K can identify 80% of the dust storm and 5% of clouds over the dust region. A threshold of -1K can identify 98% of dust and 15 % of clouds. At the same time MPI can detect 85% of dust storms under cloud using a threshold of -7.0K. However, thresholds less than -7.0K would identify higher percentages of dust storms and about 5% of clouds. In conclusion BTD can be used to detect dust over both sea and land surface when there are no clouds and MPI can be used to detect dust storm

under cloud. For this reason, the combination of BTD and MPI could possibly overcome some of the weaknesses of the individual methods.

Reference [34] investigates a dust storm detection approach using the BTD between bands 32 and 31 with the BTD between bands 20 and 30 and describes the Thermal Infrared Dust Index (TIDI) method for the detection of Saharan dust storms over the Atlantic Ocean during 2004-2006. The investigation found there was a close relationship between the aerosol optical thickness (AOT) at 550nm and the BTs of MODIS bands 20, 30, 31 and 32. The TIDI is calculated using equation 2-9.

$$TDI = C0 + C1 * BT20 + C2 * BT30 + C3 * BT31 + C4 * BT32 \quad \text{Equation 2-9.}$$

The values of the coefficients C0, C1, C2, C3 and C4 are -7.9370, 01227, 0.0260, -0.7068 and 0.5883 respectively. The results of this study show that dust storms can be distinguished from the Atlantic Ocean during day or night (as it uses thermal infrared bands). However, this method has some limitations in distinguishing dust storm from cloud and the applicability of this method for detecting dust storms over land needs more detailed study.

Reference [7] describes the use of the BTD between bands 31 and 32 for monitoring a dust storm, extracting its extent and estimating its intensity level during both day and night in the north west of China in 2006. However the use of BTDs with zero thresholds was not enough to prevent some cloud being falsely detected as dust. For this reason its authors used an NDDI technique to remove clouds during the day. At the same time temperatures greater than 263K and less than 280K were used to distinguish dust storms from clouds and

land respectively at night using the BT of band 31. The result of this study showed that the detection of dust storms was very effective in the northwest of China. However, when the author of this thesis applied this method to some dust storms events over the Sahara desert it was found to be less effective.

Reference [35] describes a comparison of Neural Network based classification using individual pixels and prior segmented regions as the objects to be classified. The pixel classification was based on selected training pixel samples in several bands from seven land cover types (irrigated agriculture, rain fed agriculture, grassland, tropical dry forest, human settlement, and orchards). The segmented region classification involves: 1) segmenting an image into non-overlapping objects and constructing a feature vector for each of these objects; 2) Classification of the features into one of the seven prior classes. The results showed that the segmentation based method performed better than the pixel based method.

Reference [36] describes the use of thermal MODIS data band 31 and 32 data to build a method for extracting dust information. The researchers used two kinds of algorithms to separate the dust from other objects such as cloud, desert surface and other ground surfaces. The research used equations 2-10 and 2-11 defined as follows

$$\Delta T = T_{32} - T_{31} (T_{32} - T_{31} \geq 1K) \qquad \text{Equation 2-10.}$$

$$\Delta T = 0 \ (T_{32} - T_{31} < 1K) \qquad \text{Equation 2-11.}$$

where T_{31} and T_{32} are the brightness temperatures of bands 31 and 32 respectively. The threshold used to separate dust storm from other objects is 1K. Although this method obtained an accurate result when it was applied in northern China, it did not give the same accuracy over the Sahara desert.

Reference [37] describes the use of the BTD between bands 31 and 32 to estimate the density of a dust storm occurring in Australia on 23 September 2009. The work estimated that at least 3 million tons of topsoil was blown away as dust in this dust storm.

Reference [38] uses a comparison between Maximum Likelihood classifier (ML) and Probabilistic Neural Network (PNN) to develop an automatic dust storm detection process applied over the United States. The data used were the MODIS multispectral bands from the Terra satellite. The feature vectors used pixels values from bands 20, 29, 31, and 32. A total of 31 dust storm events were used in this study. The results showed the PNN method was much better than the ML method for dust storm detection with detection accuracies of 84% and 67% respectively.

Reference [39] describes the use of the Thermal Infrared Integrated Dust Index (TIIDI) and four MODIS bands to monitor dust storm over various land cover types, including vegetation, bright surfaces and water. BTD_{12-11} (the subscripts indicate band wavelengths in μm) is used to distinguish cloud from other objects, $BTD_{8.6-11}$ is used to identify dust storm and surface sand and $BTD_{3.7-11}$ is used to separate dark surface and to represent the intensity of dust storm. The TIIDI algorithm is based on equation 2-12

$$TIIDI = \left(BTD_{12\mu m-11\mu m}\right) * \exp\left(\frac{BTD_{8.6\mu m-11\mu m}}{a}\right) * \left(BTD_{3.7\mu m-11\mu m}\right)$$

Equation 2-12.

The value of parameter a is set at 10 when $BTD_{8.6\text{-}11}$ is positive, otherwise it is set at 5.The results show that the TIIDI can distinguish mineral dust from cloud and land surface over bright surfaces and ocean.

2.3.2. DUST STORM DETECTION NOT USING MODIS

Several instruments other than MODIS have also been used for dust storm detections and this section, presents some of this related work.

Reference [40] describes a method to extract dust storm information and divide them into three intensity categories (low, medium and high density) using a multi-threshold method. The data used in this study are ten data events, which occurred in spring 2000, observed from the Advanced Very High Resolution Radiometer on board one of the National Oceanic and Atmospheric Administration polar orbiting satellite (AVHRR / NOAA). The authors analyzed the relationship between the dust storms and the surface of Northern China by analyzing the types of land cover and the degree of vegetation coverage where dust storms passed. It found that the land cover conditions and the degree of vegetation coverage have the dominant affect on the formation and intensity of dust under the same meteorological conditions. The authors used two channels (CH1 and CH4) to separate dust storms from land surface and clouds respectively, as shown in equation 2-13:-

$$21 < CH1 < 24 \; and \; 276 < CH4 < 286$$ Equation 2-13.

The authors of this work found that the intensity of dust storm over bare land is higher than where the surface covered by vegetation, as might be expected.

Reference [41] describes a study of the capabilities of several remote sensing instruments with respect to monitoring dust storms over the Nile Delta using different wavelength ranges. The Total Ozone Mapping Spectrometer (TOMS) was used to detect dust storms in the Ultraviolet region, but was found to be very unsuitable because of its poor resolution. Data from MISR on the Terra satellite was studied to evaluate the usefulness of monitoring in the visible region of the spectrum using different viewing angles. The results showed that dust storm events which are difficult to detect at nadir may be easily detected by off-nadir angle viewing. Furthermore, different levels of MISR products were used to extract physical parameters of dust storms such as optical thickness, dust particle size and distribution, concentration and land surface cover underneath the dust storms. This information can be used to study the development, movement and transport of dust storms. Also TRMM Microwave Image (TMI) data was used to study the effect of dust storms on water vapour in the microwave range. The result shows the location of dust storm and haze matches the position of water vapour or smog. There are some disadvantages to using MISR as its repeat coverage of the Earth is from 2 to 9 days, which is insufficient to continuously monitor dust storms. Also, MISR has just 4 bands for each camera. TRMM Microwave Image (TMI) data was particularly chosen for quantifying the water vapour, the cloud water, and the rainfall intensity in the atmosphere.

Reference [27] uses the BT technique to detect Asian dust aerosols during both day and night using the meteorological satellite data from AVHRR / NOAA and GMS-5 / VISSR. This technique uses two AVHRR 4 thermal infrared bands (10.3μm - 11.3μm) and 5 (11.5μm - 12.5μm), and two VISSR IR1 (10.5μm - 11.5μm) and IR2 (11.5μm - 12.5μm) bands. The Aerosol Vapour Index (AVI) is calculated as follows for both instruments

$$AVI(AVHRR) = n(5) - n(4) + 200, \quad for\ NOAA/AVHRR \qquad \text{Equation 2-14.}$$

$$AVI(VISSR) = IR(2) - IR(1) + 100, \quad for\ GMS-5/VISSR \qquad \text{Equation 2-15.}$$

where $n(\mathrm{i})$ and $IR(\mathrm{i})$ are the brightness temperatures of thermal infrared band i for NOAA / AVHRR and GMS-5 / VISSR respectively. The constants 200 and 100 are related to the raw data format; 10 bits for NOAA / AVHRR and 8 bits for GMS-5 / VISSR. Comparing the results from this technique with data from ground observations confirmed this method can detect aerosols of Asian dust.

Reference [42] describes a technique to detect dust storms using Principal Component Analysis (PCA) as a tool for data fusion. The PCA technique was applied to Multi-angle Imaging Spectroradiometer (MISR) data observed over the Liaoning region of China as well as parts of northern and western Korea on April 8, 2002. Three different experiments were included in this study using various angular and frequency combinations. The first experiment applied PCA to all the 20 bands rendered by different angles in the form of a multi-dimensional product and then the first eigenvalue, which contains about 93.3% of the total data variation, was used with K-means clustering for classification of the image data. The second experiment applied

PCA to information from different angles for one particular frequency and then the first eigenvalue of each frequency, which contains about 94.2% of total data variance, and was used with K-means clustering for classification. The third experiment applied PCA to the information from different frequencies for each individual camera and then the first eigenvalue of each camera, which contains about 99% of the total data variance, was used with K-means clustering. Finally, the result of each experiment was compared with the original data. The results show that the first experiment was the best for classifying dust storm data. The PCA technique has some limitations with MISR data: first, this technique is just useful during the day; second, it is just useful over a dark surface.

Reference [43] describes a study of the characteristic behaviours of Brightness Temperature and Aerosol Index associated with dust storms over the Western end of the Indo-Gangetic basin using the TOMS aerosol index and Advanced Microwave Sounding Unit (AMSU) data. The 23.8GHz channel from AMSU was used to study the Brightness Temperature near the surface. The results showed that dust storms decrease the Brightness Temperature. Also, the results show that multisensory data can be very useful in monitoring the transport and characterization of dust events.

An algorithm is developed in [44] for the detection of dust storms over-water using five channels of the AVHRR imager on board NOAA satellites. The areas of study were the north and south Atlantic, the Mediterranean Sea, the Red Sea, the Arabian Sea, the Persian Gulf, the Yellow Sea, and the sea off the north eastern coast of Australia. The authors used the BTD between the 11μm, and 12μm channels and the 0.63μm, 0.65μm and 0.86μm channels, in addition,

to improve the detection of dust storms over water. This technique was limited to detecting dust storms over water and in daytime.

Reference [8] describes an automatic threshold approach using true colour images from MERIS to detect the centres of dust storms and their intensities over non sandy ground (Northwest of China) using the FE-Otsu algorithm. Although this method can be applied to MODIS data, it almost certainly does not work in daytime over bright surfaces such as the Sahara desert because sandy ground and dust storms have very similar appearances and it cannot work at night.

Reference [45] describes an automated algorithm to generate a dust storm mask applied to MSG SEVIRI satellite imagery to extract African dust storms. This automated algorithm used the BTD between 10.8μm and 12.1μm channels with threshold functions specified in equation 2-16

$$-0.5K \geq \left(BTD_{10.8\mu m - 12.1\mu m}\right) \geq -3.5K and\ BT_{10.8\mu m} \geq 280K$$

Equation 2-16.

The results obtained showed that the dust mask was accurate and that the tuning of a related tracking algorithm is efficient.

Reference [26] describes an automated method for detecting dust storms, locating dust sources and finding dust storm direction using the BTD between bands 4 and 5 using AVHRR / NOAA imagery. This difference between bands 4 and 5 is used as an initial step to detect the presence of the dust storm area then K-means classification is performed to segment the dust

storm region from other image content. Then several different filters are used to remove cloud pixels from the dust storm and to produce a binary dust image.

Reference [46] described a dust Index (DI_{CLM}), defined in equation 2-17, formed by combining LIDAR and multispectral IR data to detect dust aerosol over the Taklamakan Desert during daytime in the springs of 2007 and 2008.

$$DI_{CLM} = C_0 + C_1 * BTD_1 + C_2 * BTD_2 + C_3 * \beta * 100 + C_4.\delta * 10 + C_5 * \chi * 10 + C_6 * \varepsilon + C_7 * \zeta$$

Equation 2-17.

BTD_1 is the brightness temperature difference between the 10.60μm and 12.05μm channels, and BTD_2 is the brightness temperature difference between the IIR 8.65μm and 11.60 μm channels, β is the layer's mean attenuated backscatter at 532nm, δ is the layer's mean depolarization ratio (layer-integrated perpendicular-to-parallel attenuated backscatter at 532nm), χ is the layer's volume colour ratio integrated from 1064nm to 532nm, ε is the layer's top altitude, ζ is the layer's base altitude above mean sea level (MSL), and C_0 to C_7 are coefficients. A limitation of this method is it is useful for detection of dust aerosol during daytime only.

Reference [47] introduced a new method for the detection of dust clouds in NOAA-AVHRR satellite images. The method used a region growing segmentation algorithm with a set of seed points applied on the difference between band 4 (10.3μm – 11.3μm) and band 5 (11.5μm – 12.5μm). The paper focuses on two dust events in south-western North America on April 15 2003 and March 04 2003. A threshold of 0 is used on the difference between band 4

and band 5 before using the region growing algorithm. The results show this approach is promising as most of the dust events were detected.

2.4. OVERVIEW OF SATELLITE IMAGE CLASSIFICATION

Image classification is an important part of remote sensing, image analysis and pattern recognition. In some cases, the classification itself may be the object of the analysis. For example, classification of land use from remotely sensed data produces a map like image as the final product of the analysis [48]. Numerous classification algorithms have been developed, many of them highly specific and only applicable to a reduced class of problems and image data. Without an additional source of knowledge, automatic image classification based on low level image features seems unlikely to succeed in extracting semantic objects in generic images [49]. Multi-band classification is the method for using pixel values calculated from different bands or merging of bands and classifying them into their object classes.

Reference [50] developed a method for automated classification of surface and cloud types using MODIS. Its surface and cloud-type classification is based on the maximum likelihood (ML) classification method. Twenty five bands with eight BTDs have been used in this method as features to classify MODIS image data into eight classes; clear water, clear land, mixed types, middle-to-low clouds, middle-to-high clouds, and high clouds. The ML performance for classifying MODIS images was validated using the MODIS cloud mask and this found that the 1-km-resolution ML classification mask improves over the 1-km-resolution MODIS cloud mask in some situations. Also, combined use of the MODIS cloud mask and ML cloud classification improves

identification of clear skies in the MODIS imagery as well as cloud types. A limitation of this method is that it did not include a dust storm class.

Reference [51] describes the segmentation of remotely-sensed images by an incremental neural network (INeN), which is a two-layer network, The number of nodes in the first layer of the INeN is determined by the structure of the feature vectors. The number of nodes in the second layer, which is also called the index layer, is determined by the number of output classes. In this paper a comparison is made between pixels based classification and region based classification. The data set consists of seven images acquired by the Landsat-5 TM sensor. In the first method, features are formed by the intensities of corresponding pixels from each channel. The second method is similar to the first but with the intensities of pixel neighbourhoods being used in each channel. Nine features are obtained from each image. The feature vector is formed by the intensities of 63 (7x9) pixels. The results show that the pixel extraction method produces much greater accuracy than the feature extraction method.

An automated satellite image classification design using object-oriented segmentation algorithms is developed in reference [49], A new region-merging segmentation technique which Includes the spectral and textural features of the objects linked with the Food and Agriculture Organization of United Nation (FAO) Land Cover Land Use classification system. This technique was tested on Landsat and Aster Images and achieved overall accuracy values of 92% for Aster images and 89% for Landsat images using standards measurements of conviction matrix. A limitation of this method for more general use is in using the FAO Land Cover Land Use classification system which is a particular technique

for classifying land cover using high resolution satellite images whereas MODIS has low resolution multi-band images.

Reference [52] provides a comparison between a decision tree classifier (DTC) and a Maximum Likelihood Classifier (MLC) for mapping very high resolution satellite images into 11 classes (Stone, House, Grassland, Grass dry area, Plain land, Sand, River, Submerged area, Sea water, trees and pool), The training feature data for both methods was prepared using RGB pixel values from the satellite image. The classified image overall accuracy was found to be 86.66% using the DTC and 81.33% using MLC.

Reference [53] describes a comparison between two algorithms, namely a feed-forward back-propagation artificial neural network and a K-Means algorithm for segmentation and classification of remotely sensed images. Both algorithms used RGB images. It is found that the K-means algorithm gives very high accuracy, but it is useful for a single database at time as a K-means unsupervised classifier, whereas the neural network is useful for multiple databases, once it is trained for it. The neural network also provides good accuracy. The limitations of this method is that it concentrated only on RGB images, which is not effective for separating dust storms from sandy land as both have the same colour.

2.5. CHAPTER CONCLUSION

This chapter was divided to three main parts; the first included an overview of the MODIS instrument and satellites, the orbits of each satellite, the number of bands and the wavelength range of each band. In addition, this part of the chapter included some information about MODIS products and

applications and information on system tools used for reading, viewing and re-projection of MODIS HDF files.

The second part of this chapter provided information about previous studies on dust storm detection over different surface using different instruments.

The third section provided information about previous studies on satellite images classifications using different methods and suggested the artificial neural network as a popular and effective tool for classifying satellite images.

The literature survey showed that a significant amount of previous work investigated the detection of dust storms. However, the achieved detection performances are still limited, as both dust storms and sandy land share some characteristics, leading to difficulty in separating dust storms and sandy land. Dust storms also share some characteristics with low clouds and shadow which also leads to difficulty in separation. The detection of dust storms at night is still also limited due to low night-time temperatures, where all previous methods concentrated on using the BT for detection of dust storms during the night.

Furthermore, there is no single method that is suitable for the detection of dust storms over different surfaces. For this reason more work is needed to improve the detection of dust storms, and to generate an automated system that can be used for detection dust storms over different surfaces and for both day and night.

Also, there are no ground truth data that can be used for validation. The only way to provide ground truth data for dust storms is to use manual detection of

dust storms, as has been used in reference [38]. Chapter 3 describes the use of brightness temperature difference between bands 23 and 31 for distinguishing between dust storm and sandy land. It also describes using differentiation between these two bands with the NDDI method for the detection of dust storms over sandy land using threshold method. The second section of Chapter 3 presents the use of both BTD between bands 23 and 31 with the BTD between bands 31 and 32 for detection dust storms in both day and night.

CHAPTER THREE

3. DUST STORM DETECTION USING THRESHOLDING

3.1. INTRODUCTION

As mentioned in Chapter 2, satellite remote sensing is expected to become the primary approach for detecting and monitoring dust storms [1] because there are many potential advantages to using this technology, including flexible coverage of wide areas, and continuous rapid monitoring of natural hazards. At the same time satellite remote sensing is limited to detection of dust storms using single band satellite images, as they share some characteristics with cloud and sandy ground. This chapter concentrates on the detection of dust storms from multispectral satellite (MODIS) images using threshold-based techniques, and is organized as follows. Section 3.2 presents a threshold technique for daytime dust storm detection, and Section 3.3 describes a threshold technique for the detection of dust storms during both day and night time. Section 3.4 includes some conclusions.

3.2. DAY TIME DUST STORM DETECTION

The MODIS thermal infrared emissive bands 20, 29, 31, and 32 are the ones most commonly used for detecting dust storms. Data from these bands are used to calculate brightness temperatures for sea, land and atmospheric surfaces with different emissivities, as shown in Chapter 2. The brightness temperature differences between these bands can often distinguish dust storms

from other objects in MODIS images. The BTD between bands 31 and 32 (11 and 12 μm respectively) in particular have been employed in many dust storm detection schemes, because the emissivity of sand in band 31 is less than the emissivity of sand in band 32, whereas the emissivities of other surfaces and cloud in band 31 are higher than in band 32 [32]. The brightness temperature calculated for dust storms at 12μm is higher than the brightness temperature calculated at 11μm, and this leads to negative values of the brightness temperature difference for dust storms between 11μm and 12μm, while other surfaces and cloud will be around zero, or positive [39]. Most of the methods used for detecting dust storms over land surface have concentrated on BTD (31-32) and this is considered an effective method for distinguishing dust storms from other imaged surfaces. However, it is less effective for detecting dust storms over desert regions because the desert surface and the airborne dust have similar behaviour in bands 31 and 32 [20]. For this reason, this research concentrates on distinguishing between dust storms and sandy land. Data from the MODIS emissivity data library, shown in Table 3.1, is used in this study to analyse the emissivities of sand, sandy soil, soil and ice and water clouds in the bands 20, 21, 22, 23, 24, 25, 27, 28, 29, 30, 31, 32, 33, 34, 35 and 36. Bands 21 and 22 have the same wavelength but have different peak temperatures. Band 21 peaks at about 500 K, and band 22 peaks at about 335 K. Furthermore, band 22 is less noisy.

Table 3-1 Emissivities of Sand, Sandy Soil and Ice and Water clouds from the MODIS data library

Band	Wavelength µm	Sand	Sandy Soil	Soil	Ice	Water
36	14.192	0.98	0.98	0.95	0.93	0.96
35	13.907	0.97	0.99	0.98	0.93	0.96
34	13.675	0.97	0.98	0.99	0.93	0.97
33	13.359	0.97	0.97	0.97	0.93	0.98
32	12.032	0.98	0.98	0.97	0.95	0.99
31	11.017	0.96	0.96	0.97	0.98	0.99
30	9.737	0.88	0.88	0.92	0.99	0.99
29	8.518	0.81	0.78	0.88	0.98	0.98
28	7.334	0.99	0.98	0.98	0.98	0.98
27	6.752	0.99	0.99	0.98	0.98	0.98
25	4.545	0.95	0.88	0.75	0.97	0.98
24	4.472	0.96	0.92	0.75	0.98	0.98
23	4.056	0.87	0.76	0.63	0.98	0.98
21, 22	3.96	0.86	0.76	0.65	0.98	0.98
20	3.785	0.84	0.73	0.63	0.98	0.98

The emissivity data for sand, sandy soil, soil and ice and water clouds in Table 3.1 are shown graphically in Figure 3.1.

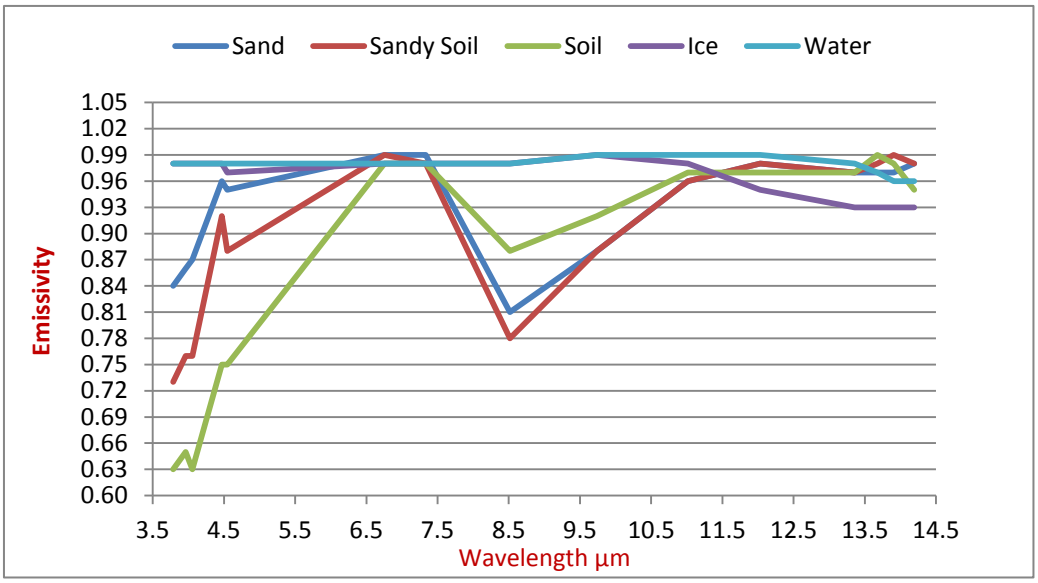

Figure 3-1 Plots of MODIS emissivity data for different surfaces

Table 3.1 and Figure 3.1 show that the emissivity of sand in band 31 (0.96) is slightly less than the emissivity of sand in band 32 (0.98), while the emissivity of

soil is the same in bands 31 and 32 (0.97) and the emissivity of water cloud is the same in bands 31 and 32 (0.99). At the same time the emissivity of ice cloud is slightly higher in band 31 (0.98) than in band 32 (0.95). Therefore, the BTD (31-32) could be useful for distinguishing dust storm from soil, and water/ice cloud. However, it is not good enough to distinguish dust storm from sandy soil as the emissivities of sandy soil and sand are the same in band 31 (0.96) and in band 32 (0.98). On the other hand, in band 23 the emissivities of sand (0.87), sandy soil (0.76) and soil (0.63) are significantly lower than the corresponding values in bands 31 or 32. The emissivity differences between bands 23 and 31 result in big differences between sand, water and ice cloud on the one hand and soil and sandy soil on the other hand as shown in Table 3.2.

Table 3-2 Emissivity differences between bands 23 and 31

	Band 23 – Band 31	**Result**
Sand	0.87 - 0.96	-0.09
Sandy soil	0.76 - 0.96	-0.2
Soil	0.63 - 0.97	-0.34
Ice cloud	0.98 - 0.98	0.0
Water cloud	0.98 - 0.99	-0.01

Table 3.2 shows that the differences between bands 23 and 31 can distinguish between sand, water/ice cloud and soil/sandy soil using -0.09 as threshold. For this reason the brightness temperature difference between bands 23 and 31 could be useful to distinguish dust storm from soil and sandy soil.

The average values over 50×50 windows for the brightness temperatures of sand, land, vegetation, water and cloud over all the MODIS emissive bands used to calculate cloud and land surface temperatures (bands 20, 21, 22, 23,

31and 32) are calculated and displayed in Figure 3.2 using the fifty dust storms, which occurred over North Africa, listed in Table 3.3.

Table 3-3 The MODIS data used in this study

No	Date	Time (GMT)	Satellite
1	2005/05/13	10:35	Aqua
2	2005/07/18	13:40	Aqua
3	2005/07/19	12:45	Aqua
4	2003/02/02	11:20	Aqua
5	2003/02/28	11:55	Aqua
6	2005/03/01	12:20	Aqua
7	2004/05/29	12:00	Aqua
8	2006/02/24	11:30	Aqua
9	2008/06/03	11:45	Aqua
10	2008/06/05	13:15	Aqua
11	2008/06/06	10:40	Aqua
12	2008/06/08	12:05	Aqua
13	2008/06/02	12:40	Aqua
14	2008/06/07	11:20	Aqua
15	2008/06/08	12:00	Aqua
16	2008/06/10	13:30	Aqua
17	2010/04/22	13:25	Aqua
18	2010/05/26	11:35	Aqua
19	2010/05/27	10:40	Aqua
20	2010/05/27	13:55	Aqua
21	2010/06/08	11:00	Aqua
22	2010/06/09	13:25	Aqua
23	2010/06/10	12:30	Aqua
24	2001/11/09	10:45	Terra
25	2002/05/07	10:30	Terra
26	2002/05/08	09:35	Terra
27	2006/02/23	09:15	Terra
28	2006/07/25	08:30	Terra
29	2006/02/25	09:00	Terra
30	2002/07/11	08:00	Terra
31	2008/01/04	11:45	Terra
32	2008/06/04	10:55	Terra
33	2008/06/05	08:20	Terra
34	2006/04/11	05:10	Terra
35	2010/06/08	07:50	Terra
36	2010/06/09	08:35	Terra
37	2010/06/10	10:55	Terra
38	2010/06/10	11:00	Terra
39	2010/07/04	10:05	Terra

40	2010/07/04	10:10	Terra
41	2010/07/24	09:45	Terra
42	2004/03/27	06:50	Aqua
43	2008/06/01	12:00	Aqua
44	2008/06/04	12:30	Aqua
45	2008/01/01	09:35	Terra
46	2008/01/01	11:10	Terra
47	2008/01/02	08:40	Terra
48	2008/01/04	08:25	Terra
49	200801/04	10:05	Terra
50	2008/08/03	09:35	Terra

The Brightness Temperature is an estimate of the temperature of a black body calculated from the thermal emissive MODIS level 1B data, without taking the emissivity of the surface into account, using Plank's radiation law defined in Equation 3-1[54].

$$L = \frac{2hc^2\lambda^{-5}}{\left(e^{hc/k\lambda T} - 1\right)}$$

Equation 3-1

where:

L = radiance (W/m^2/st/m).

h = Plank's constant (J.s).

C = speed of light in vacuum (m/s).

K = Boltzmann gas constant (J/K).

λ = band or detector centre wavelength (m).

T = Temperature (K).

However the level 1B data are scaled integers (SI) and are converted to calibrated radiance using the following equation

$$L = Radiance\_Scales \times (SI - Radiance\_Offsets) \qquad \text{Equation 3-2}$$

The **Radiance_Scales** and the **Radiance_Offsets** parameter values have been calculated by the MODIS Team for all data bands and are saved inside the HDF file Level 1B data [55].

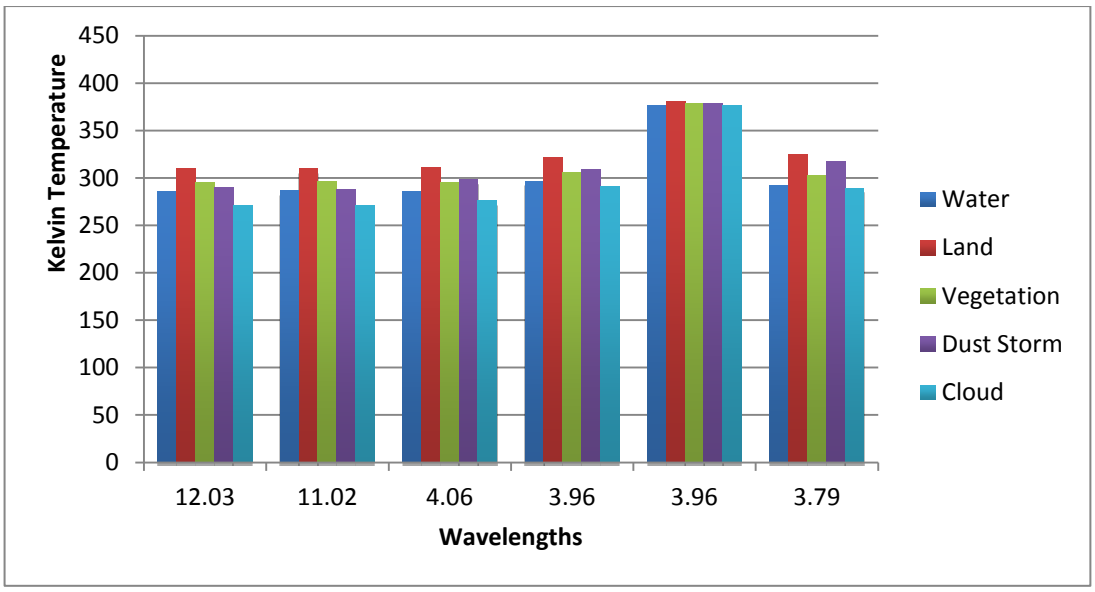

Figure 3-2 Average brightness temperatures of water, land, vegetation, dust storm and cloud in, from left to right, bands 32, 31, 23, 22, 21 and 20.

In Figure 3.2 it can be seen that the brightness temperatures of dust storm (298.4K) and cloud (276K) in band 23 (4.06μm) are higher than brightness temperatures of dust storm (287K) and cloud (271K) in band 31 (11.02μm), while the brightness temperatures of water (285K), land (310K) and vegetation (295K) in band 23 are less than in band 31 (286K, 310K and 296K for water, land and vegetation respectively). For these reasons the brightness temperature difference between bands 23 and 31 is useful for distinguishing

dust storm from land, vegetation, cloud and water and figures 3.3, 3.4, 3.5 and 3.6 show some examples of the brightness temperature difference between bands 23 and 31.

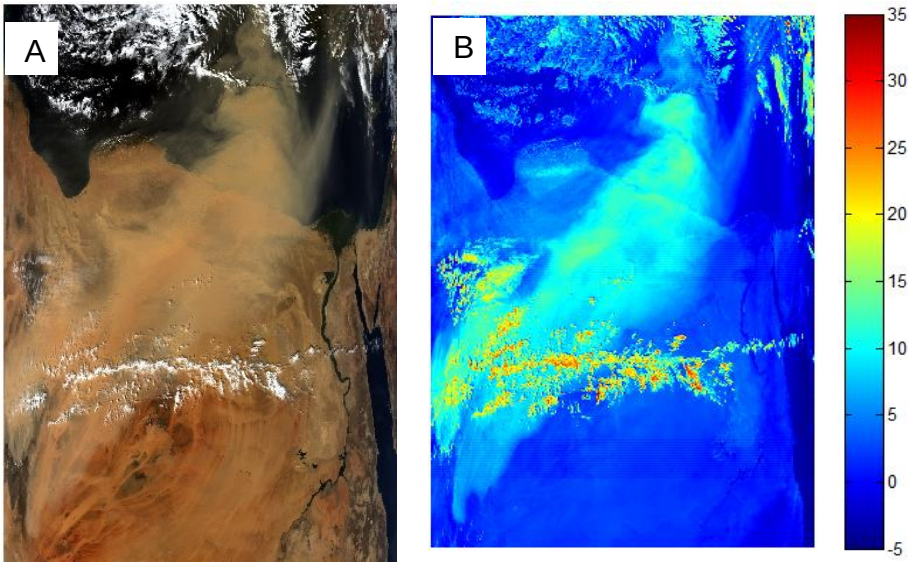

Figure 3-3 (A)is the true colour image from data number 8 in Table 3.3, captured by MODIS (Aqua) on 24th of February 2006 at 11:30 GMT over North Africa, (B) is the associated BTD between bands 23 and 31.

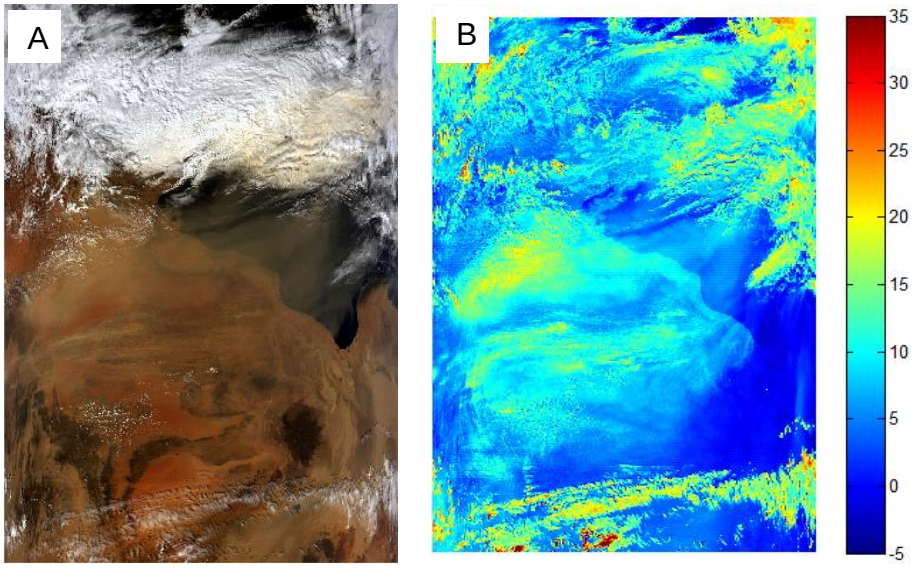

Figure 3-4 (A) is the true colour image from data number 6 in Table 3.3, captured by MODIS (Aqua) on 1st of March 2006 at 12:20 GMT over Libya, (B) is the associated BTD between bands 23 and 31.

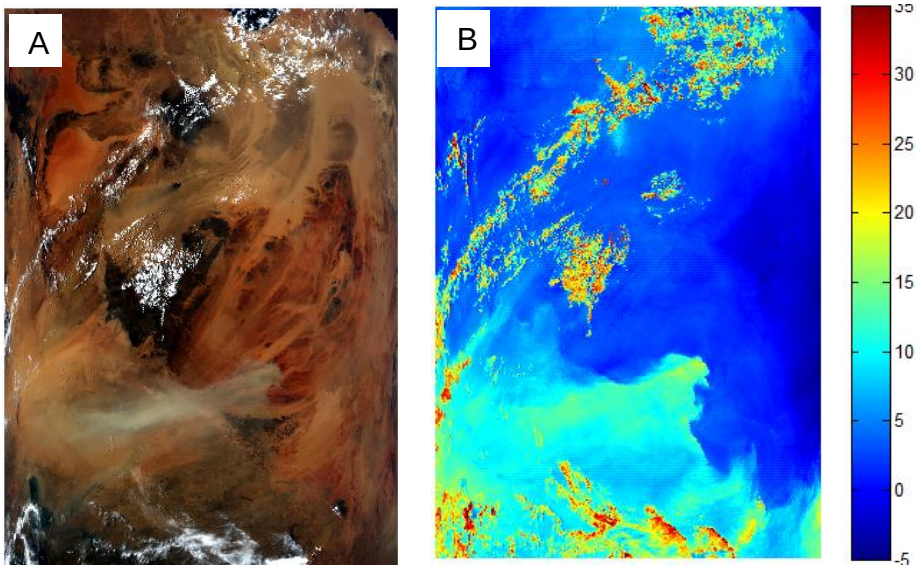

Figure 3-5 (A) is the true colour image from data number 7 in Table 3.3, captured by MODIS (Aqua) on 29th of May 2004 at 12:30 GMT over Libya, (B) is the associated BTD between bands 23 and 31.

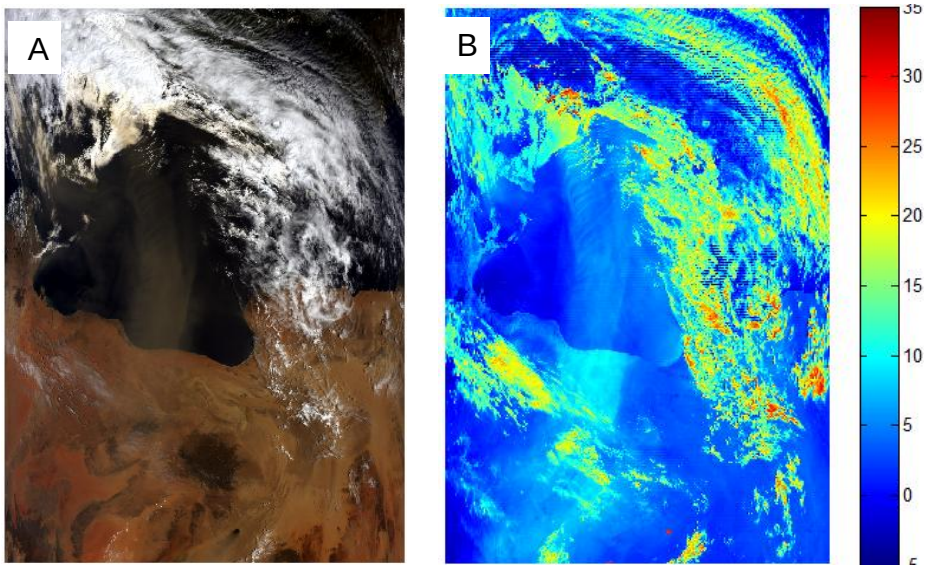

Figure 3-6 (A) is the true colour image from data number 26 in Table 3.3, captured by MODIS (Terra) on 8th of May 2002 at 09:35 GMT over Libya, (B) is the associated BTD between bands 23 and 31.

One of the common ways used to distinguish particular objects in images from other objects is to apply the threshold method, with suitable choices of threshold values. In this study, the distribution of objects pixels in the BTD between bands 23 and 31 was analyzed to separate dust storms from other objects. Figures 3.7

to 3.10 show examples of dust storm, cloud and sandy land with associated histograms.

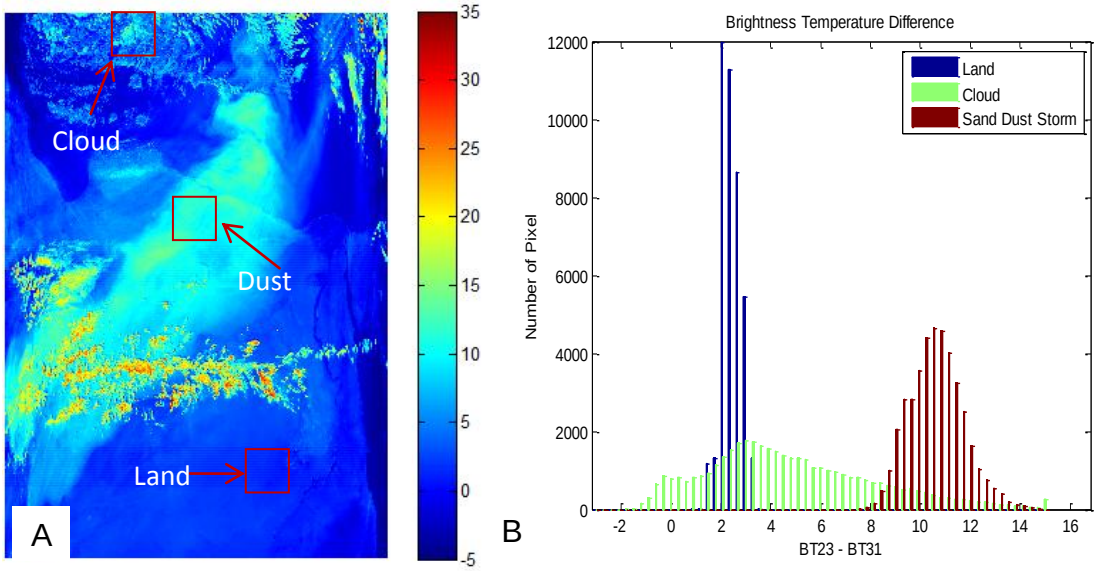

Figure 3-7 (A) is the BTD between bands 23 and 31 of data number 8 in Table 3.3, **(B) is** the histogram of Land, Cloud and Dust storm samples from the data shown in (A).

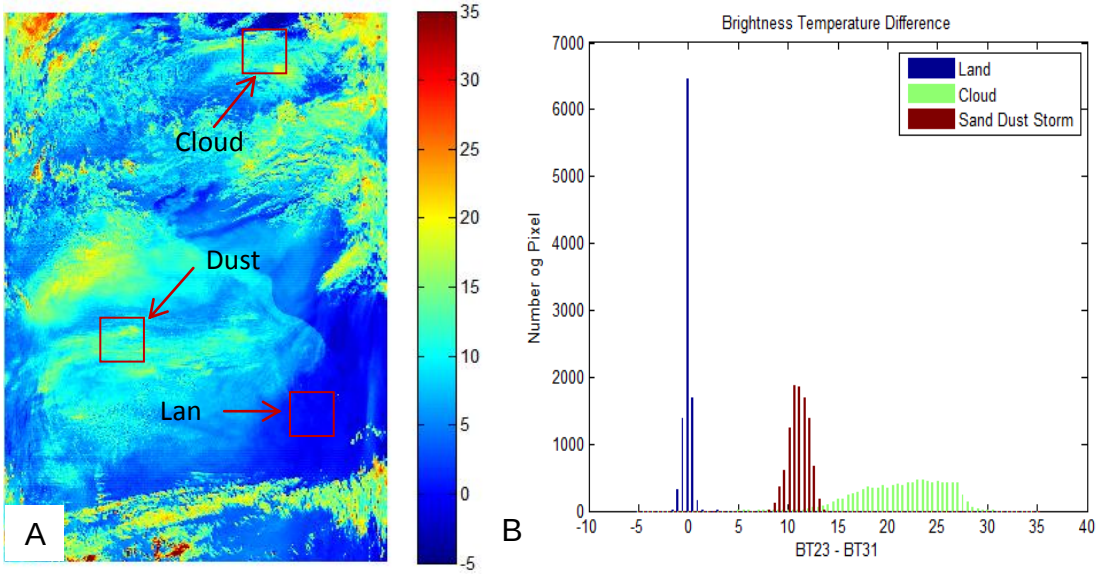

Figure 3-8 (A) is the BTD between bands 23 and 31 of data number 6 in Table 3.3, (B) is the histogram of Land, Cloud and Dust storm samples from the data shown in (A).

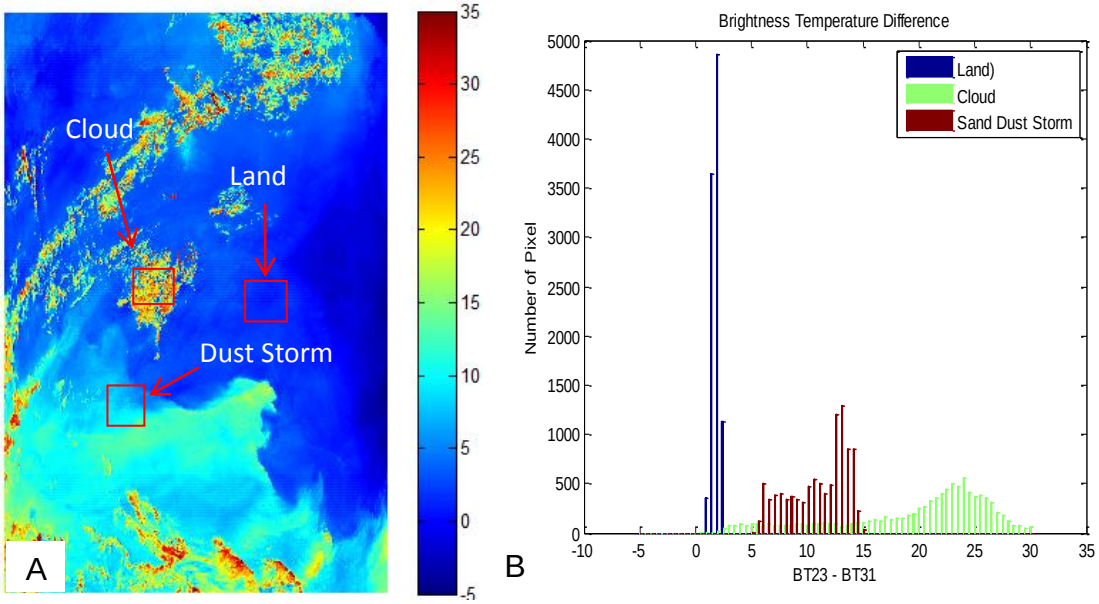

Figure 3-9 (A) is the BTD between bands 23 and 31 of data number 7 in Table 3.3, (B) is the histogram of Land, Cloud and Dust storm samples from the data shown in (A).

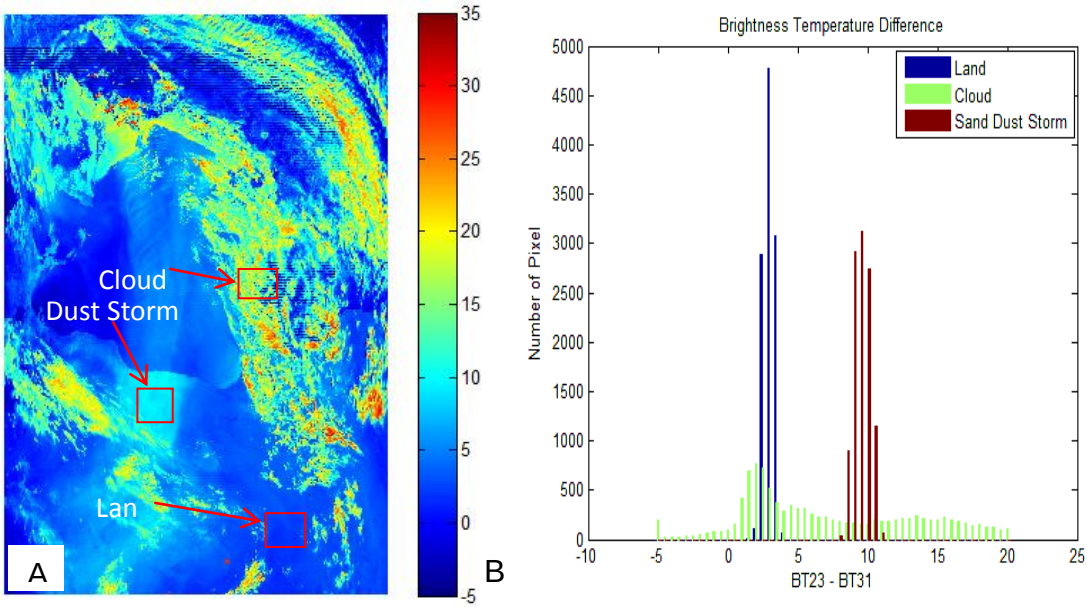

Figure 3-10 (A) is the BTD between bands 23 and 31 of data number 26 in Table 3.3, (B) is the histogram of Land, Cloud and Dust storm samples from the data shown in (A).

In figures 3.7 to 3.10 the distributions of dust storm pixels are between 5K and 15K and the distribution of sandy land pixels are between -1K and 5K. However, the cloud pixels are distributed between -5K and 30K. For this reason the dust

storm could be separated from the sandy land using 5K as threshold. However, this will include some cloud with dust storm. Mei et al. [7] used the Normalized Difference Dust Index (NDDI) method to separate dust storm from cloud as the reflectance of cloud in band 3 is higher than its reflectance in band 7 and the reflectance of sand and land in band 3 is less than in band 7, this will lead to positive sand and land while the cloud will be negative. Thus, the NDDI will be useful for separating cloud from dust storm. Figure 3.11 illustrates the method for detecting dust storms using MODIS data and thresholds.

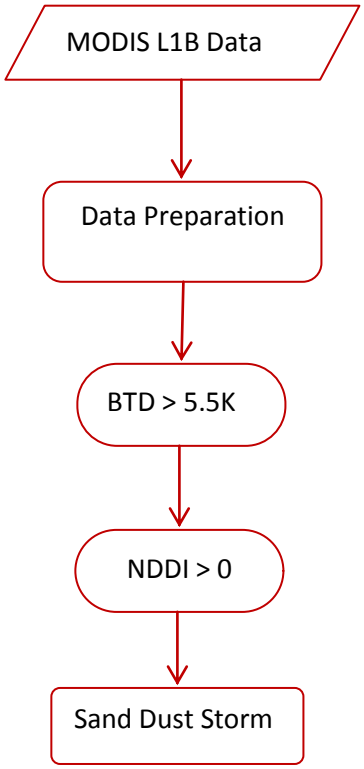

Figure 3-11 Flow chart of the proposed technique for Dust Storm detection

Results using this technique show that dust storm can be easily distinguished from dusty land and high cloud. However, it has some limitations in removing low cloud as the reflectance of low cloud in band 7 is higher than in band 3. Also, light dust storms are difficult to detect over water as the values of

the brightness temperature difference in light dust storms over water are very close to zero. In addition, this technique will be useful over land only and that is because it uses NDDI which depends on bands 3 and 7. This method was also implemented for the detection of dust storms over non-sandy surfaces such as in China which shows it can work on non-sandy land as well. Figures 3.12 to 3.16 show some results of applying this technique over different types of surface.

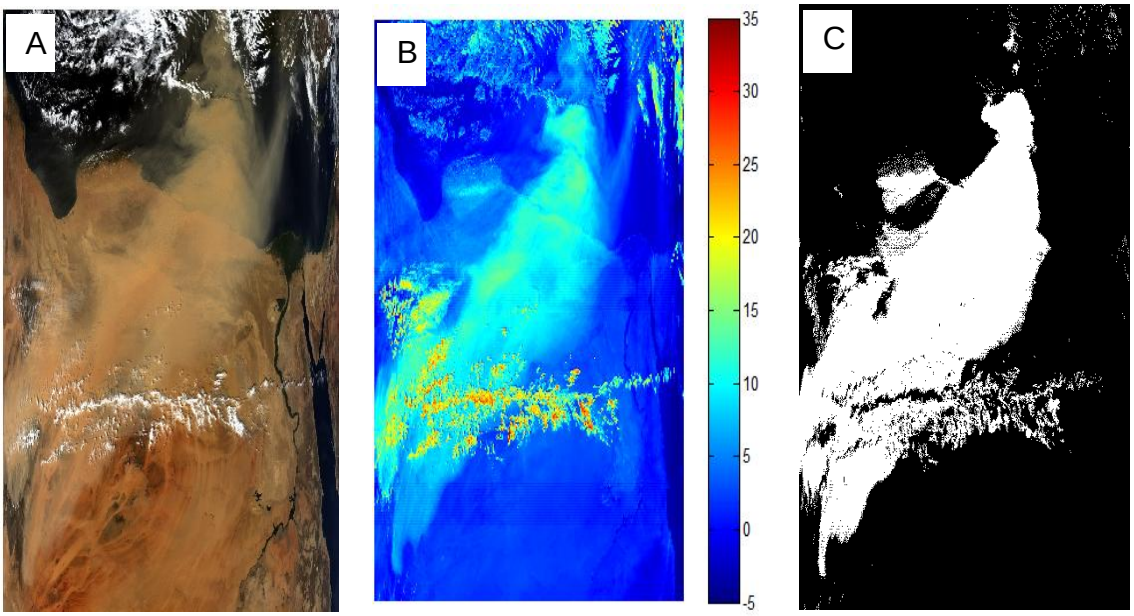

Figure 3-12 (A)is the true colour image for data number 8 in Table 3.3 captured by MODIS (Aqua) on 24th of February 2004 at 11:30 GMT over north Africa, (B) is the corresponding BTD between bands 23 and 31 and (C) is the corresponding binary image showing dust storm detection .

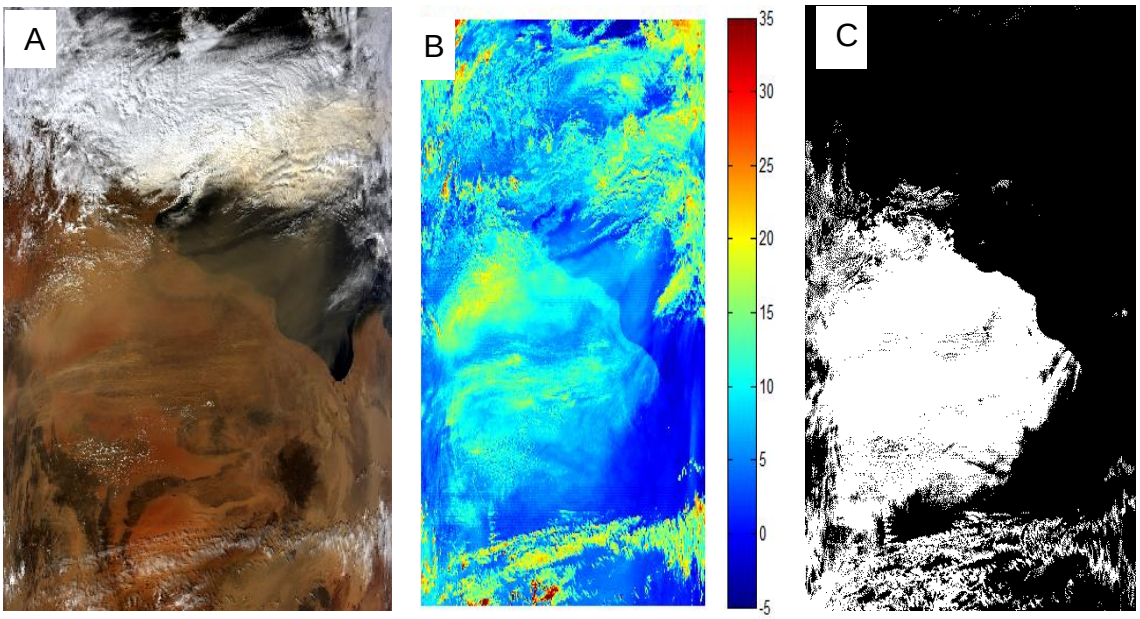

Figure 3-13 (A) is the true colour image for data number 6 in Table 3.3 captured by MODIS (Aqua) on 1st of March 2006 at 12:20 GMT over Libya, (B) is the corresponding BTD between bands 23 and 31 and (C) is the corresponding binary image showing dust storm detection .

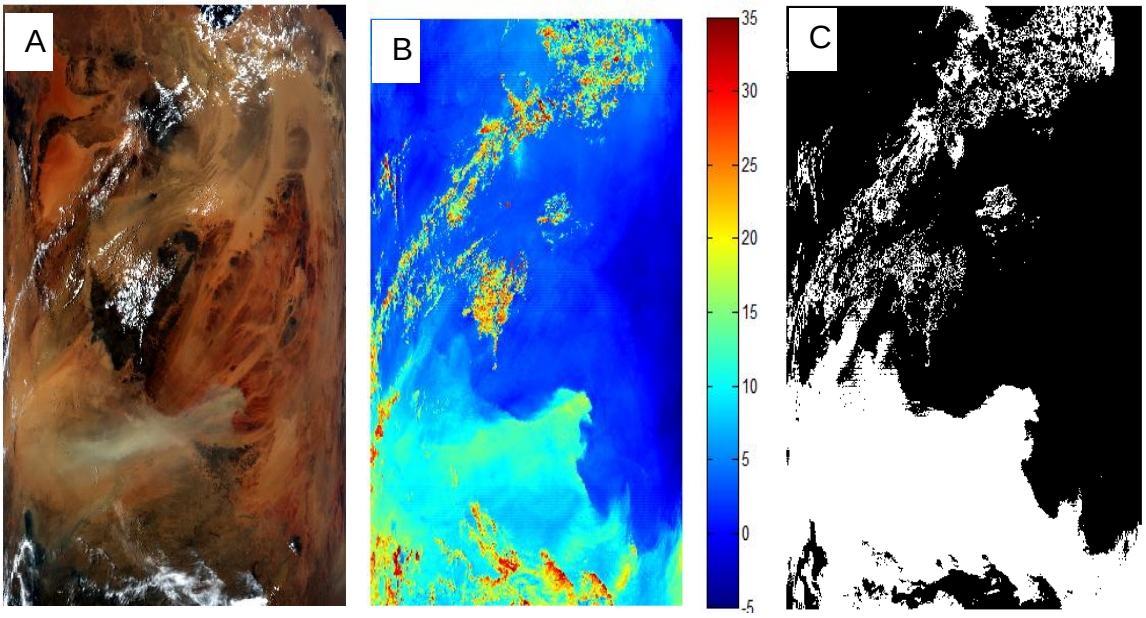

Figure 3-14 (A) is the true colour image for data number 7 in Table 3.3 captured by MODIS (Aqua) on 29th of May 2004 at 12:30 GMT over Chad, (B) is the corresponding BTD between bands 23 and 31 and (C) is the corresponding binary image showing dust storm detection .

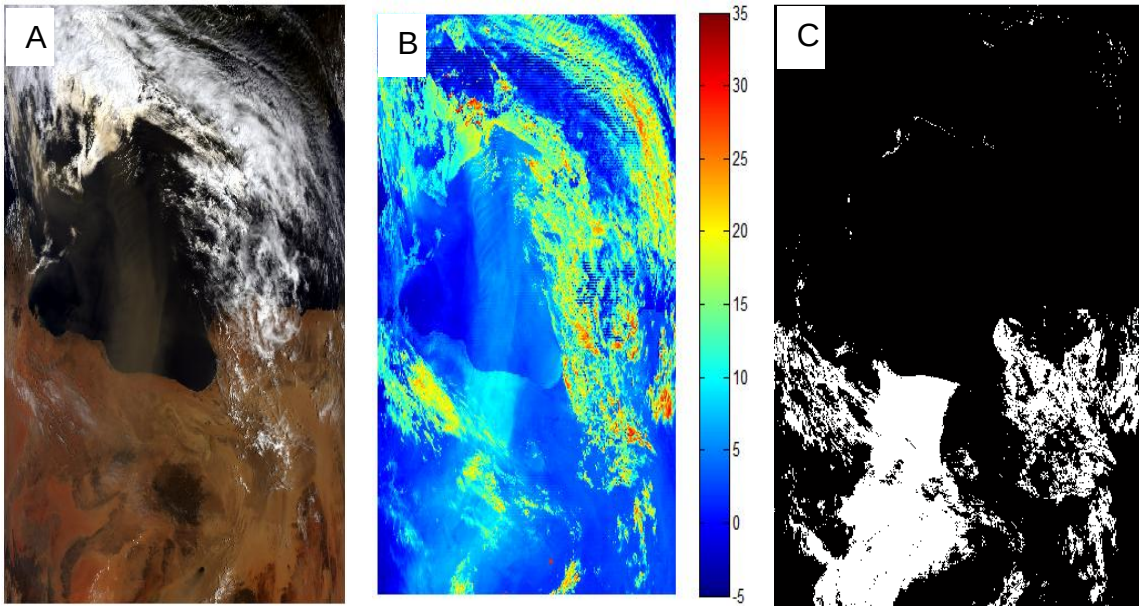

Figure 3-15 (A) is the true colour image for data number 26 in Table 3.3 captured by MODIS (Terra) on 8th of May 2002 at 09:35 GMT over Libya, (B) is the corresponding BTD between bands 23 and 31 and (C) is the corresponding binary image showing dust storm detection .

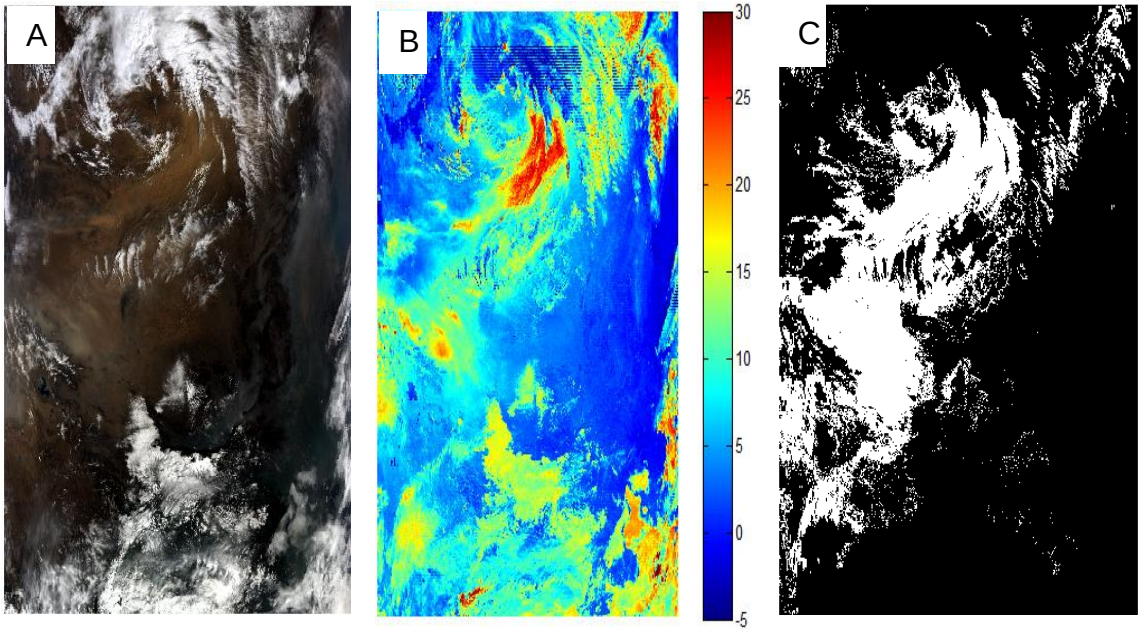

Figure 3-16 is the true colour image captured by MODIS (Terra) on 26th of March 2004 at 03:40 GMT over China, (B) is the corresponding BTD between bands 23 and 31 and (C) is the corresponding binary image showing dust storm detection.

The accuracy of this method for the detection of dust storms over sandy surfaces was assessed using several standard measures (defined in equations

4-1 to 4-8 in Section 4.2.1), and with ground truth data provided by manual detection of dust storms using true colour images, as no other source of ground truth date was available. This method of generating ground truth data was also used by some of the authors [38, 56] mentioned in Chapter 2. This method shows a True Positive Rate (TPR) of about 82% for dust storms pixels was achieved and about 18% False Negative Rate (FNR) were missing. However, there was about 14% False Discovery Rate (FDR) of cloud and other surface pixels were falsely detected as dust storm. Table 3.4 shows average and standard deviation (STD) values of the standard measures used to assess the accuracy of dust storm detection for all the data used in Table 3.3. Figure 3.17 shows a chart of the average and STD measurements in Table 3.3, used for validation of the dust storms detection method over all the Sahara data. The implementation of threshold method for dust storms over China is less effective for dust storms detection (TPR of 78%). However, the false detection of non dust storm pixels is better than over the Sahara. Here the average percentage of the true dust storms pixels over all pixels that are detected as dust storm Positive Predictive Rate (PPV) of 33% is less than over the Sahara, which means just 33% of pixels detected as dust storm are true dust. Table 3.5 and Figure 3.18 present results for the same measurements as for the Sahara implemented over China.

Table 3-4 Validation of the threshold method over the Sahara using several measures: true positive rate (TPR), false positive rate (FPR), true negative rate (TNR), false negative rate (FNR), accuracy (ACC), positive predictive value (PPV), negative predictive value (NPV) and false discovery rate (FDR)

	TPR	FPR	TNR	FNR	ACC	PPV	NPV	FDR
Average	0.816	0.146	0.859	0.183	0.860	0.383	0.979	0.616
STD	0.178	0.099	0.099	0.178	0.082	0.186	0.029	0.186

As can be seen from Table 3.4 the value of PPV is low and the value of FDR is high and that is because the sizes of most dust storms in the images are small.

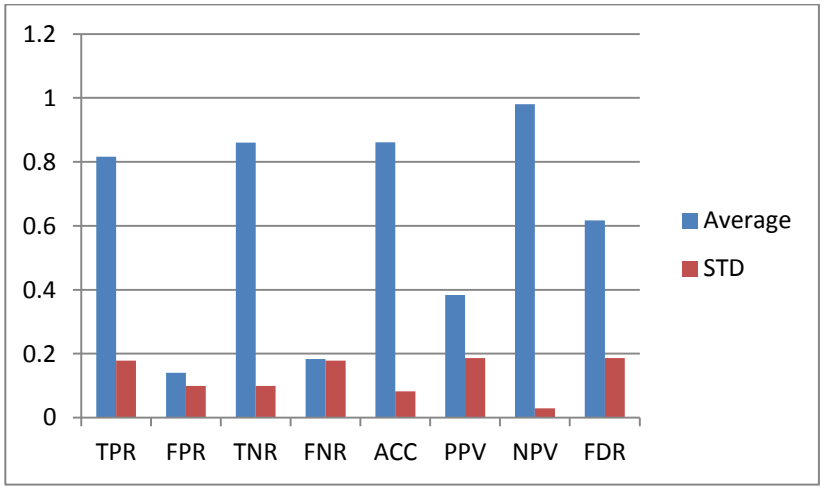

Figure 3-17 The average and the standard deviation results of the validation measurements over the Sahara

Table 3-5 Validation of the threshold method over China using several measures: true positive rate (TPR), false positive rate (FPR), true negative rate (TNR), false negative rate (FNR), accuracy (ACC), positive predictive value (PPV negative predictive value (NPV) and false discovery rate (FDR)

	TPR	FPR	TNR	FNR	ACC	PPV	NPV	FDR
Average	0.782	0.109	0.890	0.217	0.885	0.338	0.985	0.661
STD	0.197	0.075	0.075	0.197	0.072	0.182	0.014	0.182

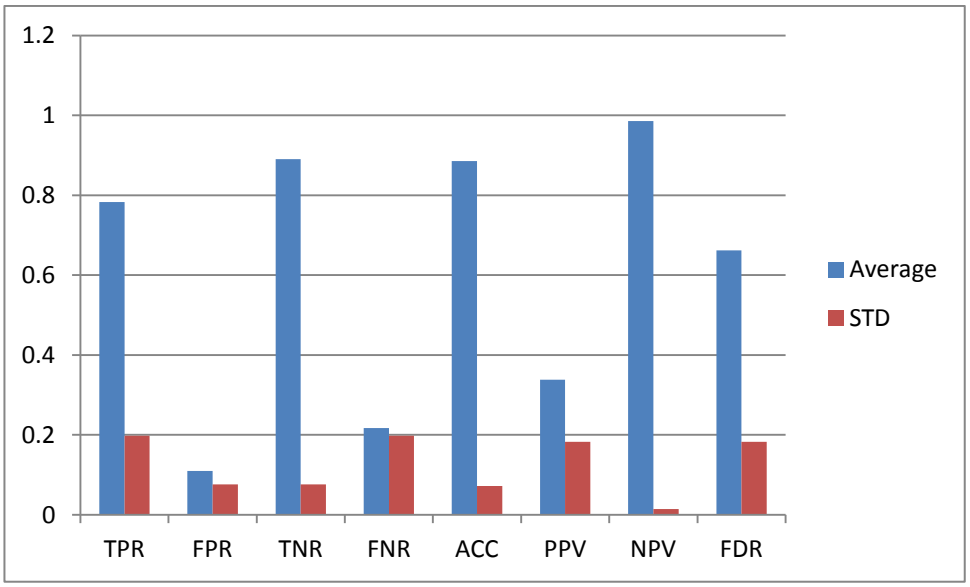

Figure 3-18 The average and the standard deviation results of the validation measurements over China

The threshold method was also applied to dust storms over water surfaces, which shows this method is not effective for dust storms detection over water. This is because the brightness temperature difference of light dust storms is less than 5.5K and the values of water in the normalized difference dust storm index are zero or less. Table 3.6 and Figure 3.19 show the average and the standard deviation results for applying this method over sea surfaces.

Table 3-6 Validation of the threshold method over sea surfaces using several measures: true positive rate (TPR), false positive rate (FPR), true negative rate (TNR), false negative rate (FNR), accuracy (ACC), positive predictive value (PPV), negative predictive value (NPV) and false discovery rate (FDR)

	TPR	FPR	TNR	FNR	ACC	PPV	NPV	FDR
Average	0.191	0.072	0.927	0.808	0.847	0.237	0.901	0.762
STD	0.203	0.077	0.077	0.203	0.087	0.183	0.060	0.183

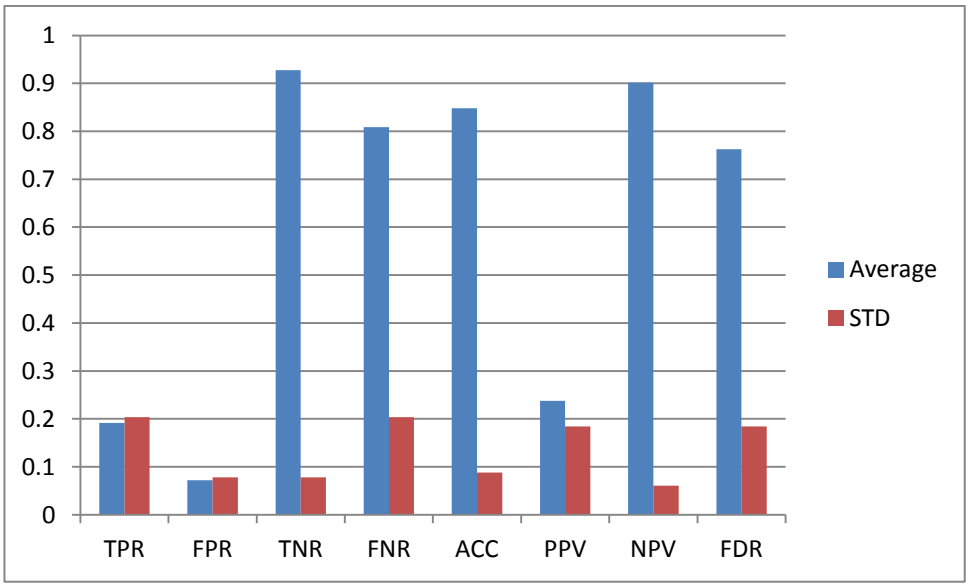

Figure 3-19 The average and the standard deviation results of the validation measurements over sea surfaces.

3.3. NIGHT AND DAY TIME DUST STORM DETECTION

The brightness temperature difference between bands 31 and 32 BTD(31-32) has been used to distinguish between clouds and dust storms. However, using this BTD alone is not enough to detect dust storms over sandy land as they share some characteristics. At the same time, this method with a 0K threshold is useful for detecting dust storm from cloud. In addition, the brightness temperature difference between bands 23 and 31 BTD(23-31) was effective for the detection of dust storm over sandy land as explained in the previous section. For this reason, in this section, both brightness temperature differences BTD(23-31) and BTD(31-32) are used for detecting dust storm over land and sandy land. Figure 3.19 illustrates the methodology of this technique.

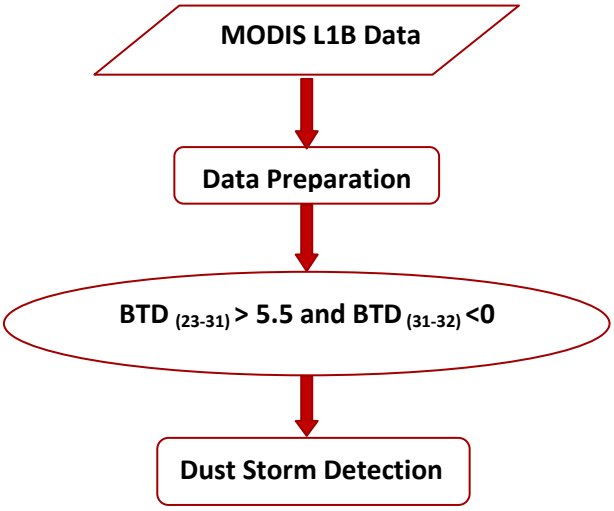

Figure 3-20 Flow chart of the proposed technique for Dust Storm detection

This method has been applied to all the Saharan data in Table 3.3 and it has been found by the author of this thesis that it can detect dust storms during the day better than the method in section 3.2. It is more effective in reducing the false detection of non-dust storms pixels as can be seen in Table 3.7, the values of FDR are smaller than the FDR Table 3.4, and the PPV value is higher, meaning more of the pixels detected are dust pixels. Also the standard deviations in all the fields are smaller, which means the results of applying the threshold method are similar for all the data in Table 3.3. Table 3.7 and Figure 3.21 show the average and standard deviation results of applying this method to all the Saharan data in Table 3.3. Figures 3.22 to 3.25 show some examples of applying this method over the Sahara desert.

Table 3-7 Validation of the threshold method over the Sahara using several measures: true positive rate (TPR), false positive rate (FPR), true negative rate (TNR), false negative rate (FNR), accuracy (ACC), positive predictive value (PPV), negative predictive value (NPV) and false discovery rate (FDR)

	TPR	FPR	TNR	FNR	ACC	PPV	NPV	FDR
Average	0.760	0.042	0.957	0.239	0.941	0.675	0.974	0.324
STD	0.167	0.039	0.039	0.167	0.039	0.210	0.0291	0.210

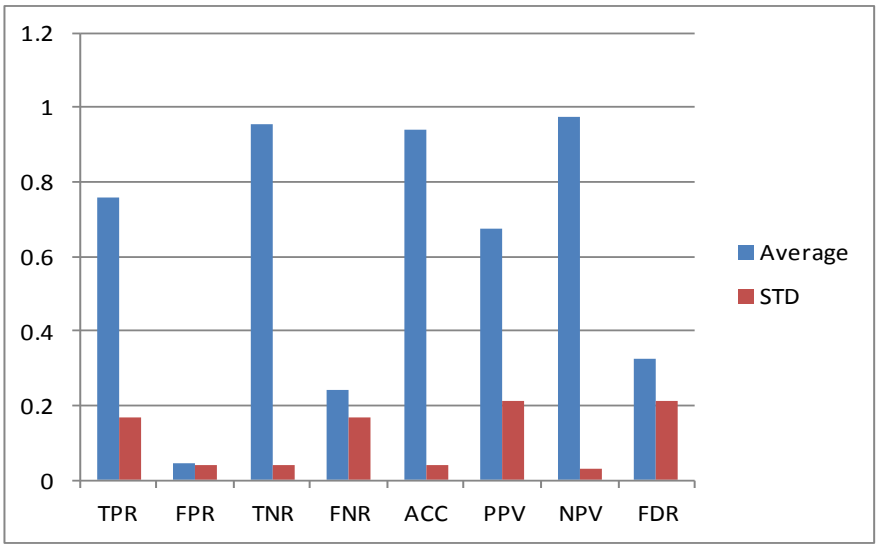

Figure 3-21 The average and the standard deviation results of the validation measurements over Sahara surfaces

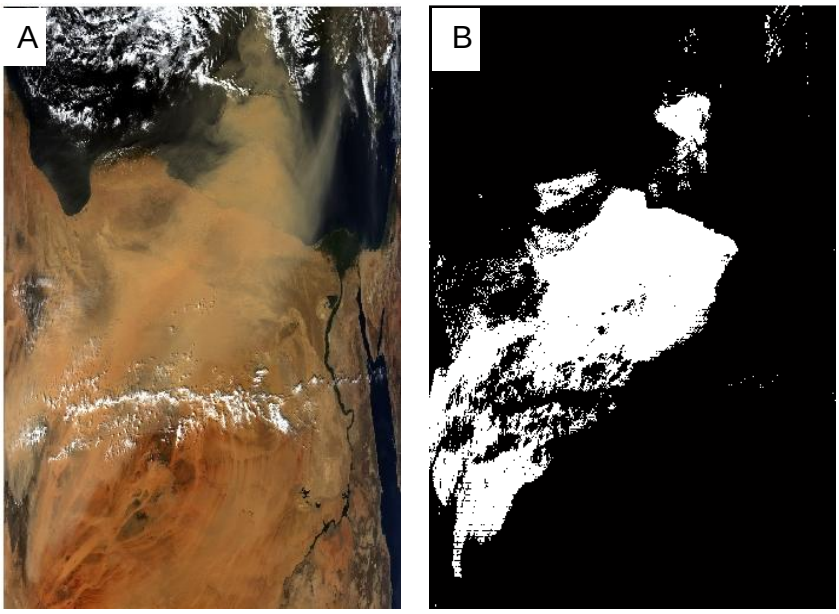

Figure 3-22 (A) is the true colour image for data number 8 in Table 3.3 captured by MODIS (Aqua) on 24th of February 2006 at 11:30 GMT over north Africa (B) is the corresponding binary image showing dust storm detection

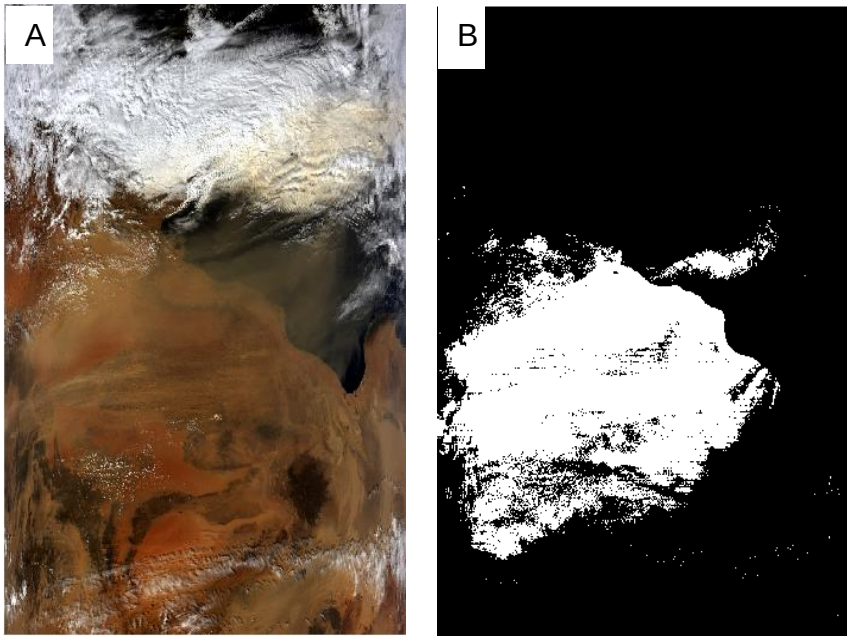

Figure 3-23 (A) is the true colour image for data number 6 in Table 3.3 captured by MODIS (Aqua) on 1st of March 2006 at 12:20 GMT over Libya, (B) is the corresponding binary image showing dust storm detection

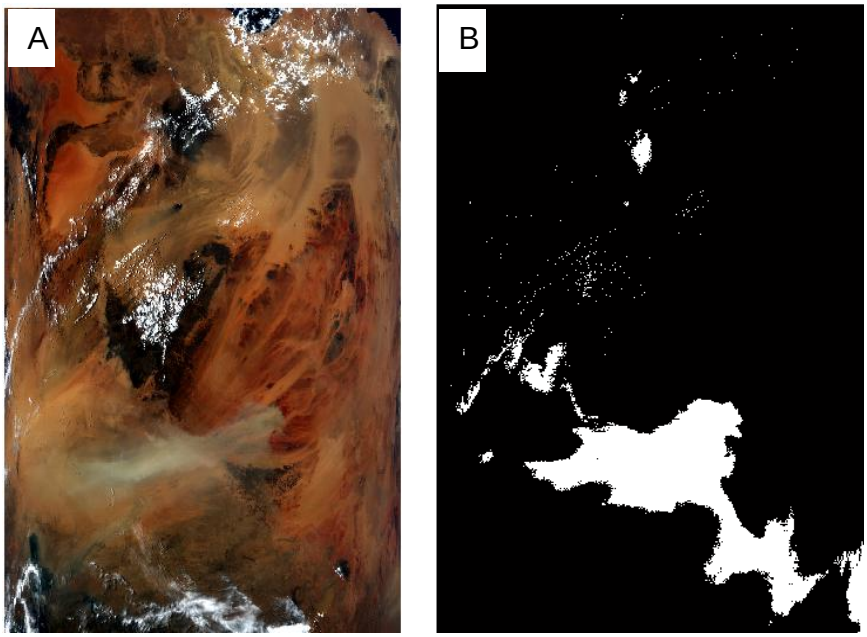

Figure 3-24 (A) is the true colour image for data number 7 in Table 3.3 captured by MODIS (Aqua) on 29th of May 2004 at 12:30 GMT over Chad, (B) is the corresponding binary image showing dust storm detection

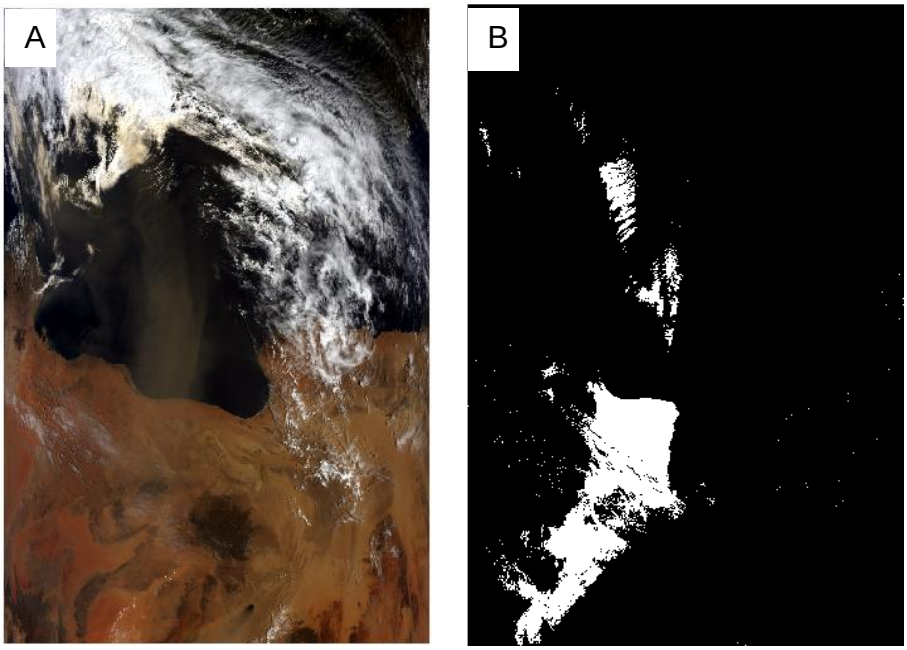

Figure 3-25 (A) is the true colour image for data number 26 in Table 3.3 captured by MODIS (Terra) on 8th of May 2002 at 09:35 GMT over Libya, (B) is the corresponding binary image showing dust storm detection

This method has also been applied to data for dust storms over China used in some publications and for other events occurring in 2011 over China. It

has been found that this method is much better than the method used in section 3.2 for dust storms detection over non-sandy lands, and is better when used over sandy land. Table 3.8 and Figure 3.26 show the average results of applying this method to dust storms over China. The standard deviations results for all data are similar. Figure 3.27 (A) shows an example dust storm over China and (B) shows the results of applying this method.

Table 3-8 Validation of the threshold method over China using several measures: true positive rate (TPR), false positive rate (FPR), true negative rate (TNR), false negative rate (FNR), accuracy (ACC), positive predictive value (PPV), negative predictive value (NPV) and false discovery rate (FDR)

	TPR	FPR	TNR	FNR	ACC	PPV	NPV	FDR
Average	0.794	0.085	0.914	0.205	0.908	0.409	0.986	0.590
Standard Deviation	0.184	0.066	0.066	0.184	0.060	0.177	0.013	0.177

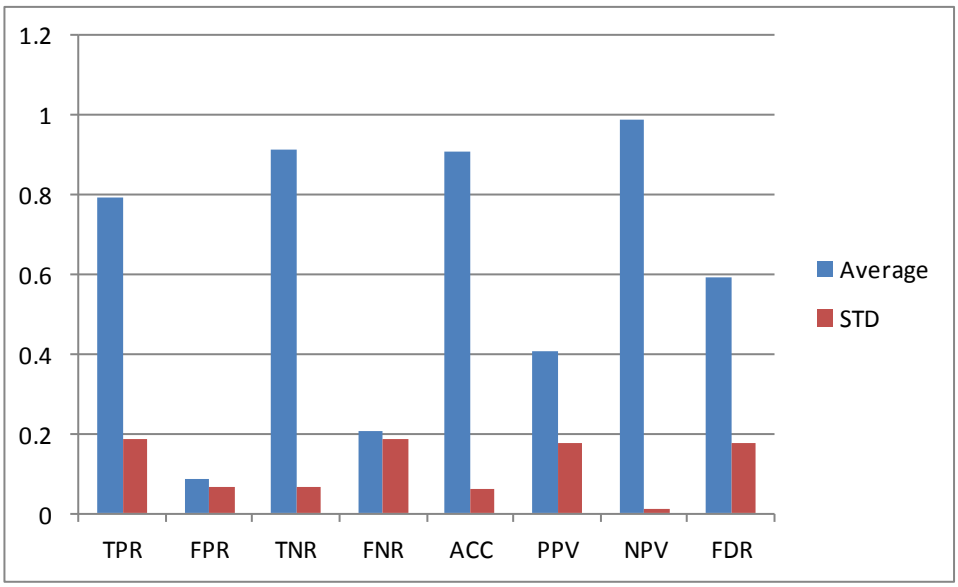

Figure 3-26 the average and the standard deviation results of the validation measurements over China

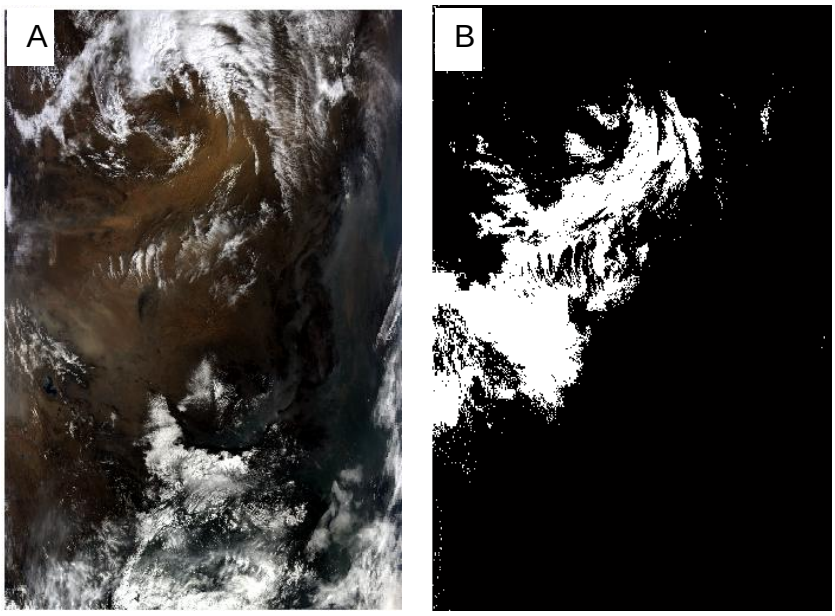

Figure 3-27 (A) is the true colour image of a dust storm captured by MODIS (Terra) on 26th of March 2004 at 03:40 GMT China, (B) is the corresponding binary image showing dust storm detection

From the previous tables and figures it can be clearly seen that dust storms can be detected using both BTDs. This technique can detect 79% of dust storms over land when BTD (31-32) is less than 0K with 8% of false detection, while 74% of dust storm can be detected with just 4% of false detection when BTD (31-32) of less than -1K is used. However, this technique has some limitations for detecting weak dust storms over land as shown in Figure 3.24, and thick dust storms over water as shown in figures 3.22, 3.23 and 3.25, because of the use of BTD (23-31) with a 5.5K threshold, whereas the threshold less than 5.5K leads to the false detection of some of land and cloud as dust storm. This method can also be used to detect dust storms during the night-time, as both BTDs use the emissive bands. However, for detecting dust storms during the night, the previous threshold is not appropriate as the temperature drops at night and this leads to the difference dropping as well.

Thus, for the detection of dust storms at night, the -1k threshold is used with the BTD (23-31). Table 3.9 and Figure 3.28 show the average and the standard deviation of the results of applying this method during the night.

Table 3-9 Validation of the threshold method during night over sandy land using several measures: true positive rate (TPR), false positive rate (FPR), true negative rate (TNR), false negative rate (FNR), accuracy (ACC), positive predictive value (PPV), negative predictive value (NPV) and false discovery rate (FDR)

	TPR	FPR	TNR	FNR	ACC	PPV	NPV	FDR
Average	0.672	0.019	0.980	0.327	0.956	0.789	0.972	0.210
Standard Deviation	0.032	0.019	0.019	0.032	0.020	0.149	0.004	0.149

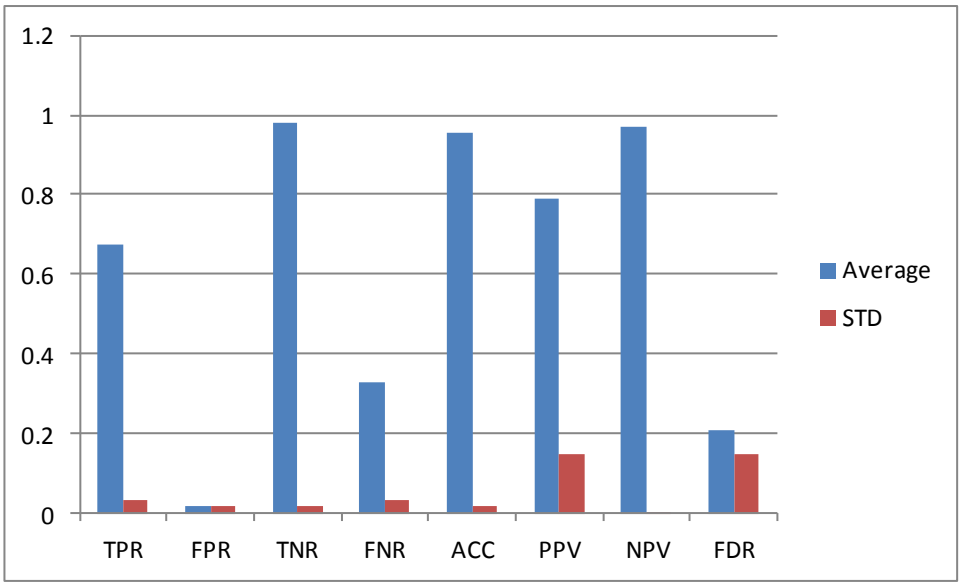

Figure 3-28 the average and the standard deviation results of the validation measurements over sandy land during the the night

Figures 3.29 to 3.31 illustrate the application of this method to the dust storms detected in the north of Saudi Arabia on both the day and night of 12th of May 2005 at 23:35 GMT, which continued for 3 days.

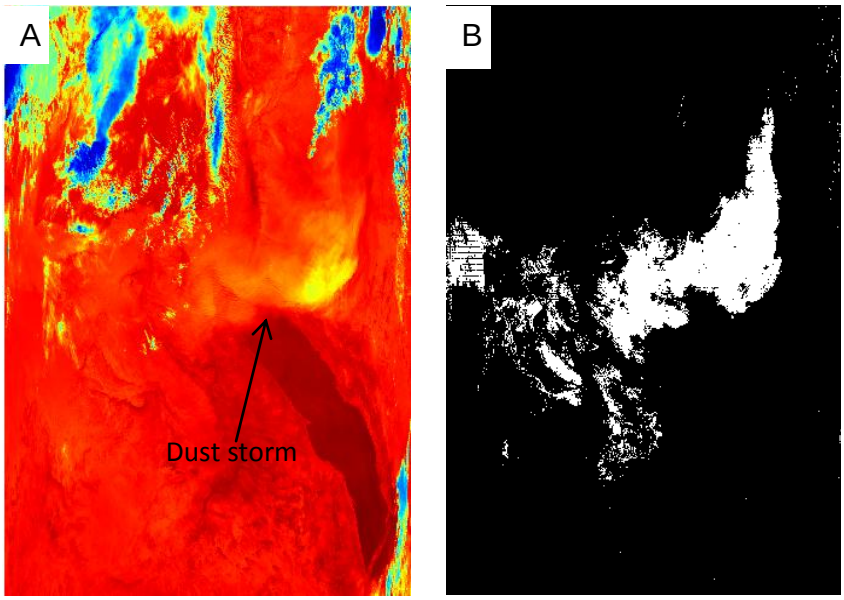

Figure 3-29 (A) is the brightness temperature image for band 31 of the dust storm event which occurred on 12th of May 2005 at 23:35 over the north of Saudi Arabia, (B) is the corresponding binary image showing dust storm detection

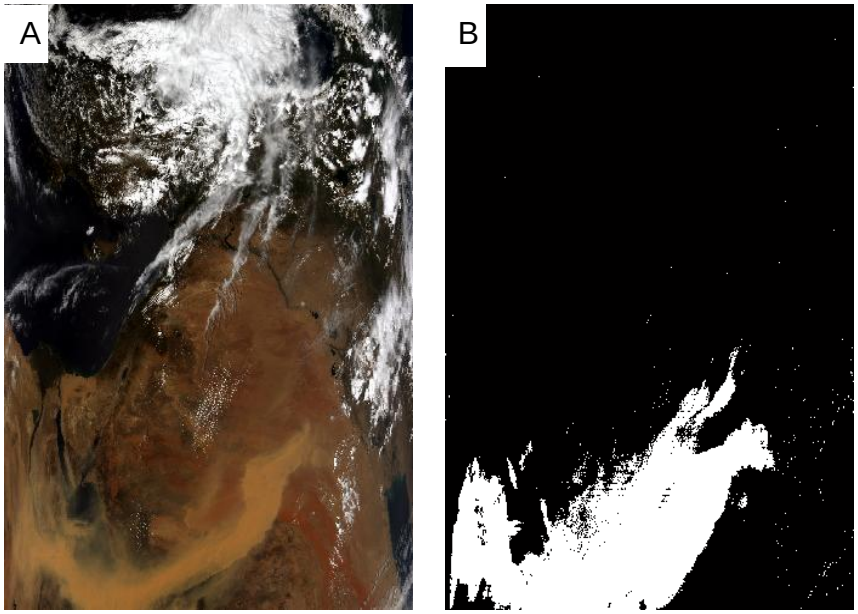

Figure 3-30 (A) is the colour image of the continuing dust storm event shown in Figure 23 which occurred on 13th of May 2005 at 10: 35, (B) is the corresponding binary image showing dust storm detection

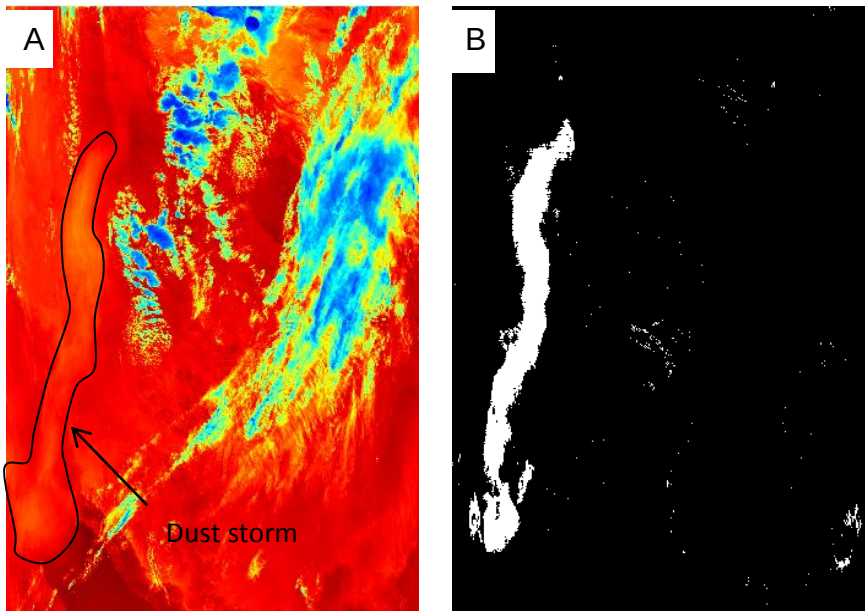

Figure 3-31 (A) is the brightness temperature image for band 31 of the dust storm event which occurred on 13th of May 2005 at 22:40 over the north of Saudi Arabia, (B) is the corresponding binary image showing dust storm detection

This method has some limitations in that weak dust storms over water will not be detected and different thresholds need to be used to detect dust storms during day and night times.

3.4. CHAPTER CONCLUSIONS

Dust storms over different surfaces can be detected using two threshold methods. The first uses the brightness temperature difference BTD (23 - 31) with normalized difference dust index (NDDI). The BTD (23 - 31) is used to distinguish dust storm and cloud from other surface content and the NDDI is used for separating dust storm from cloud. The results show this method for detecting dust storms was effective. However, it has limitations in that some low clouds and shadow are detected as dust with a dust storm. Also, this method has limitations when detecting weak dust storms over water, and for the detection of dust storms at night because of the use of the NDDI.

The second method uses both BTD (23 – 31) and BTD (31 – 32) with thresholds of 5.5K and 0K respectively. The results show that this method is much better than the method in section 3.2 for dust storm detection over land and sandy land by reducing the false detection of non-dust storms pixels. However, this method is also limited for dust storms detection over water. The biggest advantage of this method is that it can be used for the detection of dust storms during the night. However, during the night, a threshold of -1K for both BTDs is used. Thus, there is a need to improve the detection of a dust storm over water, and for generating an automated method that can detect dust storms over different surfaces at both day and night. Chapter 4 describes the use of an Artificial Feed-Forward Back-Propagation Neural Network for dust storms detection, attempting to address some of these problems.

CHAPTER FOUR

4. DUST STORM DETECTION USING A NEURAL NETWORK

4.1. INTRODUCTION

To tackle the limitations of the methods introduced in Chapter 3, neural networks are used for the detection of dust storms in this chapter. Neural networks are computer systems that attempt to work similarly to the human brain by using electronic components analogous to biological neurons. One of the operations that neural networks can do is pattern classification [57]. Neural networks have a massively parallel distributed structure and the ability to learn and so can produce reasonable outputs for inputs not encountered during training. These two features make neural networks potentially useful solutions to complex problems [58]. There are a number of neural networks topologies. In this work, Feed-Forward Back-Propagation Neural Networks (FFNN) have been adopted to investigate the detection of dust storms using MODIS images. FFNN is defined as a neural network that uses more than one node and contains no feedback paths [59]. There are two different types of feed-forward neural networks:

4.1.1. SINGLE LAYER FEED-FORWARD

In this structure there is only one input layer and one output layer, and the number of nodes used in these layers depends on the application [59].

4.1.2. MULTI LAYER FEED-FORWARD

This structure is similar to the single layer feed-forward structure except it has multiple extra (hidden) layers connected between the input layer and the output layer [59].

Neural Networks are widely used in many applications, such as data mining and classifying data, such as vegetation and other land cover-obtained from satellites. The FFNN has been shown to provide effective performance in classifying satellite images. Gao et al. [35] made a comparison of feed-forward Neural Networks based classifiers using individual pixels and prior segmented regions as the objects to be classified. The performances of a Probabilistic Neural Network (PNN) and a Maximum Likelihood classifier (ML) were compared for dust storm detection over the United States using MODIS bands 20, 29, 31, and 32. The result of this study shows the PNN is much better than the ML for detecting dust storms, with accuracies of detecting dust storms of 84% and 67% respectively [60].

This chapter is organised as follows. Section 4.2 describes the use of FFNN for dust storm detection during the day using reflectance bands and two brightness temperature differences. Section 4.3 introduces the FFNN for dust storm detection during both day and night using features generated from four brightness temperature differences. Section 4.4 describes the use of the FFNN to generate a dust storm mask. Section 4.5 presents the conclusions of this chapter.

4.2. DAYTIME DUST STORM DETECTION

Many previous studies have concentrated on detecting dust storms during the day over different region using different techniques. However, no one

has provided effective results for dust storm detection over sandy land. Also, the threshold methods use fixed value thresholds, but these are different for weak or intense dust storms. For these reasons a feed-forward back propagation network has been proposed to classify pixels to detect dust storms from weak to intense.

4.2.1. FEATURE SELECTION

The feature vector inputs used for the neural network are pixel samples of dust storm, land, cloud, water, and vegetation extracted from multi-spectral MODIS bands 1, 3 and 4, the BTD used in [61] and the BTD used in [7], as shown in Figure 4.1. MODIS bands 1, 4, and 3 correspond to the components which can be used to construct true colour images showing white for cloud and black for water. Sand and land are both shown similarly as shades of brown with areas of vegetation as green. The true colour images enable cloud, land, water, and vegetation areas to be distinguished, while the BTD between bands 23 and 31 is used to distinguish between dust storm and land, and the BTD between bands 31 and 32 is used to distinguish between dust storm and cloud.

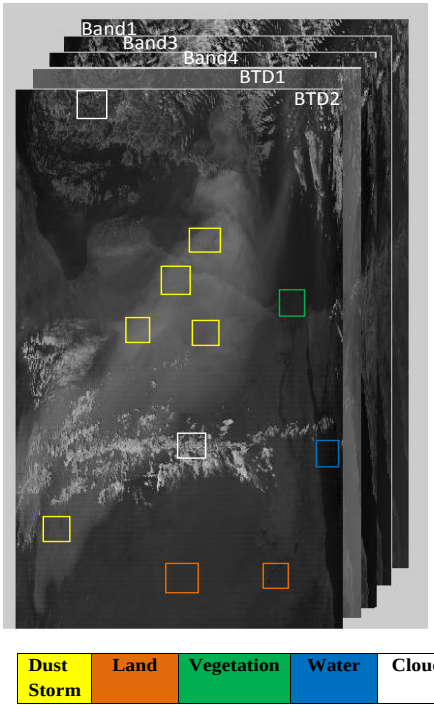

Figure 4-1 Sampling of the five classes from the three band images and two BTD images generated from row 8 of Table 3.3 in Chapter 3.

4.2.2. EXPERIMENTAL VALIDATION

The training and testing of the neural network proceeds by first selecting samples for the five different objects of interest from the three bands and the two BTDs, as illustrated in Figure 4.1. A total of 135,000 data components extracted from 27 images were used in this study for training and testing the neural network. Table 4.1 shows sample rows of data that were used for training and testing the Neural Network, where rows 1-3 correspond to the pixels from the “dust” class and rows 4 - 8 correspond to pixels from the “no-dust” class chosen from pixels representing Land, Vegetation, Cloud, and Water.

Table 4-1 A small sample of the data used for training and testing the Neural Network. Numbers in columns 1 to 3 are reflectance values and numbers in columns 4 and 5 are BTD values. The class values 0.9 and 0.1 correspond to "dust storm" and "not dust storm", respectively.

Band1	Band3	Band4	BTD1	BTD2	Class
0.3765	0.2245	0.293	10.891	-2.222	0.900
0.3698	0.2215	0.288	11.403	-2.237	0.900
0.3529	0.2144	0.276	10.914	-2.190	0.900
0.3006	0.1322	0.1804	2.3116	-0.554	0.100
0.2965	0.1303	0.1769	2.3721	-0.571	0.100
0.2884	0.1279	0.1704	2.3253	-0.583	0.100
0.0501	0.1455	0.0794	-3.447	1.0106	0.100
0.0497	0.1451	0.0791	-3.400	0.9411	0.100

The extracted data were randomly divided into two sets, with 60% of data used for training the neural network and 40% used for testing. The FFNN had five input nodes, twenty hidden nodes and two output nodes. This number of hidden nodes is the default number of FFNN recommended by MATLAB. Figure 4.2 illustrates the structure of the FFNN.

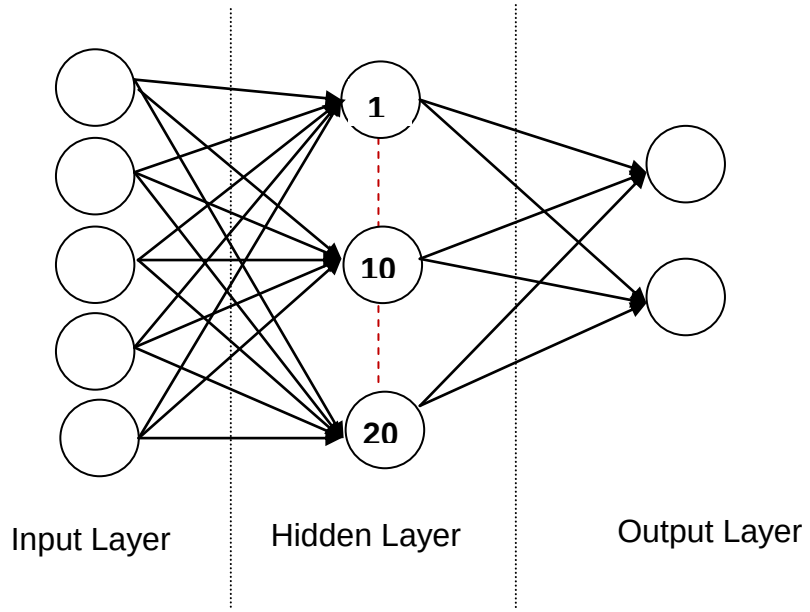

Figure 4-24 Feed- Forward Neural Network Structure

The Cross validation method was used in this work to avoiding over fitting. The division of data is repeated ten times, each time generating different

training and testing subsets to train the neural network and determine the prediction performance measures. Then the average and standard deviation values are generated from the repeated prediction measures. When a training process is finished, the resulting neural network uses the 40% testing data set without classes to predict the classes; the predictions are compared with the actual classes to determine the prediction performance measures. Figure 4.3 illustrates the strategy of using cross validation method in the FFNN algorithm.

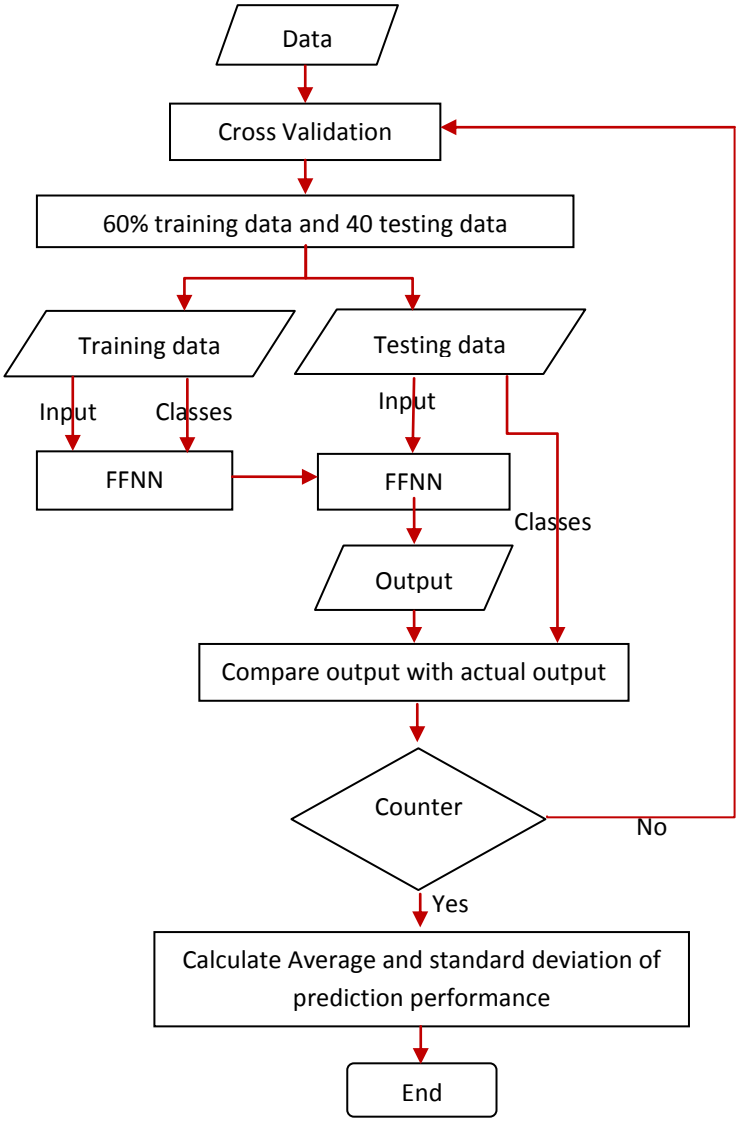

Figure 4-3 A flowchart of the FFNN algorithm using cross validation

A threshold of 0.5 is used to classify the output of the FFNN, with an output greater than 0.5 classified as a dust storm and an output less than or equal 0.5 classified as a non-dust storm. The performance of the FFNN is evaluated by comparing the output from the test data with the correct outputs and calculating the four measures: True positive (TP), False Positive (FP), True Negative (TN) and False Negative (FN). These measures are explained in more detail below:

- TP indicates the number of pixels that are dust storm and correctly predicted to be dust storm.
- FP indicates the number of pixels that are not dust storm but are falsely predicted to be dust storm.
- TN indicates the number of pixels that are not dust storm and are correctly predicted as not dust storm.
- FN indicates the number of pixels that are dust storm but falsely predicted as not dust storm.

Then to quantify the prediction performance of the FFNN some standard forecasting measures is calculated from the four previous measures. These forecasting measures are:

- True Positive Rate (TPR), also known as Sensitivity, is the percentage of dust storm pixels that are successfully predicted to be dust storm pixels. Higher TPR referring to a better prediction performance. TPR is calculated using equation 4-1.

$$TPR = \sum TP / \sum (TP + FN) \qquad \text{Equation 4-1}$$

- False Positive Rate (FPR) is the percentage of non-dust storm pixels that are falsely predicted to be dust storm pixels. Lower FPR indicates better performance. FPR is calculated using Equation 4-2.

$$FPR = \sum FP / \sum (FP + TN) \quad \text{Equation 4-2}$$

- True Negative Rate (TNR) is the percentage of non-dust storm pixels that are successfully predicted to be non-dust storm pixels. Higher TNR indicates better performance. TNR is calculated using Equation 4-3.

$$TNR = \sum TN / \sum (TN + FP) \quad \text{Equation 4-3}$$

- False Negative Rate (FNR) is the percentage of dust storm pixels that are falsely predicted as non-dust storm pixels. Lower FNR indicates better performance. FNR is calculated using Equation 4-4.

$$FNR = \sum FN / \sum (FN + TP) \quad \text{Equation 4-4}$$

- Accuracy (ACC) indicates how close the overall predicted outputs are to the true outputs. Higher FNR indicates better performance. ACC is calculated using Equation 4-5.

$$ACC = (\sum TP + TN) / \sum (TP + FP + TN + FN) \quad \text{Equation 4-5}$$

- Positive Predictive Value (PPV) is the percentage of dust storm pixels correctly predicted to be dust storm compared with the overall dust storm predicted values. Higher PPV indicates better performance. PPV is calculated using Equation 4-6.

$$PPV = \sum TP / \sum (TP + FP) \quad \text{Equation 4-6}$$

- Negative Predictive Value (NPV) presents the percentage of non-dust storm pixels correctly predicted as non-dust storm compared with the overall non-dust storm predicted values. Higher NPV indicates better performance. NPV is calculated using Equation 4-7.

$$NPV = \sum TN / \sum (TN + FN) \qquad \text{Equation 4-7}$$

- False Discovery Rate (FDR) presents the percentage of non-dust storm pixels falsely predicted to be dust storm compared with the overall dust storm predicted values. Lower FDR indicates better performance. FDR is calculated using Equation 4-8.

$$FDR = \sum FP / \sum (TP + FP) \qquad \text{Equation 4-8}$$

Here ΣTP and ΣTN are the numbers of true positive and true negative pixels respectively and ΣFP and ΣFN are the numbers of false positive and false negative pixels respectively. These forecasting measures are not all independent. From the definitions it follows that: FPR + TNR = 1, TPR + FNR = 1 and PPV + FDR = 1.

Table 4.2 and Figure 4.4 show the average and STD results for the forecasting measures after training and testing the FFNN machine learning algorithm ten times.

Table 4-2 The average and the standard deviation results of the forecasting measures after training and testing the FFNN ten times

	TPR	FPR	TNR	FNR	ACC	PPV	NPV	FDR
Average	0.9995	0.0002	0.9997	0.0004	0.9996	0.9996	0.9996	0.0003
STD	0.0001	0.0001	0.0001	0.0001	0.0000	0.0001	0.0001	0.0001

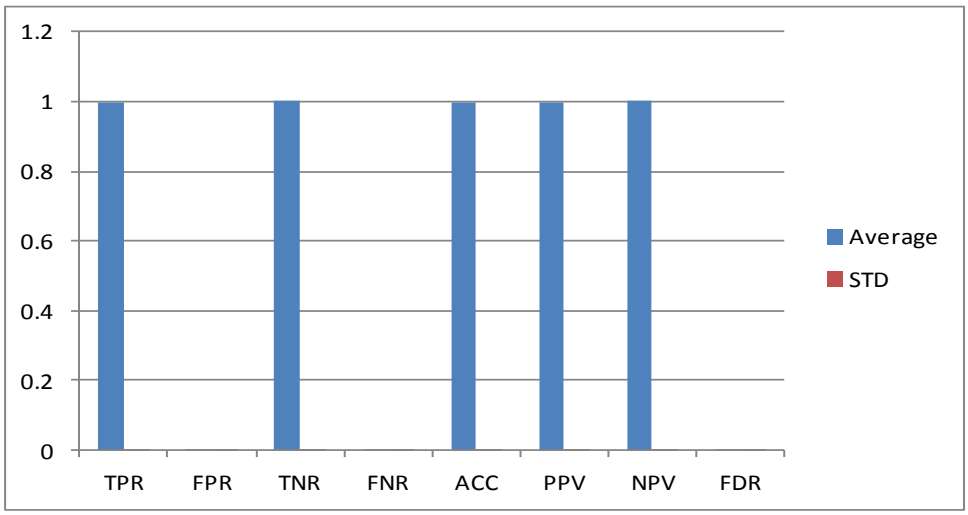

Figure 4-4 The average and the standard deviation results of the forecasting measures after training and testing the FFNN ten times

Table 4.2 and Figure 4.4 shows that the average values of TPR, TNR, ACC, PPV and NPV are very high at 0.999 and the average values of FPR, FNR, and the FDR are very low, which means FFNN method is very useful for predicting dust storm pixels. The small STD values show that the repeated results are close to each.

After the training and testing of the FFNN, the trained network was applied to new MODIS images acquired by the Terra and Aqua satellites over Africa and listed in Chapter 3 together with dust storms events which occurred in 2011 and which are classified by the Earth Observatory as dust storm images (http://earthobservatory.nasa.gov/NaturalHazards/). The accuracy of this approach was assessed using several standard measures for each image, with ground truth data provided by manual detection of dust storms using true colour images. The average results for all the dust storm images are displayed in Table 4.3 where they are also compared with the latest technique (TIIDI) used for detection dust storms over bright surface used in reference [39]. It is

apparent that the Neural Network based approach is much better for the detection of dust storms over the Sahara desert and this is also the case for the Gobi desert, as may be seen in Table 4.4.

Table 4-3 Comparison of standard measure averages obtained applying the FFNN and TIIDI methods over the Sahara

Method	TPR	FPR	TNR	FNR	ACC	PPV	NPV	FDR
FFNN	0.80	0.02	0.97	0.19	0.94	0.81	0.96	0.18
TIIDI	0.80	0.28	0.71	0.19	0.73	0.29	0.96	0.70

Table 4.3 shows that the TPR is the same in both methods which means the same number of dust storm pixels were detected as a dust storm. However, the values of TNR ACC and PPV from FFNN are higher than from TIIDI which means FFNN is better that TIIDI. Furthermore, FPR and FDR from FFNN are less than from TIIDI and that means the FFNN is also better at reducing the number of pixels that are unsuccessfully detected as dust storm pixels. Figure 4.5 shows an example of applying the FFNN and the TIIDI to a dusty image captured over the Sahara.

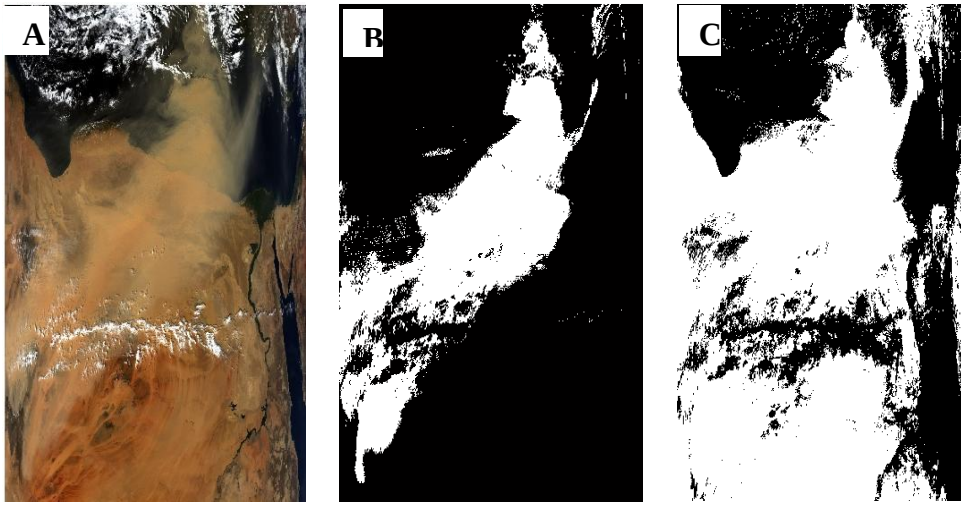

Figure 4-5 (A) shows the dust storm image for row 8 in Table 3, using the three true color bands, (B) is the result of dust storm detection using the trained Neural Network and (C) is the corresponding result from the technique used in reference [39].

The neural network system trained on the Saharan data was further tested by the detection of dust storms over China. It was found that these too can be detected, but with somewhat poorer performance than for the detection of dust storms over the Sahara desert, as summarised in Table 4.4 for comparison with Table 4.3. However, comparing these results with the results of the previous methods used in Chapter 3, these are better. Figure 4.6 shows an example of applying the FFNN over China compared with results from reference [39].

Table 4-4 Comparison of standard measure averages obtained applying the FFNN and TIIDI methods over the China.

Method	TPR	FPR	TNR	FNR	ACC	PPV	NPV	FDR
FFNN	0.86	0.11	0.88	0.13	0.88	0.33	0.98	0.66
TIIDI	0.87	0.32	0.67	0.12	0.68	0.15	0.98	0.84

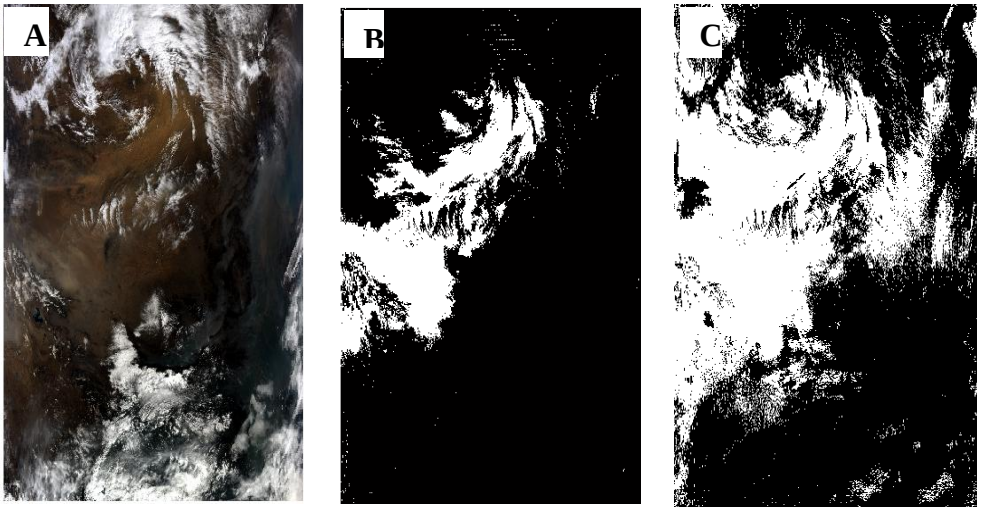

Figure 4-6 (A) is the true colour Aqua image of a dust storm over north China used in reference [1], (B) is the result of dust storm detection using the neural network, and (C) is the corresponding result from the technique used in reference [1].

This trained ANN has been further tested using all the events that occurred worldwide in 2011, which are classified by Earth Observatory as dust storm images (http://earthobservatory.nasa.gov/NaturalHazards/). Of the 96 dust

storm events, only 6 were not detected by the ANN, and all of these represent very weak dust storms.

4.3. NIGHT AND DAY DUST STORM DETECTION

The neural network method used in the previous section was useful for detecting dust storm over land, sandy land and water. Furthermore, it was able to extract dust storm from cloud with less misclassification. However, this method is limited to detecting dust storms at night. It is worth noting that the threshold method has its limitations for night detection, as the threshold is not constant from day to night. For this reason this section concentrates on detecting dust storm during both day and night using the neural network technique.

4.3.1. FEATURE SELECTION

The central of MODIS bands 20, 23, 29, 31, and 32 are the most commonly used thermal infrared channels for detecting dust storms. The brightness temperature differences between these bands can be used to identify dust storms from other objects in MODIS images. The brightness temperature difference between the 11 µm (b31) and the 12 µm (b32) bands has been employed in many dust storm detection schemes and its basic function is to isolate the cloud from dust storms [32]. Since the brightness temperature of dust storms in the 12 µm (band 32) is generally higher than the brightness temperature in the 11 µm (band 31), the values of dust storms in the brightness temperature difference between 11 µm and 12 µm will be negative, and most of the other objects will be around zero or positive [39]. Also the water

vapour absorption in the 8.6 μm (band 29) is higher than in the 11 μm (band 31) [2]. For this reason the brightness temperature difference between the 8.6 μm and the 11 μm will be positive. Liu et all [2] used the BTD(31-32) < 0 and BTD(29-31) > threshold for detecting dust storms at both day and night time. Yang and Ronggao [39] used the Thermal Infrared Integrated Dust Index (TIIDI) to detect dust storm over sandy, vegetation, and water surfaces. The brightness temperature difference of four MODIS bands is used to develop the TIIDI BTD(20-31), BTD(29-31), and BTD(32-31), where BTD(32-31) is used to distinguish cloud from other objects, BTD(29-31) is used to identify dust storm and surface sand, and BTD(20-31) is used to separate dark surface and represent the intensity of dust storm. The Brightness temperature difference BTD(23-31) used in Chapter 3 for separating dust storms and cloud from other surfaces. The Brightness temperature of band 31 is also used for distinguish between airborne dust and sandy ground.

In this section the Neural Network feed-forward back propagation technique is used to identify dust storms over different surface at both day and night. The training and testing features vectors used in this study are: pixel samples of cloud, dust storm, land, water, snow, and vegetation areas extracted from BTD(20-31), BTD(23-31), BTD(29-31), BTD(31-32), and the brightness temperature of band 31. A total of 160,000 components of data extracted from 27 images were used in this study, with 60% used for training and 40% for testing the neural network.

4.3.2. EXPERIMENTAL AND VALIDATION

The same steps used in section 4.2.2 to train and validate the result of the FFNN are also used in this section. The performance of the neural network is evaluated using the same standard measures used in section 4.3.1. Table 4.5 and Figure 4.7 show the average and STD values of the standard measured results.

Table 4-5 The average and the standard deviation results of the forecasting measures after training and testing the FFNN ten times

	TPR	FPR	TNR	FNR	ACC	PPV	NPV	FDR
Average	0.989	0.003	0.996	0.010	0.994	0.983	0.997	0.016
STD	0.002	0.000	0.000	0.002	0.001	0.004	0.000	0.004

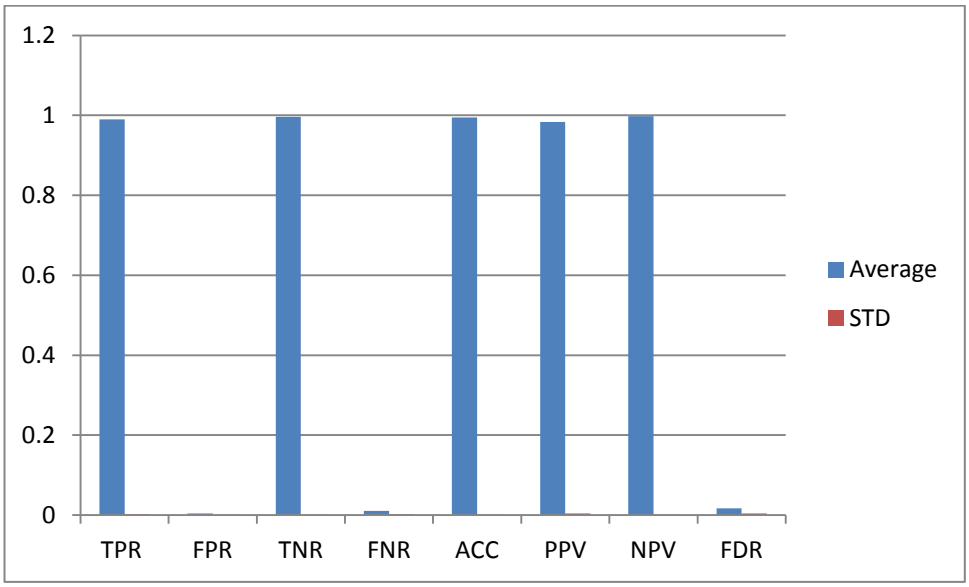

Figure 4-7 The average and the standard deviation results of the forecasting measures after training and testing the FFNN ten times

From Table 4.5 and Figure 4.7 it can be seen that the FFNN-based approach using the four brightness temperature differences, together with the brightness temperature of band 31, can be used for detecting dust storms at both day and night. This method has been applied to MODIS data from both the Terra and

Aqua satellites over bright, dark and ocean surfaces, for both day and night time images. The accuracy of this method has also been assessed using several standard measures. A manual detection of dust storms using the true colour bands was chosen to provide ground truth data during the day while the BTD (23-31) and the BT of band 31 were chosen to provide ground truth data during the night because no other source of ground truth date was available.

- **Dust Storm Detection over Bright Surfaces**

  The trained neural network was applied to all MODIS data corresponding to dust storms over the Sahara desert occurring in 2011, and classified by the Earth Observatory as dust storm images. **(http://earthobservatory.nasa.gov/NaturalHazards/).** The results are shown in Table 4.6. An average TPR value of 80% and an average FPR value of about 5% were found for dust storms. Also an average accuracy of about 93% was found. This shows that the method is useful for the detection of dust storms over deserts during the day. However, the average results of the positive predictive values and the false discovery rate are high, at about 56% and 43% respectively. The standard deviations of these two measures are also high, meaning the results fluctuated over a few percent. The reason, the PPV and FDR are high is because the sizes of dust storms in the images are very small compared to the remaining objects.

Table 4-6 The average and the standard deviation of the forecasting measures of applying FFNN over sandy land

	TPR	FPR	TNR	FNR	ACC	PPV	NPV	FDR
Average	0.796	0.057	0.943	0.204	0.931	0.569	0.977	0.431
STD	0.122	0.039	0.039	0.122	0.039	0.190	0.021	0.190

As an example of sandy land to which the FFNN was applied, Figure 4.8 (A) shows a true colour image of the dust storm event which occurred on 19th of July 2005 over the Sahara desert, captured by the Aqua satellite. Figure 4.9 (A) shows a similar true colour image of a huge dust storm over the north of Saudi Arabia and south of Jordan on 13th of May 2005, captured by the Aqua satellite. Figures 4.8 (B) and 4.9 (B) show the result of the dust storm detection algorithm for both events shown in figures 4.8 (A) and 4.9 (A) respectively. These results show that dust storms can be effectively separated from cloud and bright surface.

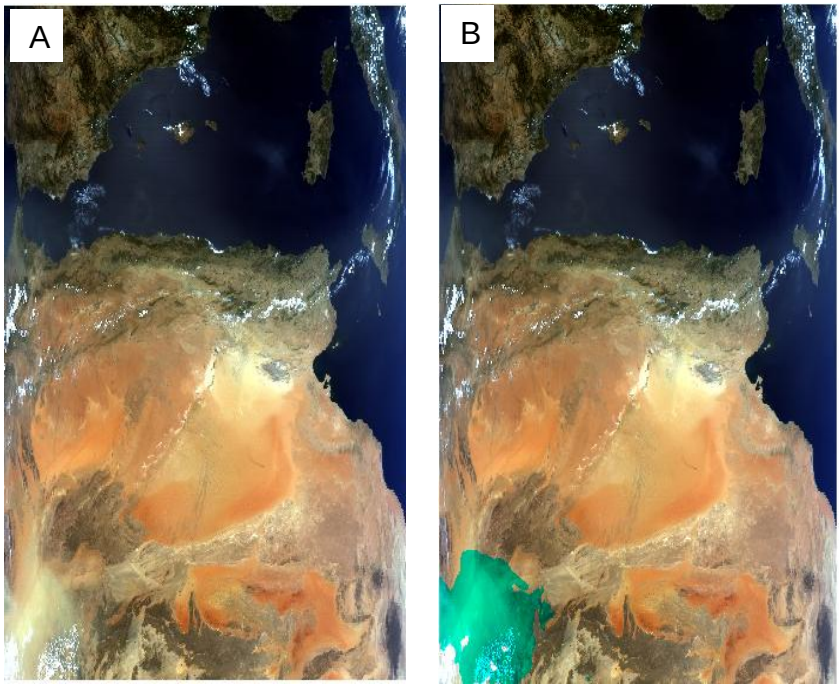

Figure 4-8 (A) is the true colour image of a Saharan dust storm captured by Aqua on 19th of July 2005 and (B) is its corresponding dust storm detection

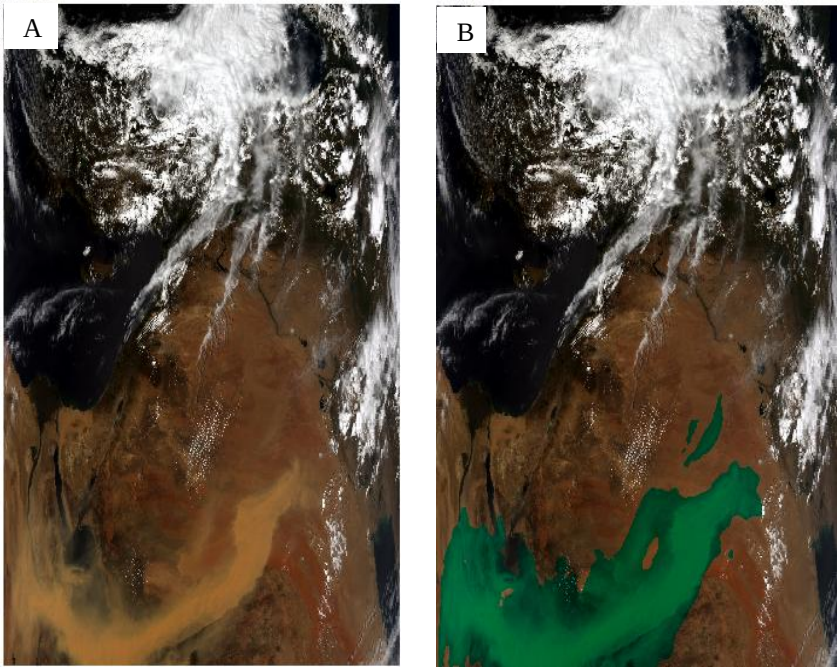

Figure 4-9 (A) is the true colour image of dust storm over north of Saudi Arabia on 13th of May 2005 captured by Aqua and (B) is its corresponding dust storm detection.

- **Dust Storm Detection over Vegetation**

To evaluate the performance of this technique over vegetation covered surfaces it has been applied to dust storms which occurred in 2011 over the northeast of China. The results are gaven in Table 4.7 which shows the average and STD results of applying the FFNN over non-sandy land. These show that the FFNN is more effective than over desert for dust storm detection, because it is more effective at reducing the false detection of non-dust storm pixels. The overall accuracy shows the FFNN is more effective over sandy lands than over non-sandy or vegetation covered land.

Table 4-7 The average and the standard deviation of the forecasting measures of applying FFNN over non sandy land

	TPR	FPR	TNR	FNR	ACC	PPV	NPV	FDR
Average	0.853	0.103	0.897	0.147	0.899	0.349	0.990	0.651
STD	0.083	0.060	0.056	0.083	0.060	0.169	0.008	0.169

Figures 4.10 and 4.11 show another pair of examples applying FFNN over non-sandy land. Figure 4.10 (A) shows a heavy dust storm over north east China captured by the Terra satellite on November 11th 2010. Figure 4.11(A), shows a thick dust storm which blew over the north of Afghanistan on 5th of October 2011 captured by the Aqua satellite. Figures 4.10 (B) and 4.11 (B) show the corresponding results of the FFNN algorithm applied to the data shown in Figures 4.10(A) and 4.11(A) shows the corresponding result of the FFNN algorithm applied to the data shown in Figure 4.11(A). The results show that the technique can detect dust storms over non- sandy surfaces as well as sandy surfaces.

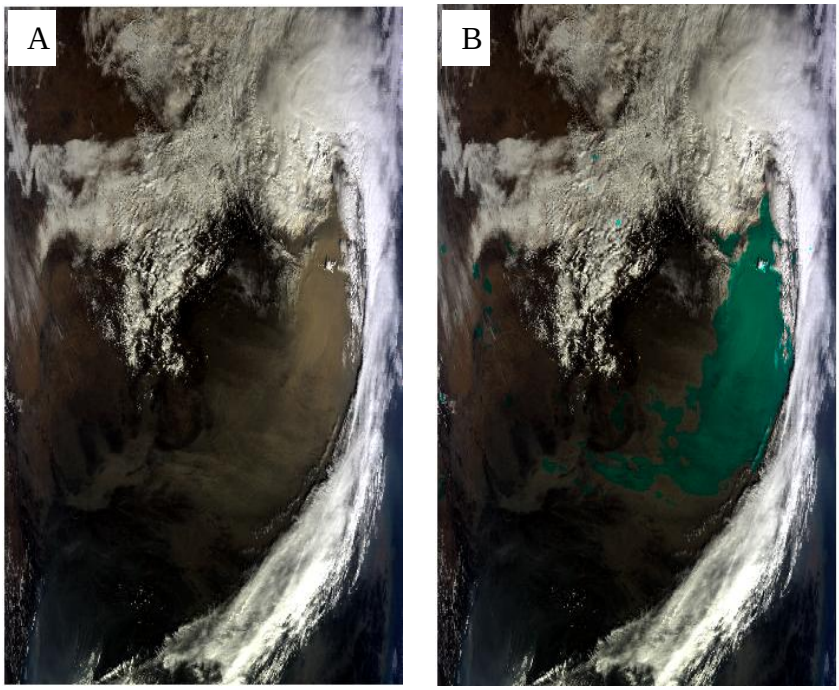

Figure 4-10 (A) is the true colour image of dust storm event over an area of vegetation (north east of China) captured by Terra Satellite on 11th of November 2010 and (B) is its corresponding dust storm detection.

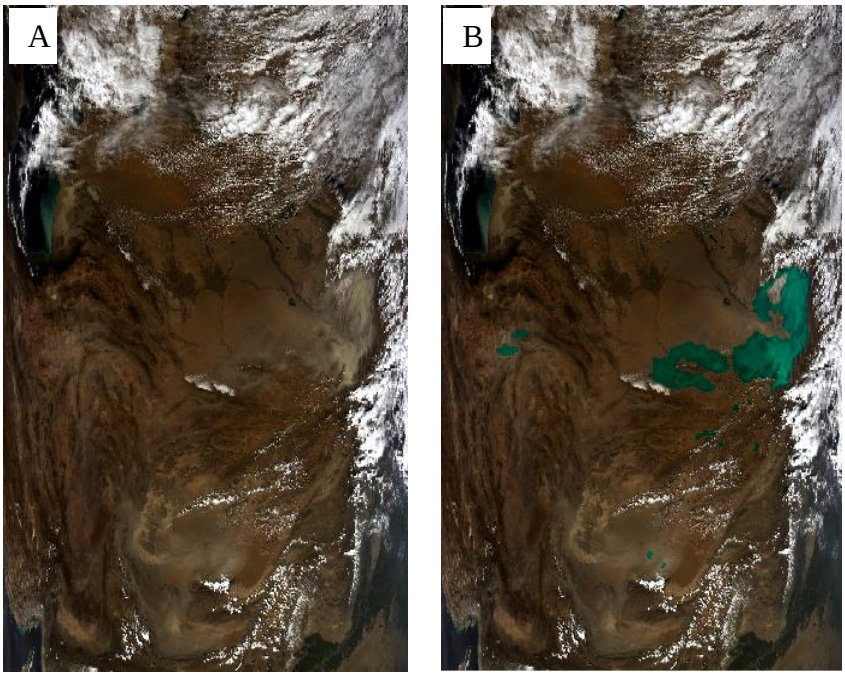

Figure 4-11 (A) is the true colour image of a dust storm event which occurred over Afghanistan on 5th of October 2011 captured by the Aqua Satellite and (B) is its corresponding dust storm detection.

- **Dust Storm Detection over Sea Water**

This FFNN algorithm was also applied to dust storms over sea water. Results are shown in Table 4.8 and illustrated in Figures 4.12 and 4.13. It was found that the algorithm can detect thick dust storms over water. However, some weak dust storm pixels are not detected. The results show the applying of FFNN over the sea is less effective than over land for detecting dust storms pixels, where a TPR value of about 72% was obtained. At the same time an FPR value of about 6% corresponded to cloud falsely detected as dust.

Table 4-8 The average and the standard deviation of the forecasting measures of applying FFNN over Sea water

	TPR	FPR	TNR	FNR	ACC	PPV	NPV	FDR
Average	0.717	0.063	0.937	0.283	0.913	0.599	0.963	0.401
STD	0.130	0.058	0.058	0.130	0.051	0.226	0.032	0.226

Figures 4.12(A) and 4.13(A) show the true colour images of dust storm events over Atlantic Ocean on and the 12th of February 2005 captured by the Aqua satellite. Figures 4.12(B) and 4.13(B) show the results of this technique applied to the data of figures 4.12(A) and 4.13(A), and it can clearly be seen that some of dust is not detected.

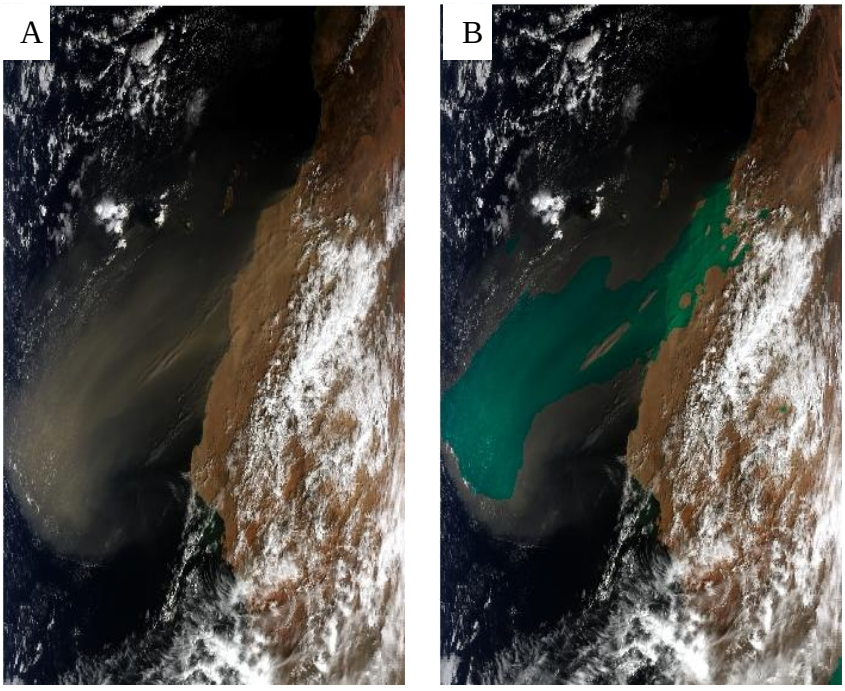

Figure 4-12 (A) is the true colour image of a Saharan dust storm captured by Aqua on 19th of July 2005 and (B) is its corresponding dust storm detection.

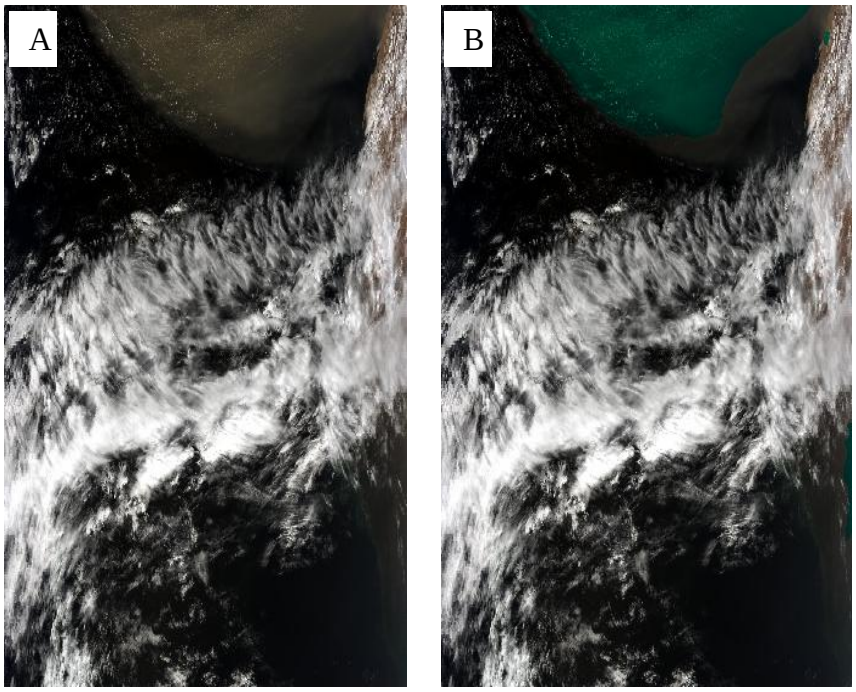

Figure 4-13(A) is the true colour image of a Saharan dust storm captured by Terra on 19th of July 2005 and (B) is its corresponding dust storm detection.

- **Dust Storm Detection at Night**

This FFNN algorithm was also applied to night time dust storms and the results are shown in Table 4.9. These show that applying FFNN at night is effective for dust storm detection with a TPR value of about 86%. However, it is less effective for reducing the false detection with an FPR value of about 10%. An overall accuracy of about 89% was achieved.

Table 4-9 The average and the standard deviation of the forecasting measures of applying FFNN over Sea water

	TPR	FPR	TNR	FNR	ACC	PPV	NPV	FDR
Average	0.858	0.107	0.893	0.142	0.893	0.409	0.986	0.591
STD	0.000	0.007	0.007	0.000	0.007	0.042	0.003	0.0429

Figures 4.14 (A) and 4.15 (A) are night-time false-colour images produced by the combination of bands 20, 31, and 32. Dust storms in figures 4.14 (A) and 4.15 (A) appear light purple in colour. Figure 4.14 (A) shows

the beginning of a dust storm over the south of Jordan in an image captured on 12th May 2005 at night by the Aqua satellite. Figure 4.15 (A) shows the continuing dust storm on 13th May 2005. The true colour image of this dust storm during the day is shown in Figure 4.9(A). Figures 4.14 (B) and 4.15 (B) show the results of this algorithm for the dust storms shown in figures 4.14 (A) and 4.15 (B) respectively. The detected dust storm is shown light blue in colour. This result shows that some of the weak dust storm over water has been missed.

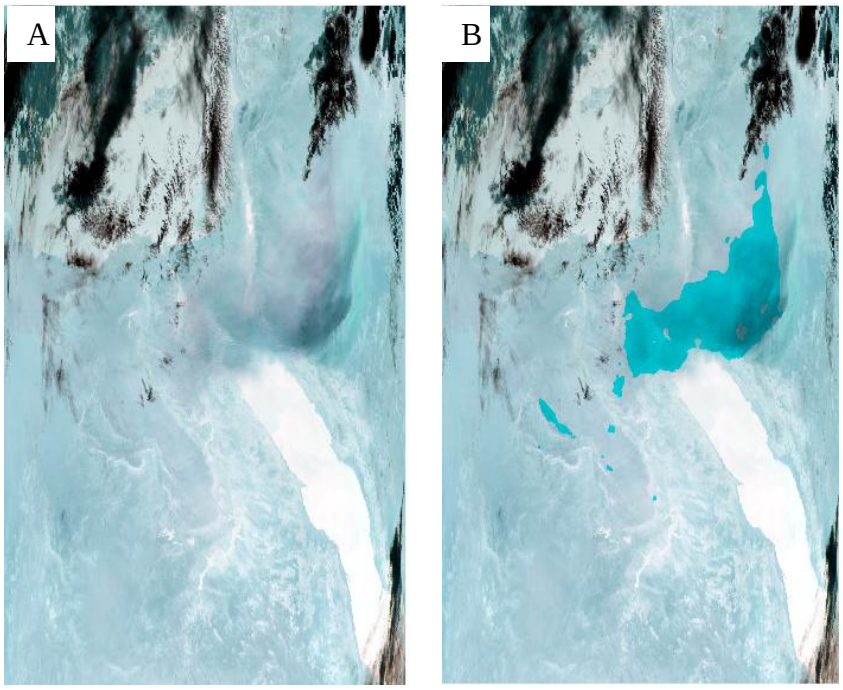

Figure 4-14 (A) is a false colour image of a dust storm captured by Aqua on 12th of May 2005 and (b) is its corresponding dust storm detection.

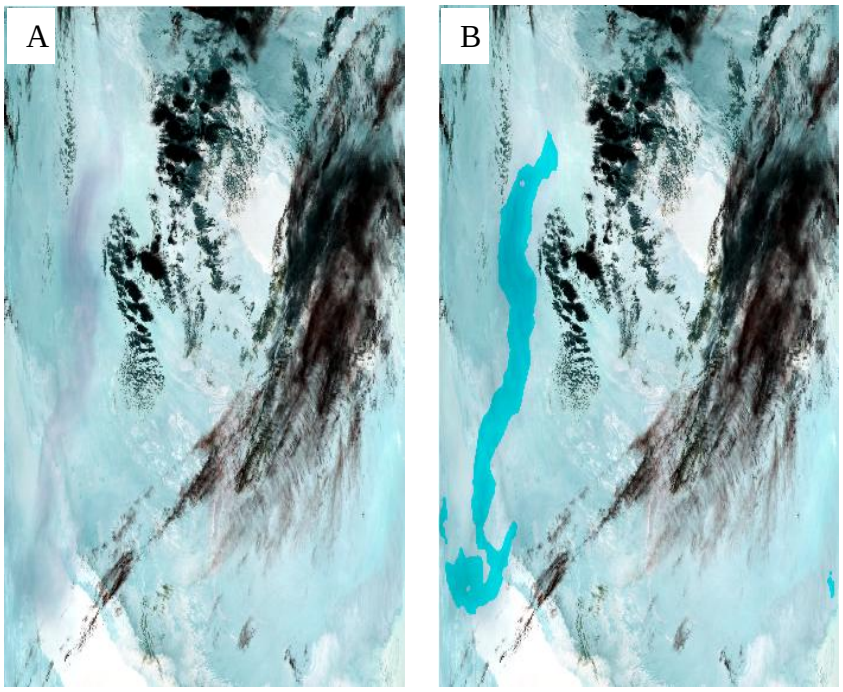

Figure 4-15 (A) is a false colour image of the dust storm over northern Saudi Arabia shown in Figure 36 (A) captured on 13th of May 2005 by Aqua Satellite and (b) is its corresponding dust storm detection

4.4. CREATING A DUST STORM MASK USING NEURAL NETWORKS

Zhang el al [30] developed a dust mask algorithm to identify dust storms from MODIS images over northern China on 7 April 2001. They used the brightness temperature differences BTD(31-32) and BTD(29-31) with a threshold technique to create five classes (strong dust region, weak dust region, ice cloud, low cloud or surface and uncertain region). This method was effective for the detection of dust storms divided into strong and weak regions. However, it is limited for the detection of dust storms over sandy regions. Mei et al [7] used the BTD(31-32) to monitor dust storms which occurred in April 2006 over northern China and to extract the scope of the dust storms. Also, the dust storms were intensity graded using multiple thresholds. The intensity of dust storm was divided into three categories (strong, medium and weak). This

method was effective for detecting, monitoring and estimating the intensity of dust storms over northern China. However, it has some limitations for detecting dust storms over water or sandy land.

The MODIS team used the cloud mask technique to define the pixels as: confident cloud, probably cloud, probably clear and confident clear [23].

In this section a feed-forward neural network method, together with a set of thresholds, is used to generate a dust storm mask. The dust storm mask is set to define image pixels as: certainly dust (Red), probably dust (Yellow), probably not dust (Aquamarine) or certainly not dust (Blue). The feature vector and the data used in this section are the same features and data used in Section 4.3. A set of thresholds (0.8, 0.65 and 0.5) are used to define the dust mask values where an FFNN output greater than 0.8 is certainly dust, an output greater than 0.65 and less than 0.8 is probably dust, an output greater than 0.5 and less than 0.65 is probably not dust, and an output less than 0.5 is certainly not dust.

Figures 4.16 to 4.19 show results from applying the dust storm mask algorithm: a red colour indicates pixels that defined as certainly dust storm, yellow indicates probably dust storm, light green indicates probably not dust storm, and blue indicates certainly not dust storm. This method is used in Chapter 6 to identify the images of dust storms.

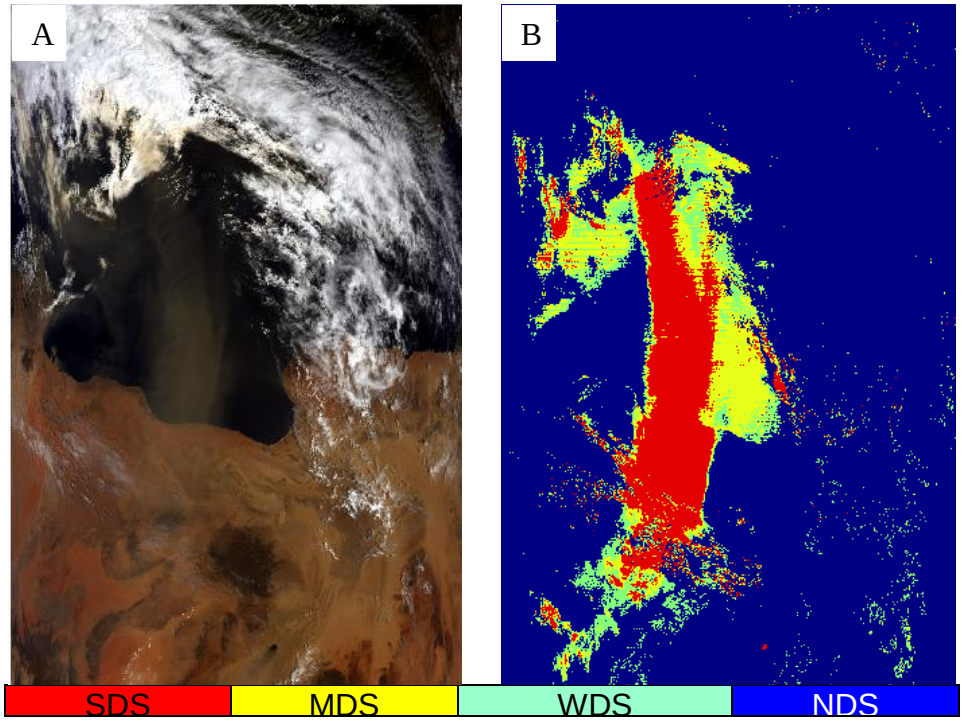

Figure 4-16 (A) is the true colour image of the Saharan dust storm captured by Terra on 8th of May 2002 and (B) is its corresponding dust storm mask.

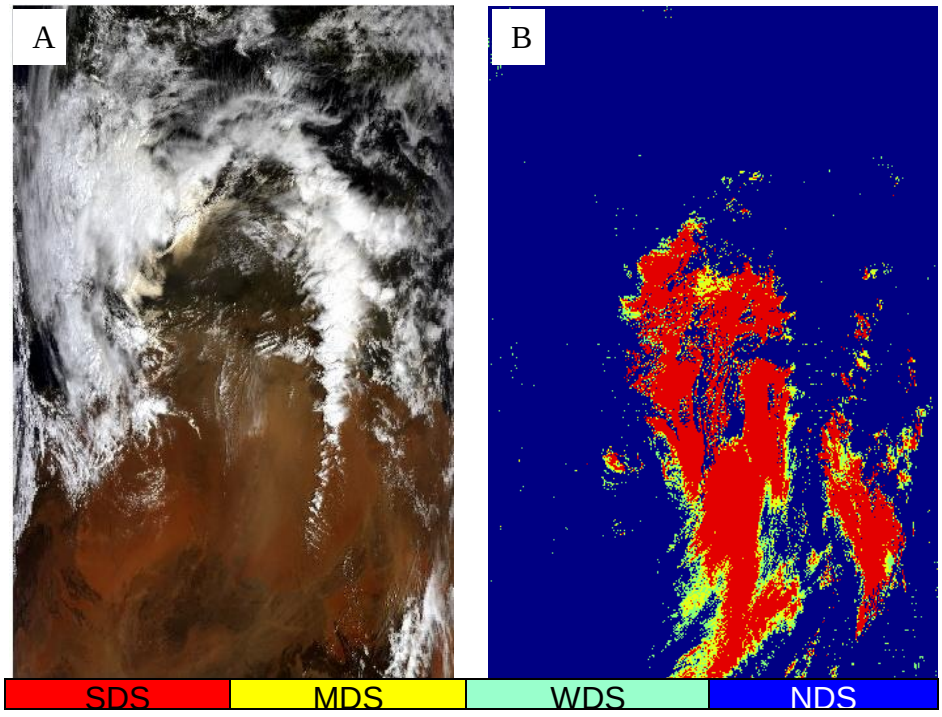

Figure 4-17 (A) is the true colour image of the Saharan dust storm captured by Terra on 8th of May 2002 and (B) is its corresponding dust storm mask.

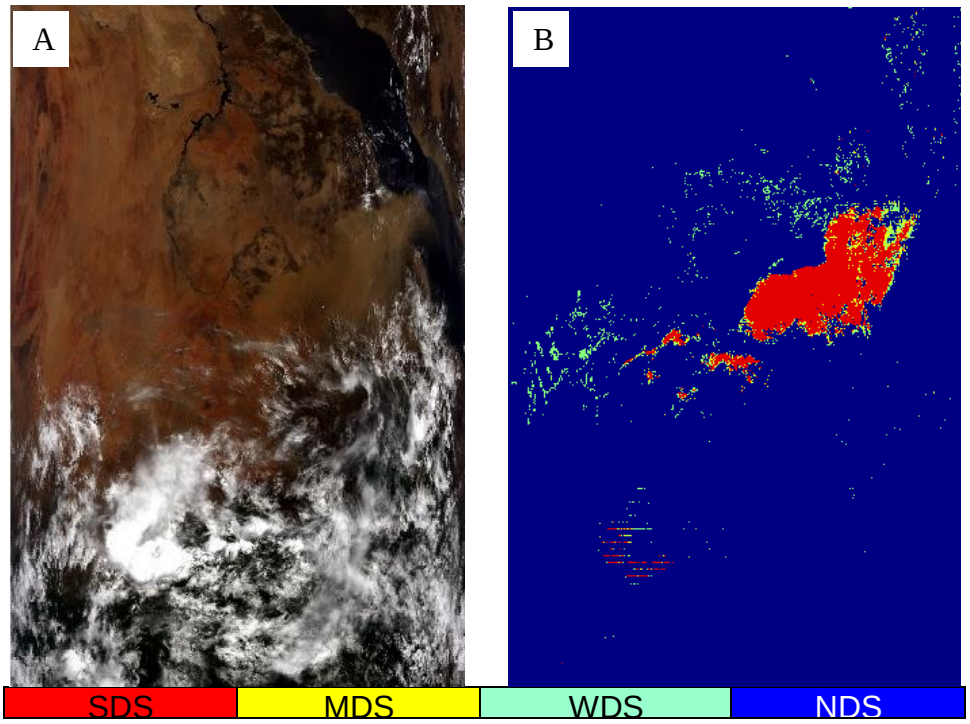

Figure 4-18 (A) is the true colour image of the Saharan dust storm captured by Terra on 8th of May 2002 and (B) is its corresponding dust storm mask.

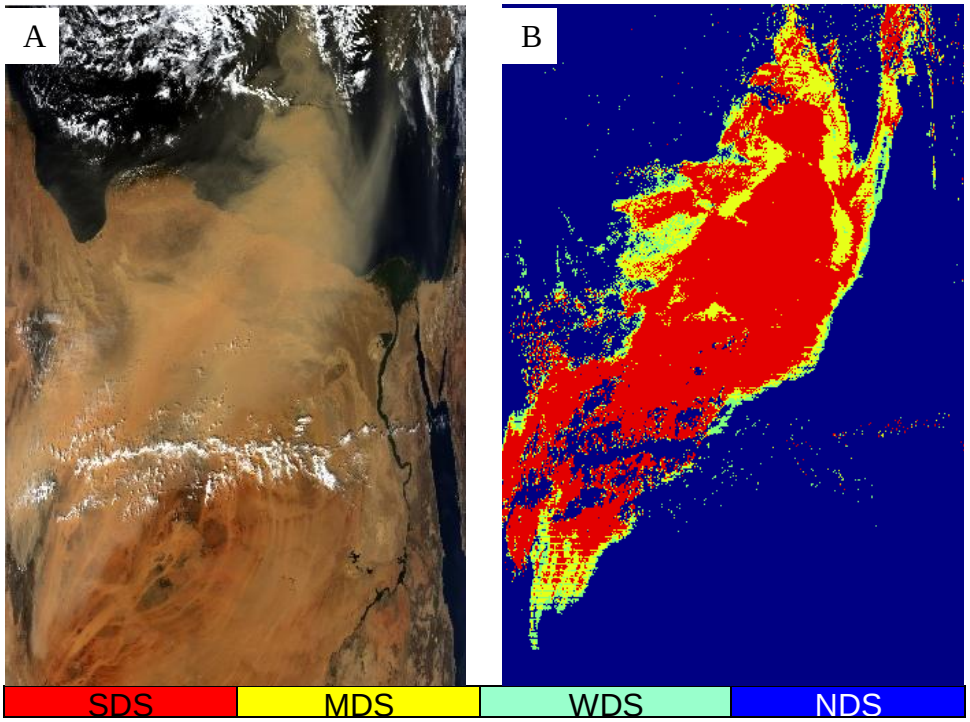

Figure 4-19 (A) is the true colour image of the Saharan dust storm captured by Terra on 25st of June 2006 and (B) is its corresponding dust storm mask

4.5. CHAPTER CONCLUSION

Dust storms were detected over different surfaces using a neural network classification method. The neural network method described in Section 4.2 was able to detect dust storms over different types of surfaces, using the two brightness temperature differences BTD(23-31) and BTD(31-32) and the three infrared bands b1, b3 and b4 as a feature vector. The results show that this neural network provides superior performance compared to the threshold methods, discussed in Chapter (3), for dust storm detection over different type of surfaces. However, the performance still needs improvement for detecting dust storms at night. For this reason, the neural network in Section 4.3 was developed to detect dust storms at night by using the brightness temperature differences BTD(20-31), BTD(23-31), BTD(29-31), and BTD(31-32) with the brightness temperature of band 31 as a feature vector. This method was effective for detecting dust storms over different type of surface and during the night time as well. The final work, described in Section 4.4, used the neural network with the features used in section 4.3 to generate a dust storm mask using a set of thresholds. This is to be used in Chapter 6 as part of an automated system to decide if an image contains dust storm or not, and to save information on dust storms images in a database. The next chapter, Chapter 5, presents a comparison between Artificial Feed Forward Back-Propagation Neural Network and Decision Tree for classifying MODIS image pixels into six class: cloud, dust storm, snow, water, land and vegetation.

CHAPTER FIVE

5. CLASSIFICATION OF MODIS IMAGES USING SIX CLASSES

5.1 INTRODUCTION

Image classification is an important part of remote sensing, image analysis and pattern recognition. In some cases, the classification may be just the first stage of image interpretation, while in others it may be the object of the analysis. For example, classification of land use from remotely sensed data produces a map-like image as the final product of the analysis [48]. The main reason for satellite image classification is the recognition of objects in the atmosphere and on the Earth's surface, and their display in the form of thematic maps [62]. Therefore, image classification is an important tool for examination of the satellite images [48]. Classification is more formally the process of assigning or mapping an input attribute set into its class label [63], as illustrated in Figure 5.1.

Figure 5-1 Classification as the task of mapping an input attribute set X into its class label Y.

Satellite image classification has been used in many studies to partition the images into semantically meaningful regions. However, manual classification needs much expensive human effort. Thus, automatic and efficient satellite image classification is one of the most important problems in remote sensing applications [64]. Many researchers have attempted to use the MODIS images in the classification of land cover using Normalised Difference Vegetation Index (NDVI) images [22], and many researchers have tried to detect one type of object from MODIS images using various techniques. The aim of this chapter is to classify MODIS images into the six classes: Cloud, Sand, Water, Land, Vegetation and Snow/Ice, and to compare decision tree and neural network approaches to find which is better for the task. The interest here in the decision tree stems partly from its use in the cloud mask, MODIS atmospheric product, which is generated using a decision tree classifier and data from 19 MODIS bands. However, the MODIS cloud mask takes a relatively long time to become available (about two hours) after the image is captured, and it also has difficulty separating cloud and thick dust storm, as well as separating weak dust storm and sandy land. Thus, with a new classifier, the classification of the six classes could be faster than before, as all the classes can be detected at one time as soon as the image data is made available. Also, a new classifier could be more effective at distinguishing between dust storm, snow and clouds, which are complicated objects.

The rest of this chapter is organised as follows. Section 5.2 provides a discussion and description of a decision tree to classify MODIS data. Section

5.3 describes using a feed forward neural network for multi-classifying MODIS data. Section 5.4 presents the conclusions from this chapter.

5.2 MODIS IMAGE CLASSIFICATION USING A DECISION TREE

Decision Trees are one of the most common classification algorithms used in machine learning to create a knowledge structure that guides the decision making process. There are two ways for creating a decision tree: 1) from a set of examples (data records), which is the most common technique and 2) from rules, which is thus called the rule-based decision tree method [65]. There are major differences between these two approaches. When creating a decision tree from rules, the method assigns attributes to the tree nodes using criteria based on the properties of the decision rules, rather than from the statistics of the data examples. A decision tree designed using data examples can only be an effective tool as long as no changes occur in the dataset used to generate the decision tree [65]. If there is a significant change in the data base of a decision tree then methods for restructuring the decision tree become desirable. However, it is known to be difficult to control or restructure decision trees [65]. A decision tree is a sort of multistage classifier, which can be implemented on one image or a set of images. It is made up of a collection of binary decisions that are used to decide the final category for each pixel. Each decision in the tree splits the data into one of two classes or sets of classes. As an example of a comparison with another classifier, a Maximum Likelihood Classifier (MLC) [52], to map very high resolution satellite images into 11 classes (Stone, House, Grassland, Grass dry area, Plain land, Sand, River, Submerged area, Sea water, trees and pool), the overall image classification

accuracies were found to be 86.66% and 81.33% for the Decision Tree and the MLC respectively. In another example, closer to the current interest, an automated method [9] used a decision tree classifier to classify data in the visible MODIS bands captured over the northwest of China into four classes: land, dust storms, cloud and snow. A weakness of this study is that the weak dust regions are not easily distinguished from the surface, and that is because the lower dust content in these regions does not cover the surface completely. Furthermore, cloud shadow and surface are mixed up with detected dust, so further improvement is still needed. The decision tree classification work presented in this chapter was done using a MATLAB tool designed to provide powerful and flexible decision trees.

5.2.1 FEATURE SELECTION

The most commonly methods used for detecting dust storms are the brightness temperature differences between bands 20, 23, 29, 31, and 32 which can identify dust storms from other objects in MODIS images. The brightness temperature difference between bands 31 and 32 has been used in many dust storm detection methods and for separating clouds from other surface contents [32], while the brightness temperature difference between bands 23 and 31 is used to separate dust storm and sandy surface using a threshold higher than 5,5K [61]. The Normalised Difference Vegetation Index (NDVI) is provided by the MODIS team to measure and monitor plant growth and vegetation cover using MODIS reflectance bands 1 and 2 [66] and can separate vegetation from other surfaces. It is defined in equation 5-1.

$$NDVI = \frac{band\ 2 - band\ 1}{band\ 2 + band\ 1} \qquad \text{Equation 5-1.}$$

The Normalized Difference Snow Index (NDSI) has been used to detect snow and Ice from MODIS images [67] and is defined in equation 5-2.

$$NDVI = \frac{band\ 4 - band\ 7}{band\ 4 + band\ 7} \qquad \text{Equation 5-2.}$$

The Normalized Difference Dust Index (NDDI) has been used to distinguish cloud from other objects in MODIS images [7] and is defined in equation 5-3.

$$NDDI = \frac{band\ 7 - band\ 3}{band\ 7 + band\ 3} \qquad \text{Equation 5-3.}$$

For these reasons the feature vector used in this section for training and testing a decision tree to classify MODIS images was chosen to be the BTDs between bands 23 and 31 and bands 31 and 32 and the NDDI, NDVI and NDSI.

5.2.2 EXPERIMENTAL AND VALIDATION

The process of training and testing the decision tree proceeded by first downloading 27 MODIS data sets from the Level 1 B and Atmosphere Archive and Distribution system website (LAADS Web), http://ladsweb.nascom.nasa.gov/. A total of 120,000 components of pixel data extracted from the MODIS data were used in this study, with 80% used for training and 20% for testing of the decision tree. An image showing the sampling of data for the six classes is shown in Figure 5.2. Figure 5.3 illustrates the methodology of extracting data from the images mentioned previously. Table 5.1 indicates the total number of data in each class in each feature used

in this study. Table 5.2 shows a sample of data used for training and testing the decision tree.

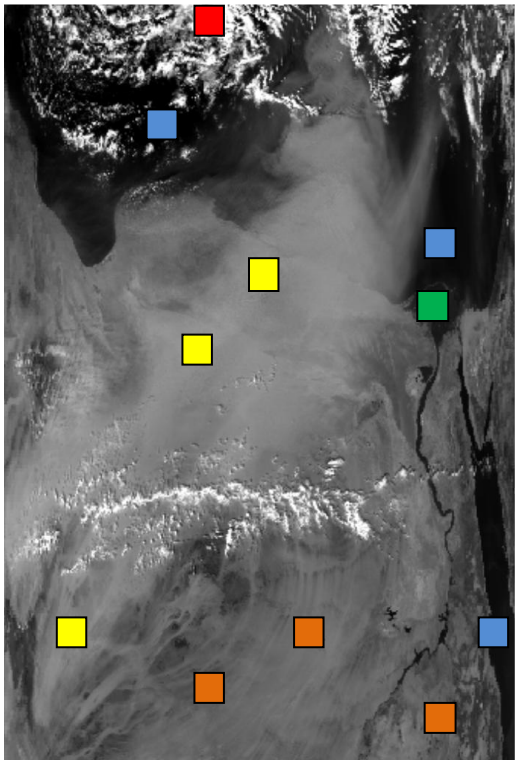

Figure 5-2 Example of pixel data extracted from a MODIS image: cloud is red, water is blue, dust storm is yellow, vegetation is green and land is brown.

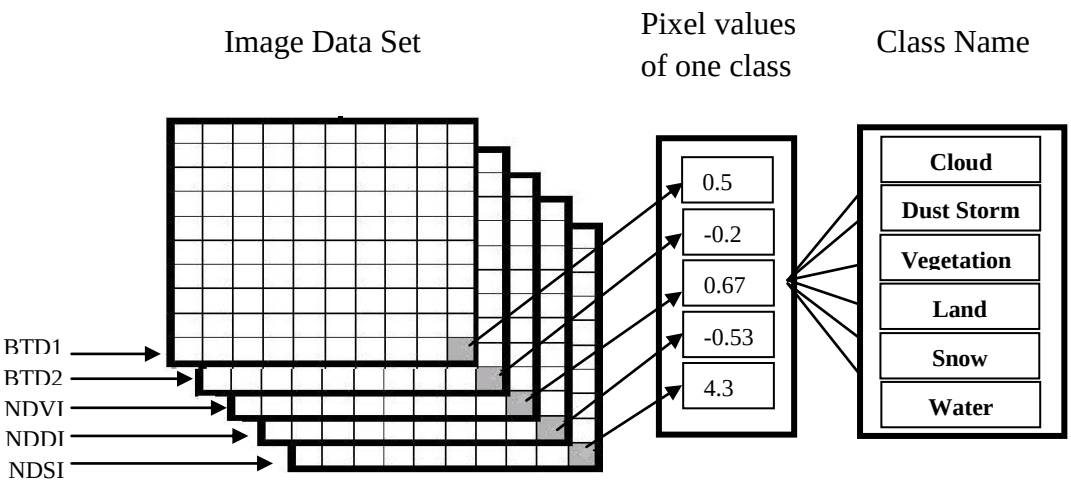

Figure 5-3 Steps in data extracted from the two BTDs, NDVI, NDDI and NDSI to be used in the decision tree

Table 5-1 Total number of data in each class in each feature

Class Description	Total Number of Samples in class per feature				
	BTD (23-31)	BTD (31-32)	NDVI	NDDI	NDSI
Cloud	25000	25000	25000	25000	25000
Dust Storm	25000	25000	25000	25000	25000
Water	20000	20000	20000	20000	20000
Vegetation	17500	17500	17500	17500	17500
Land	17500	17500	17500	17500	17500
Snow or Ice	15000	15000	15000	15000	15000

Table 5-2 Sample of data used for training the decision tree

Class ID value	Class Description	BTD (23-31)	BTD (31-32)	NDVI	NDDI	NDSI
100000	Cloud	5.9564	0.5357	0.0326	-0.6062	0.5783
010000	Dust Storm	1.9249	0.1153	-0.0199	-0.3117	0.2823
001000	Water	-0.5406	0.5727	-0.2151	-0.7860	0.6384
000100	Vegetation	2.0663	1.3890	0.7281	-0.1753	0.0983
000010	Land	3.2111	-1.4067	0.1484	0.6076	-0.4988
000001	Snow or Ice	0.1452	-0.1760	0.0816	-0.8660	0.8366

The performance of the decision tree was evaluated using the standard performance metrics: TPR, FPR, TNR, ACC, PPV, NPV and FDR. The decision tree was evaluated using two types of ground truth data. The first used 20% of the selected data as ground truth, and the second used the cloud mask as ground truth for cloud, water, vegetation, snow and land as well as manually detected dust storm. Figure 5.4 shows a flow chart of the decision tree training and testing procedures. Table 5.3 shows the average of results of repeated training and testing ten times, where the TPR, TNR, ACC, PPV and NPV are about 100% for all the classes, and the FPR and FDR are about zero for all the classes. This means that the decision tree is very effective at classifying this MODIS image data.

Table 5-3 Standard measure results for the six classes using training data with the decision tree

Class	TPR	FPR	TNR	ACC	PPV	NPV	FDR
Cloud	1	0	0.99	0.99	0.99	1	0
Dust	1	0	0.99	0.99	0.99	1	0
Land	1	0	1	1	1	1	0
Snow	1	0	1	1	1	1	0
Vegetation	1	0	1	1	1	1	0
Water	0.99	0	1	0.99	1	0.99	0

The decision tree was applied to MODIS data from the Terra and Aqua satellites acquired over several regions of the earth. The accuracy of this approach was assessed using the standard measures, with ground truth data provided by cloud mask, and manual detection of dust storms using true colour images.

After training, the decision tree was applied to 200 MODIS images with results shown in Table 5.4. These show, in particular, that the decision tree was unable to classify snow; the snow pixels were classified as water and also some dust storm and some cloud were classified as water. At the same time some water area was classified as cloud. Figures 5.5, 5.6, 5.7, 5.8 show some examples of MODIS images classified using the decision tree. The results show that the method is good for classifying dust storm, vegetation, land, water and cloud. However, it's not effective at classifying the snow.

Table 5-4 Standard measure results for the six classes using the decision tree with 200 new MODIS test data images

Class	TPR	FPR	TNR	ACC	PPV	NPV	FDR
Cloud	0.60	0.03	0.96	0.81	0.87	0.76	0.12
Dust	0.76	0.10	0.89	0.88	0.46	0.96	0.53
Land	0.67	0.10	0.89	0.85	0.65	0.90	0.34
Snow	0	0	1	0.95	NaN	1	NaN
Vegetation	0.70	0.06	0.93	0.91	0.38	0.97	0.61
Water	0.62	0.04	0.96	0.93	0.49	0.96	0.50

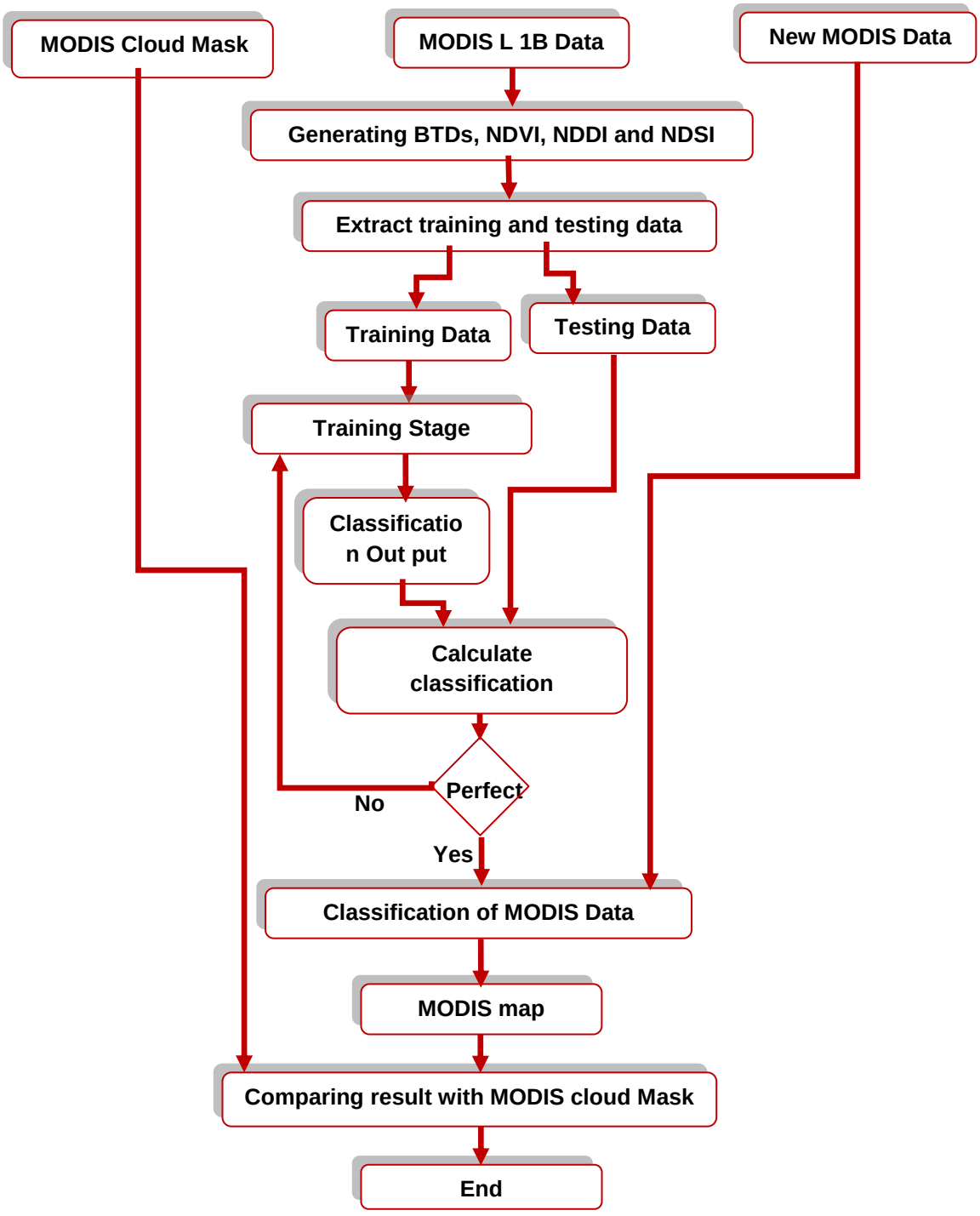

Figure 5-4 Flowchart of the Decision Tree application with separate training and testing data

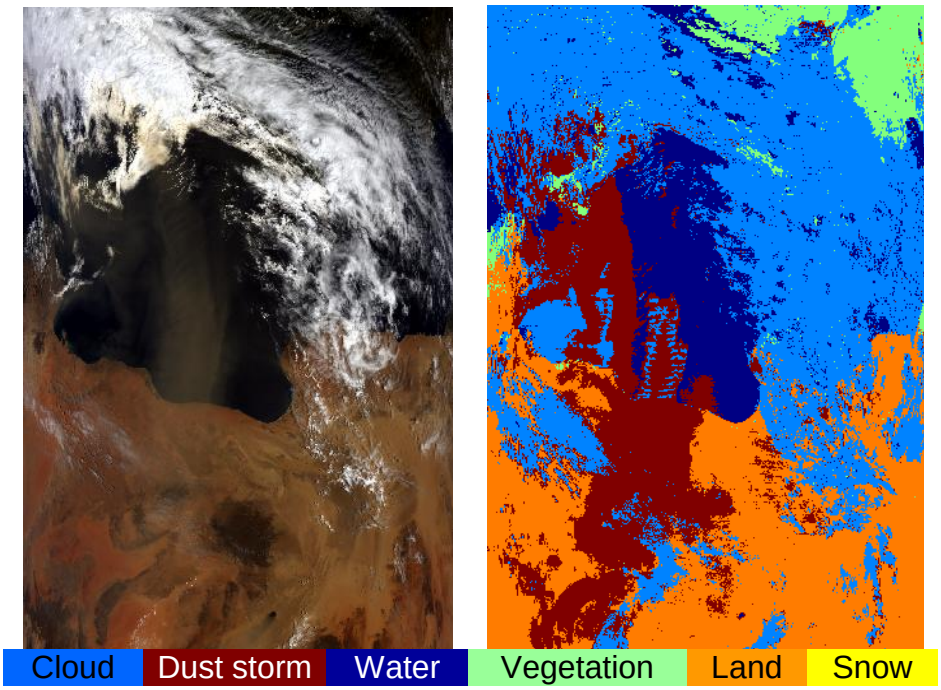

Figure 5-5 On the left is the true colour image of a dust storm captured over Libya by MODIS (Terra) on the 8th of May 2002 at 09:35 GMT, and on the right is the result of the decision tree classification displayed using the colour key at the bottom.

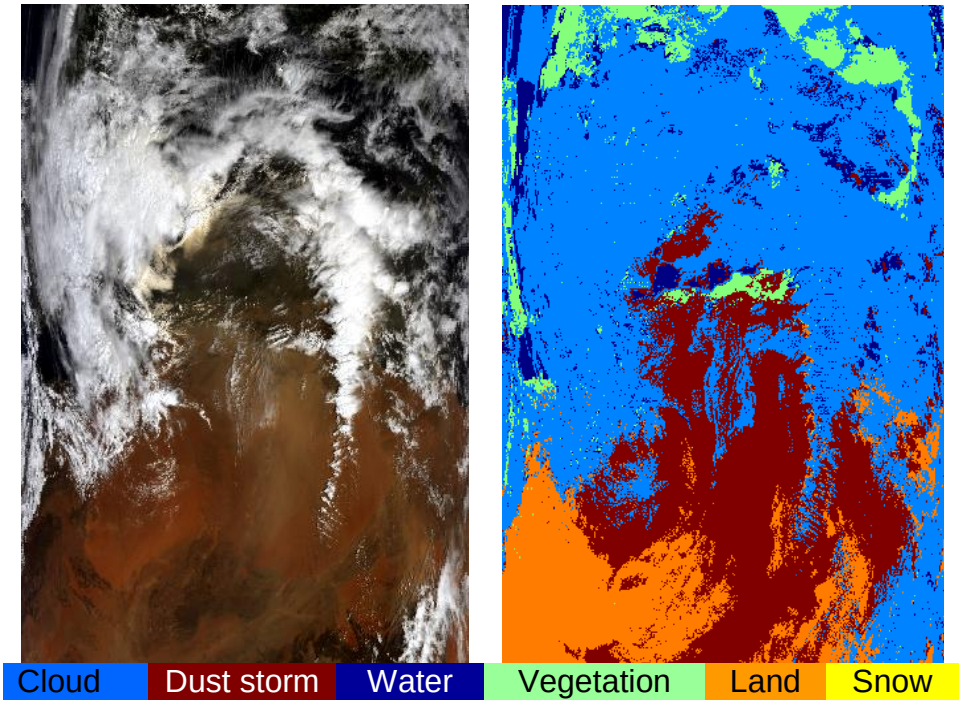

Figure 5-6 On the left is the true colour image of a dust storm captured over the Sahara by MODIS (Terra) on the 8th of May 2002, and on the right is the result of the decision tree classification displayed using the colour key at the bottom.

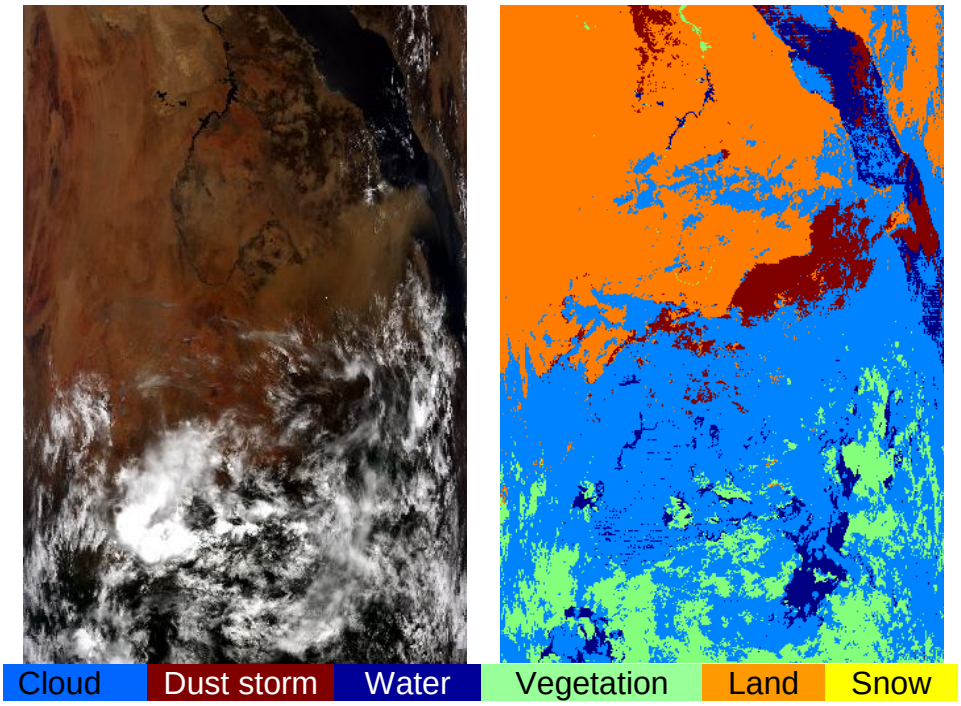

Figure 5-7 On the left is the true colour image of a dust storm captured over the Sahara by MODIS (Terra) on the 25th of June 2006, and on the right is the result of the decision tree classification displayed using the colour key at the bottom.

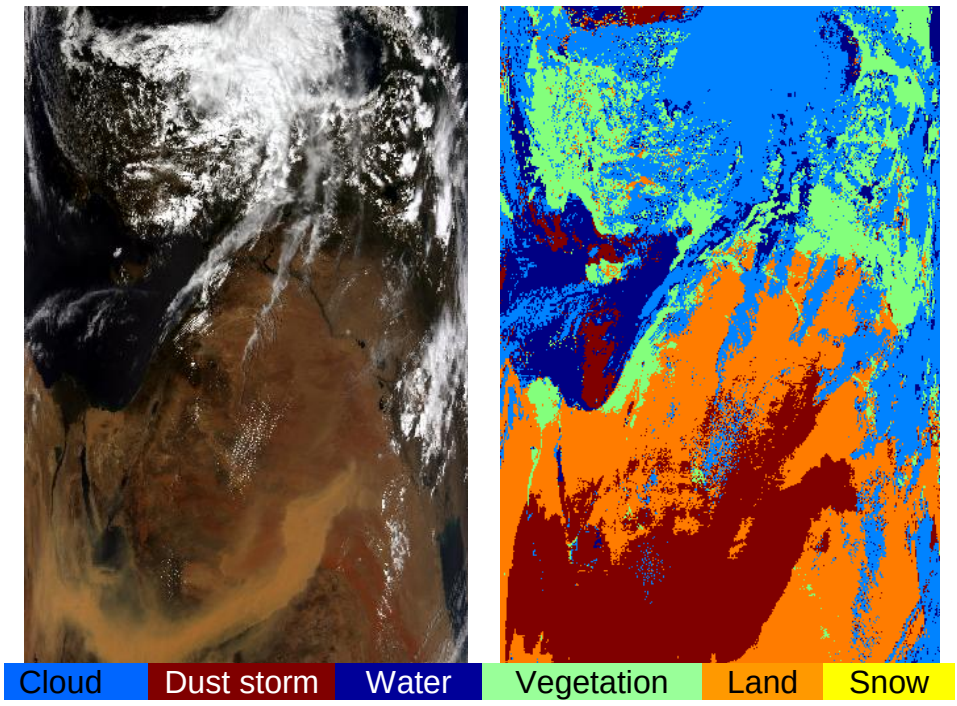

Figure 5-8 On the left is the true colour image of a dust storm captured over the north of Saudi Arabia by MODIS (Aqua) on the 13th of May 2005, and on the right is the result of the decision tree classification displayed using the colour key at the bottom.

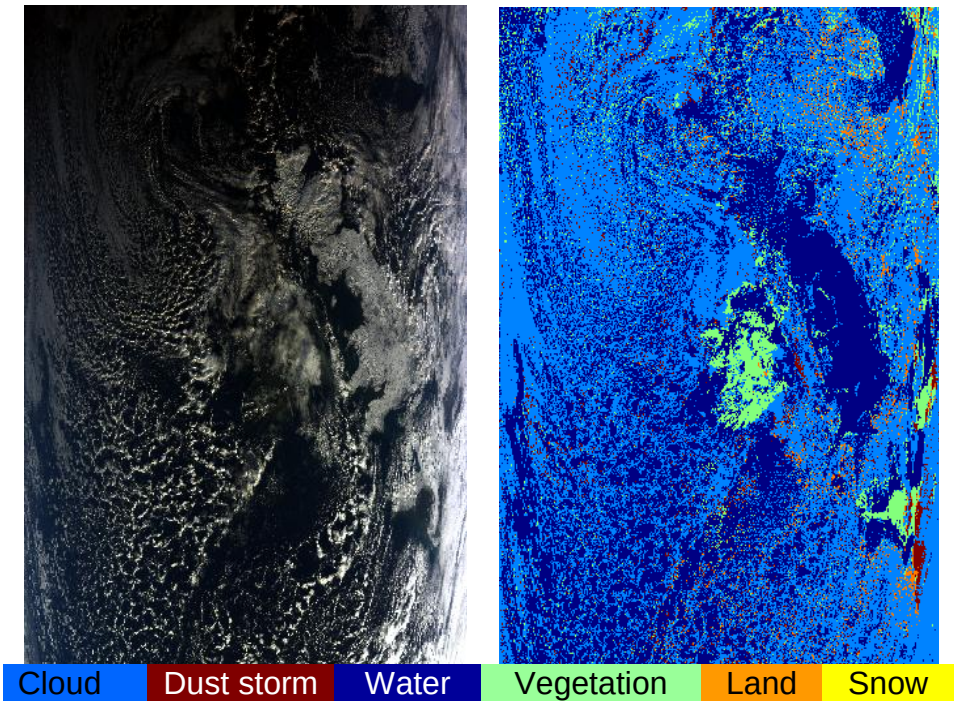

Figure 5-9 On the left is the true colour image of heavy snow captured over the UK by MODIS (Terra) on the 7th of January 2010, and on the right is the result of the decision tree classification displayed using the colour key at the bottom.

5.3 MODIS IMAGE CLASSIFICATION USING A NEURAL NETWORK

Multi-class pattern recognition is the problem of mapping an input feature into more than two pattern classes. Multi-class pattern recognition has a wide range of applications such as handwriting recognition, object classification, speech tagging and recognition, bioinformatics, text categorization and information retrieval [68]. Object classification is one of the most active research and application areas for neural networks. In this section a neural network is used to classify the pixels of MODIS images into the same six classes as the decision tree: Cloud, Dust Storm, Land, Vegetation, Water and Snow, as in Section 5.2.

5.3.2 FEATURE SELECTION

The feature vector used in this section for training and testing the neural network to classify MODIS image is the same as the feature vector used in the decision tree of Section 5.2: BTD(23-31), BTD(31-32), NDDI, NDVI and NDSI. Also, the same date used for training and testing the decision tree is used for training and testing the neural network. As before, these data were divided randomly into sets of 80% and 20% for training and testing respectively.

5.3.2 EXPERIMENTAL RESULTS AND DISCUSSION

The performance of the neural network was evaluated using the standard performance metrics: TPR, FPR, TNR, ACC, PPV, NPV and FDR. The neural network was evaluated using two types of ground truth, the first used 20% of the selected data as ground truth and the second used the cloud mask as ground truth for cloud, water, vegetation, snow and land as well as manually detected dust storm. Table 5.5 shows the average standard measures obtained for the six classes during the training and testing of the neural network ten times. Where the TPR, TNR, ACC, PPV and NPV are about 100% for all the classes and the FPR and FDR are about zero for all the classes. This shows that the neural network is very effective at classifying MODIS images.

Table 5-5 Standard measure results for the six classes using training data with the neural network

Class	TPR	FPR	TNR	ACC	PPV	NPV	FDR
Cloud	1	0	1	1	1	1	0
Dust	1	0	1	1	1	1	0
Land	1	0	1	1	1	1	0
Snow	1	0	1	1	1	1	0
Vegetation	1	0	1	1	1	1	0
Water	1	0	1	1	1	1	0

After the neural network was trained it was applied to the same 200 MODIS data sets acquired by the Terra and Aqua satellites over different region of the earth and used for testing the decision tree.

A comparison of the decision tree and neural network results shows that the latter is much better than the former for classifying MODIS data, in particular for classifying snow pixels. Table 5.6 shows the average results from the neural network and figures 5.10, 5.11, 5.12, 5.13 and 5.14 show some examples of classifying MODIS images using the neural network. Comparing Table 5.6 with Table 5.4 shows that the NN method is better than the decision tree for classifying dust storm, vegetation, land, water, cloud and snow since the TPR, TNR, ACC, PPV and NPV values are higher than from the decision tree. Also, the FPR and the FDR values are less than from the decision tree.

Table 5-6 Standard measure results for the six classes using the neural network with 200 new MODIS test data images

Class	TPR	FPR	TNR	ACC	PPV	NPV	FDR
Cloud	0.77	0.06	0.85	0.93	0.90	0.79	0.09
Dust	0.82	0.06	0.92	0.93	0.58	0.96	0.41
Land	0.91	0.15	0.87	0.84	0.66	0.96	0.33
Snow	0.79	0.03	0.96	0.96	0.47	0.99	0.52
Vegetation	0.76	0.06	0.91	0.93	0.69	0.94	0.30
Water	0.85	0.03	0.95	0.96	0.768	0.97	0.23

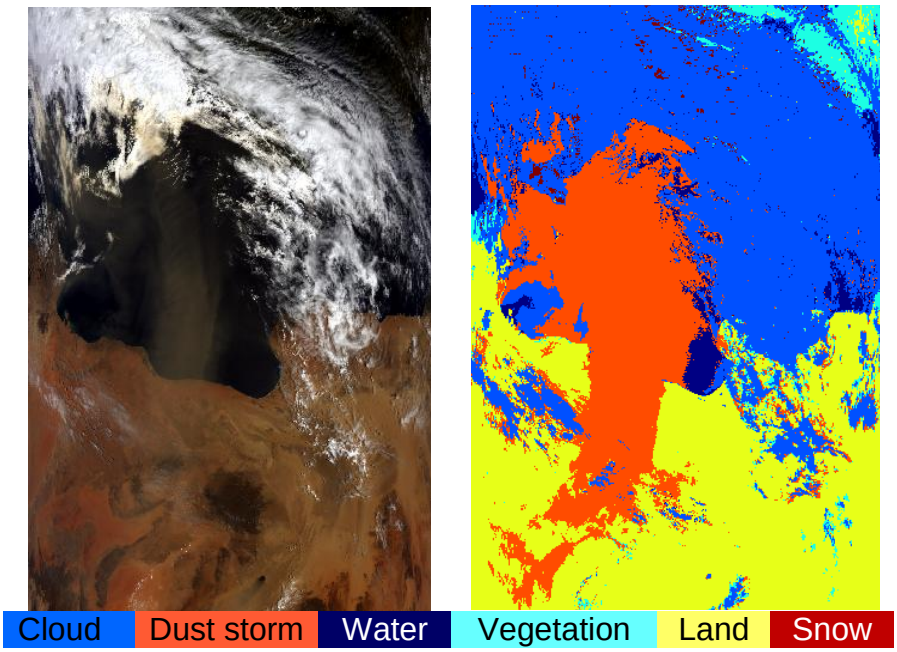

Figure 5-10 On the left is the true colour image of a dust storm captured over Libya by MODIS (Terra) on the 8th of May 2002 at 09:35 GMT, and on the right is the result of the neural network classification displayed using the colour key at the bottom

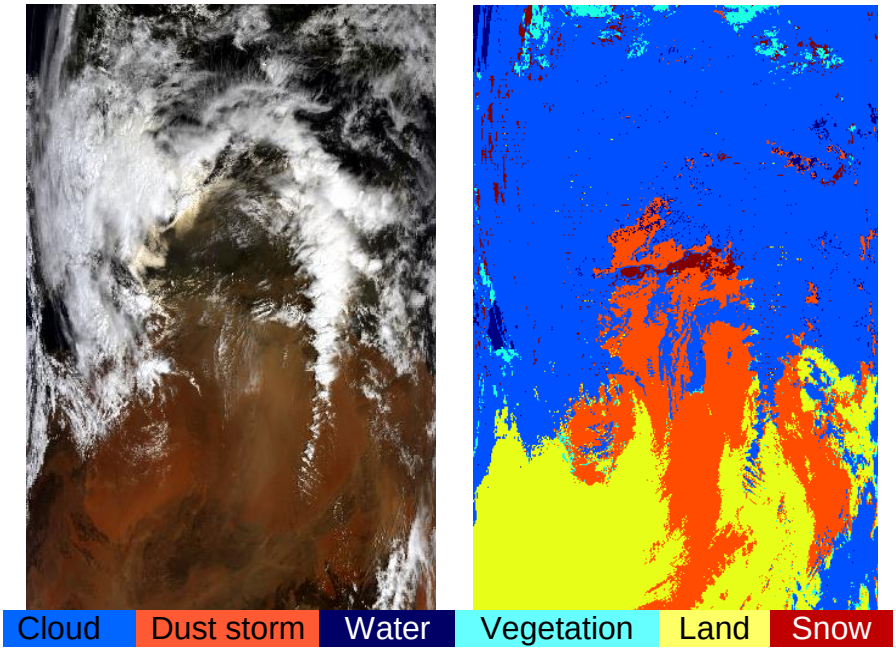

Figure 5-11 On the left is the true colour image of a dust storm captured over the Sahara by MODIS (Terra) on the 8th of May 2002, and on the right is the result of the neural network classification displayed using the colour key at the bottom.

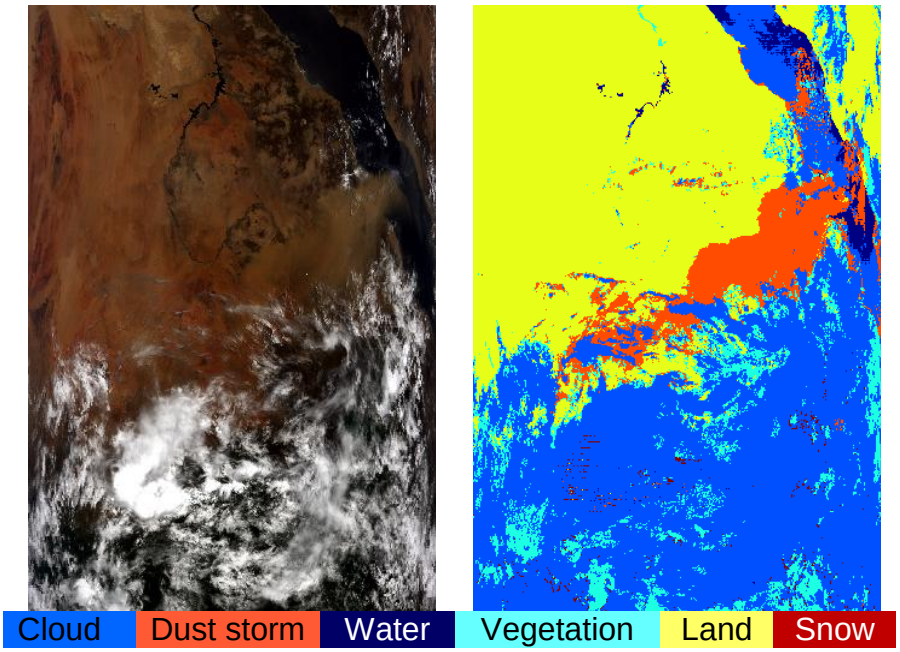

Figure 5-12 On the left is the true colour image of a dust storm captured over the Sahara by MODIS (Terra) on the 25th of June 2006, and on the right is the result of the neural network classification displayed using the colour key at the bottom.

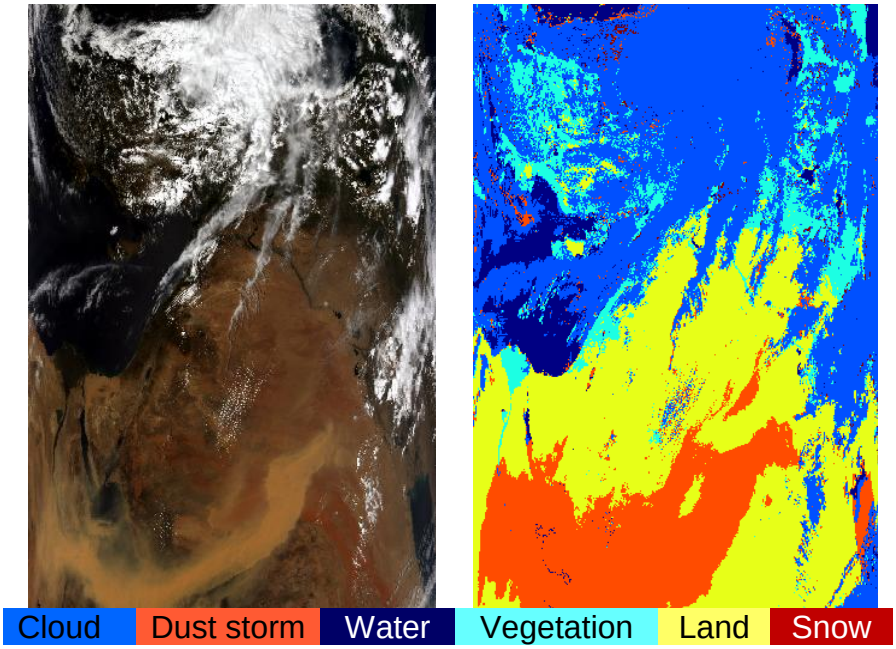

Figure 5-13 On the left is the true colour image of a dust storm captured over the north of Saudi Arabia by MODIS (Aqua) on the 13th of May 2005, and on the right is the result of the neural network classification displayed using the colour key at the bottom.

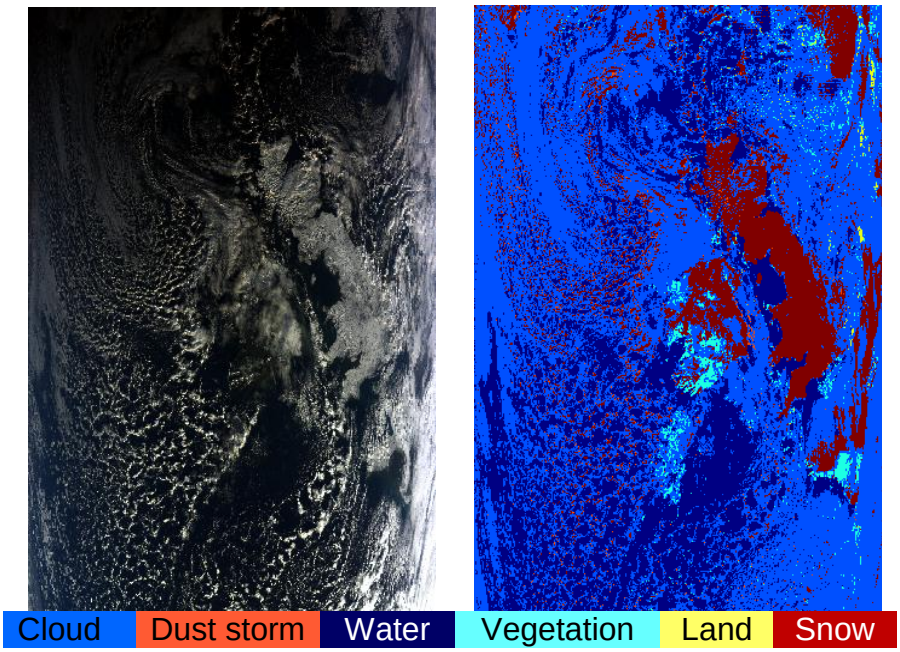

Figure 5-14 On the left is the true colour image of heavy snow captured over the UK by MODIS (Terra) on the 7th of January 2010, and on the right is the result of the neural network classification displayed using the colour key at the bottom.

5.4 CHAPTER CONCLUSION

In this chapter, a comparison was made between the use of a decision tree and an FFNN to classify MODIS images into the six classes: cloud, dust storm, water, vegetation, land and snow. The features used in both methods are: BTDs from bands 23 and 31, and bands 31 and 32 and NDDI, NDVI and NDSI. During training, both methods gave essentially the same performance but when new data was used, the neural network was found to be more effective than the decision tree. Furthermore, both methods are much faster than waiting for the cloud mask results to become available. The neural network and decision tree are better than the cloud mask method for dust storm detection. A limitation of both decision tree and neural network methods is that they can only be used during the day.

CHAPTER SIX

6. GENERATING AN AUTOMATED MODIS DUST STORM DATABASE SYSTEM

6.1 INTRODUCTION

As previously discussed, dust storms are a natural hazard whose increased frequency in recent years has significantly affected human life. Focussed research is required in order to more effectively monitor and track these dust storms. A critical element necessary for this to happen is a comprehensive database of dust storm types. This chapter therefore presents the author's system for automatically generating a dust storm database from MODIS data. The technique for the detection of dust storms during both day and night, as presented in Chapter 4, is implemented here. The system is interfaced using MATLAB in order to create a complete platform package which includes two predominant interfaces: the administrator interface and the user interface. This chapter is organized as follows: Section 6.2 presents the objectives of the system, Section 6.3 presents the system development, Section 6.4 presents the validation of the system and Section 6.5 presents the conclusions of the chapter.

6.2 SYSTEM OBJECTIVE

The primary aim of this system is the creation of a dust storm database. This database will consist of the metadata of dust storm events which will assist

researchers using MODIS data to detect dust storm events more easily. Furthermore, this system will also form the primary step in creating a MODIS hazards database system.

6.3 SYSTEM DEVELOPMENT

The MODIS dust storm database system consists of two packages: the administrator package and the user package. The administrator package enables the administrator to upload new MODIS files. These files are automatically checked for the presence of a dust storm, and if a storm is detected, information is extracted from the file and saved in the database. This information includes: date, time, density and file name. The administrator can then search the database for information regarding previous dust storm events. The density *D* indicates the size of the dust storm in terms of a percentage of the size of the image and is calculated using equation 6-1.

$$D = (M/V) * 100 \qquad \text{Equation 6-1.}$$

where *M* is the number of detected dust storm pixels and *V* is the total number of pixels in the image.

The user version of the package enables the user to search and display dust storm information that has been saved by the administrator. This system was developed using MATLAB, with the administrator package being developed first. The method used in this section for dust storm detection is the same method used in Chapter 4 where four BTDs were used for the detection of dust

storms. The administrator package includes two main classes of process as shown in Figure 6.1.

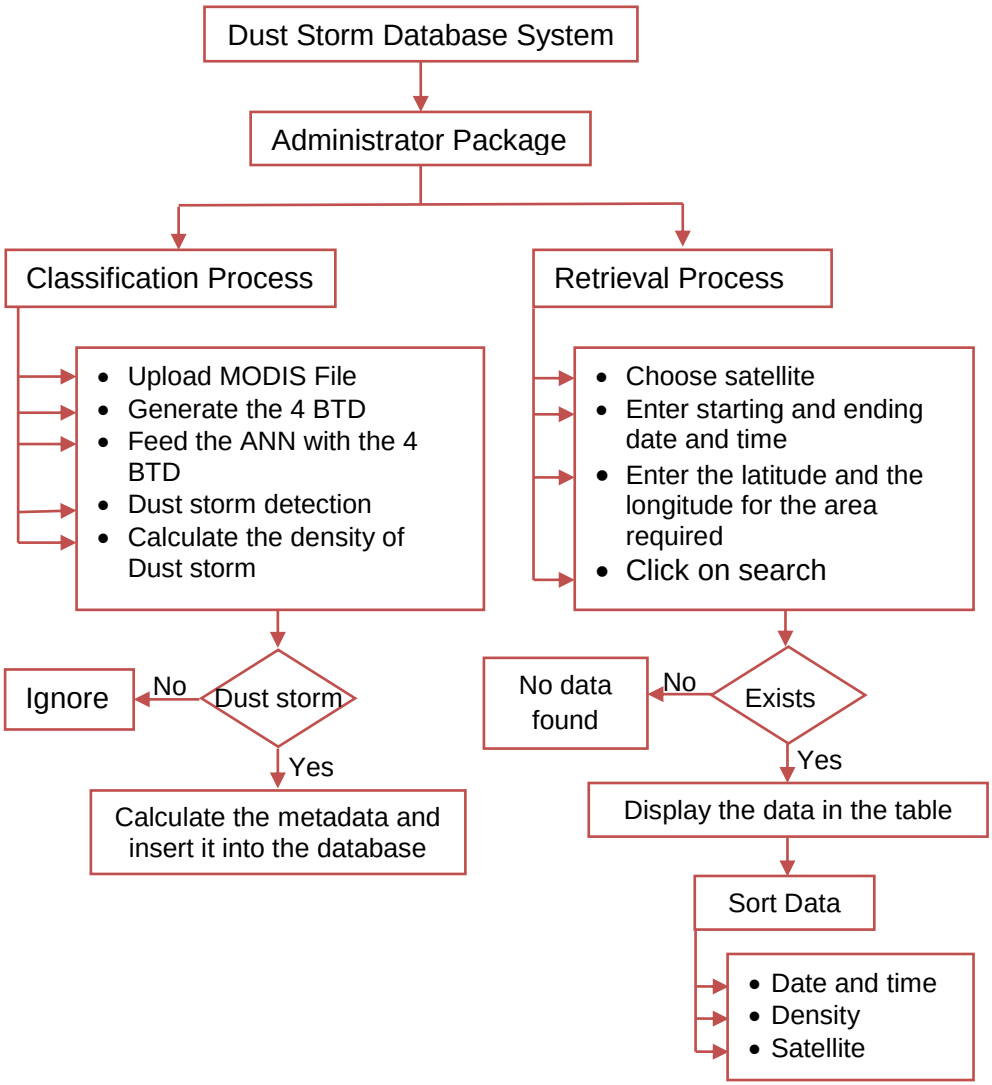

Figure 6-1 Block diagram describing the operations of the administrator package for MODIS dust storms database

In contrast, the user package includes only one main class of process as shown in Figure 6.2.

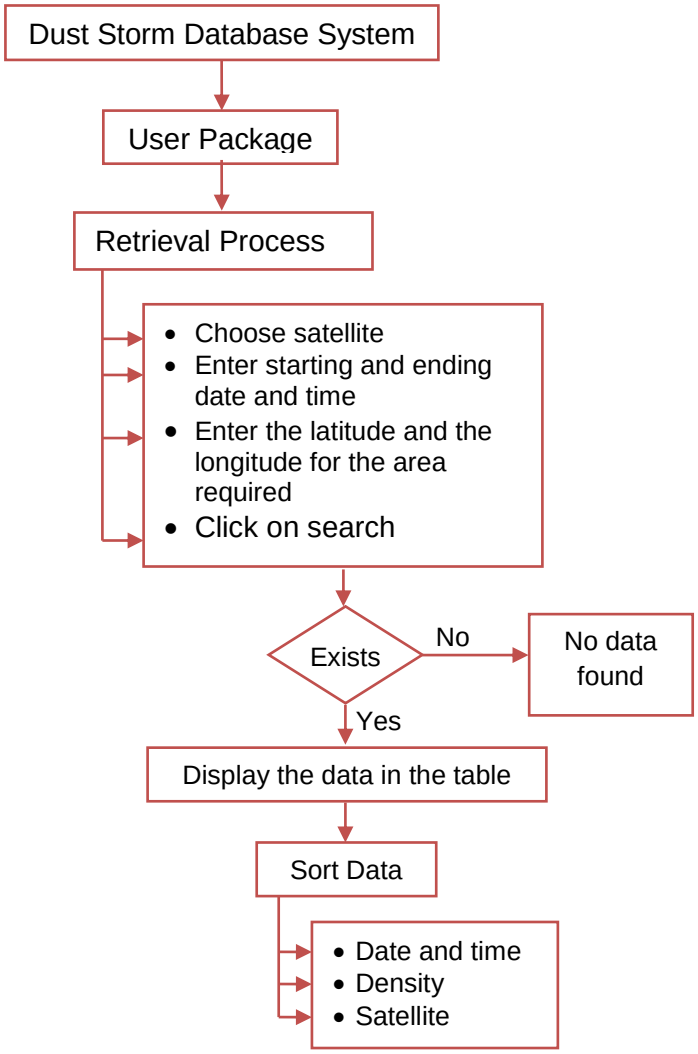

Figure 6-2 Block diagram describing the operations of the user package for MODIS dust storms database

6.4 SYSTEM VALIDATION

This section presents a step by step validation of the MODIS dust storm database system for both the administrator and user packages.

6.4.1. ADMINISTRATOR PACKAGE

When the administrator package is run, the administrator interface appears as shown in Figure 6.3.

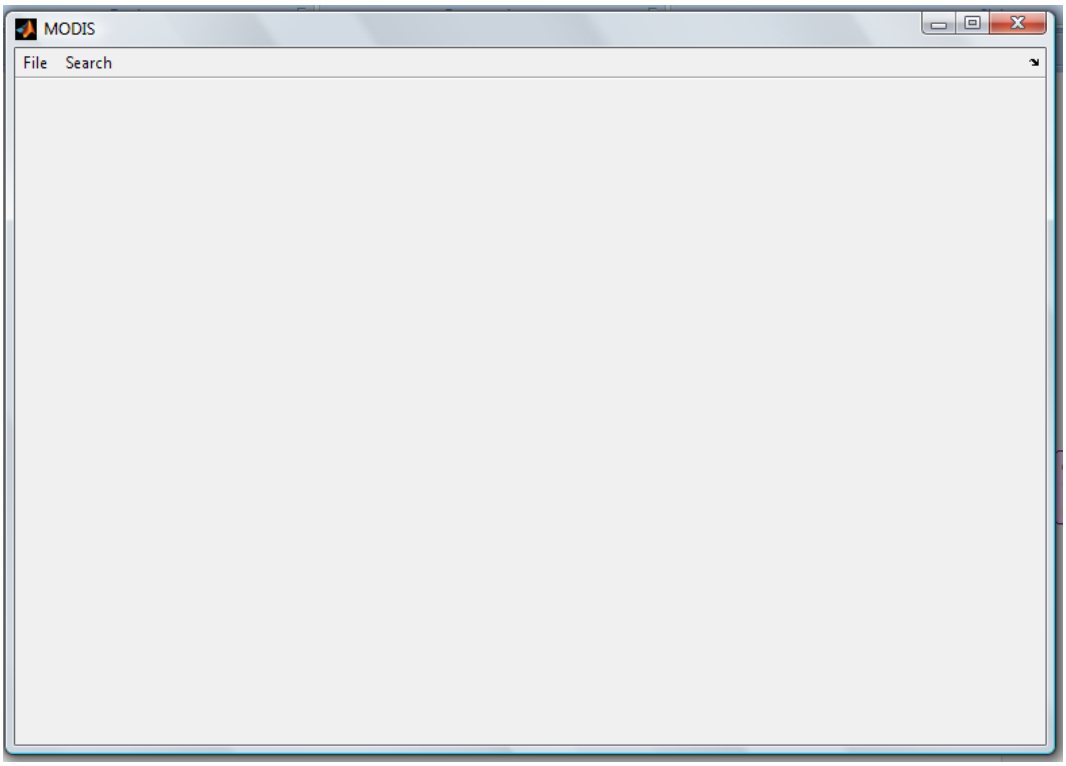

Figure 6-3 The main interface of the administrator package

The menu bar of the main interface of the administrator package includes a File menu and a Search menu. The File menu includes three Items:

- **Load File**: from the load file menu item the administrator can load new MODIS file data to be automatically checked for the presence of dust storms.
- **Clear window**: the clear window menu item allows the administrator to clear the interface of any items.
- **Exit**: the exit menu item allows the administrator to exit and close the system.

When the administrator clicks on the file menu the items menu appears as shown in Figure 6.4.

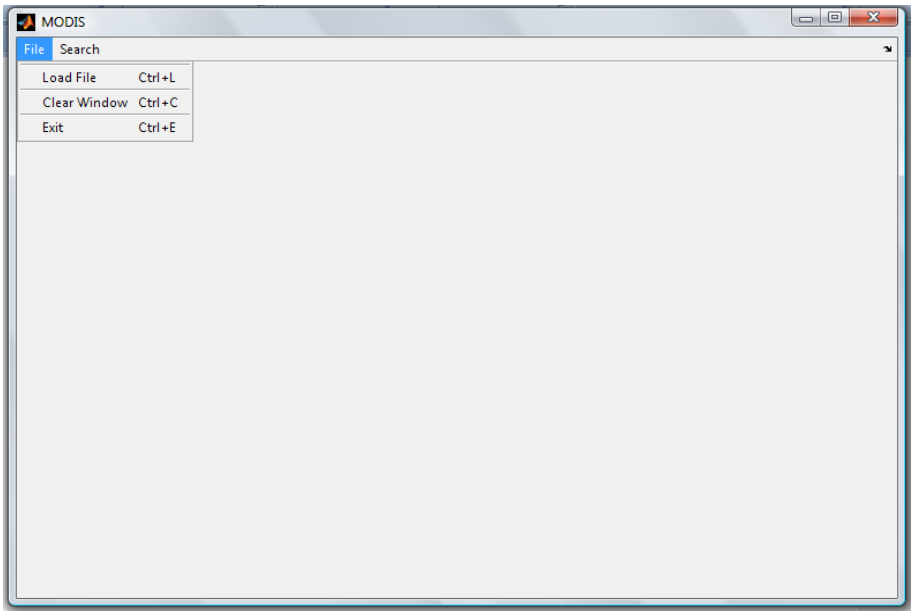

Figure 6-4 The file menu of the administrator package interface

If the administrator clicks on the load file menu item, or uses the shortcut key combination Ctrl + L, a new window will appear allowing the administrator to load a MODIS Level 1B of type hdf as shown in Figure 6.5. If the loaded file is not MODIS Level 1B, an error message will appear as shown in Figure 6.6.

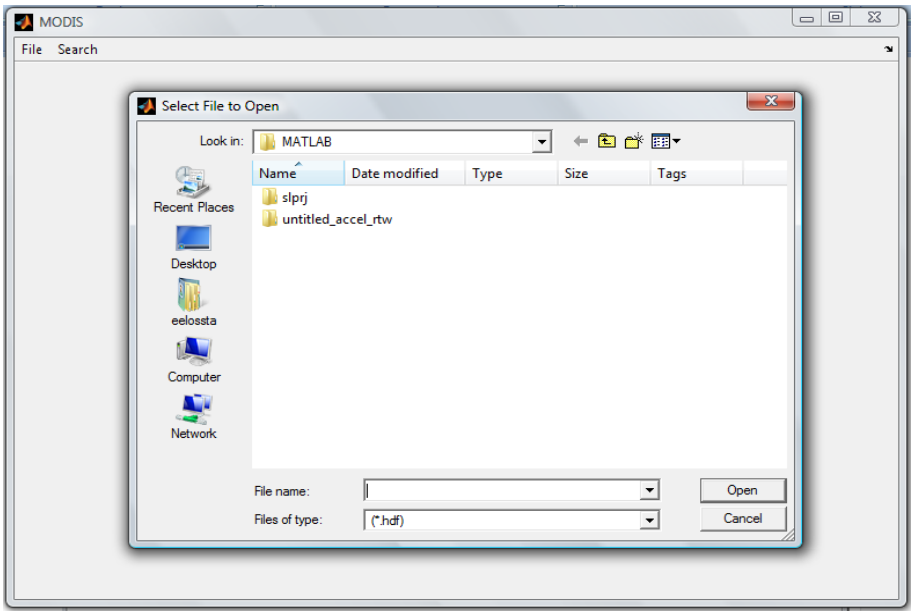

Figure 6-5 Loading MODIS Level 1B data

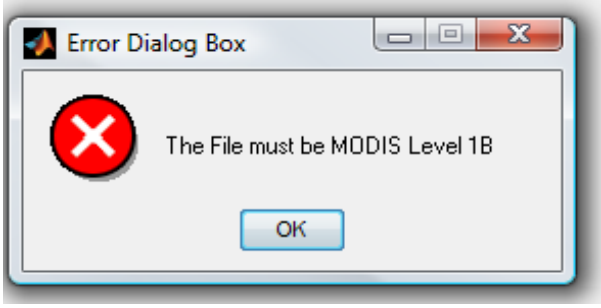

Figure 6-6 Error message caused by loading the wrong file

If the administrator has loaded the correct file, the system will automatically generate the BT data for bands 20, 23, 29, 31 and 32, and will then create the four BTDs. Upon completion, the system will feed these data into the trained neural network. If the neural network outputs a result larger than 0.7, this will be classified as dust storm data, and the density of the dust storm will then be calculated; if the density is higher than 0.24, then the associated image will be classified as a dusty image and the metadata will be saved in the database. The image will also be displayed on the main interface of the system as shown in the Figure 6.7, while a message will appear to confirm the addition of the metadata to the database. However, if the image is not classified as a dusty image, it will appear on the main interface with a message as shown in Figure 6.8. Furthermore, if the image is classified as a dusty image and the metadata of this file already exists in the database, the image will appear with the message “this record already exists” as shown in Figure 6.9.

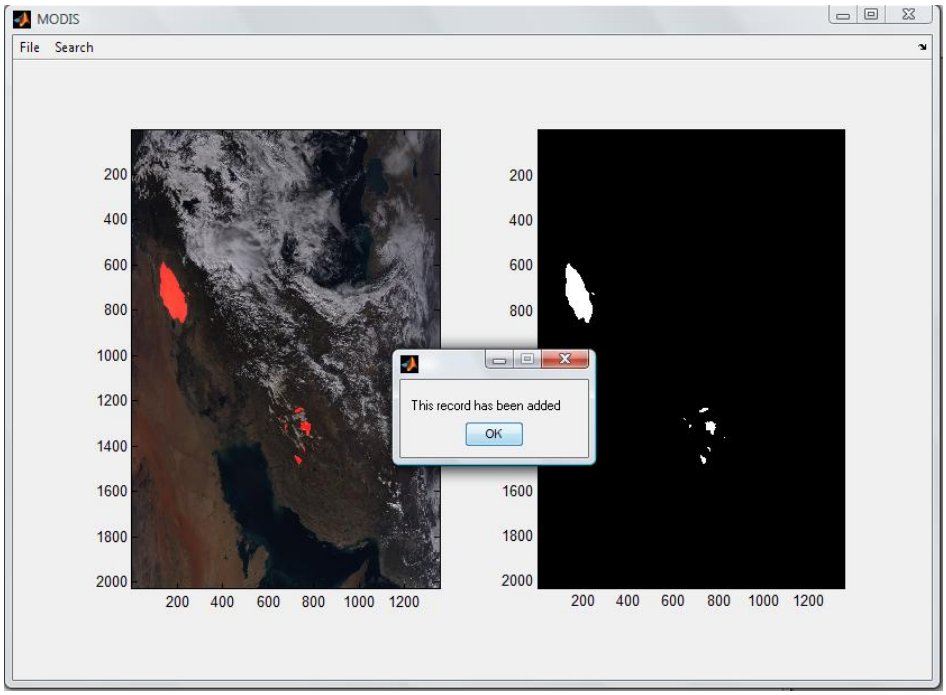

Figure 6-7 The result when new data are added.

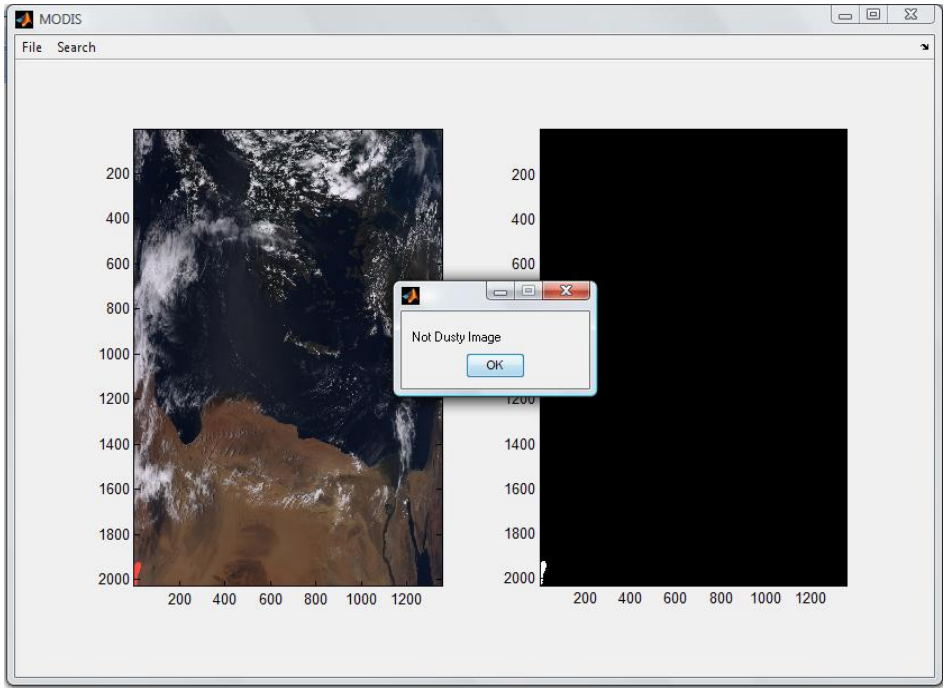

Figure 6-8 The result if there is insufficient dust storm evidence in the image.

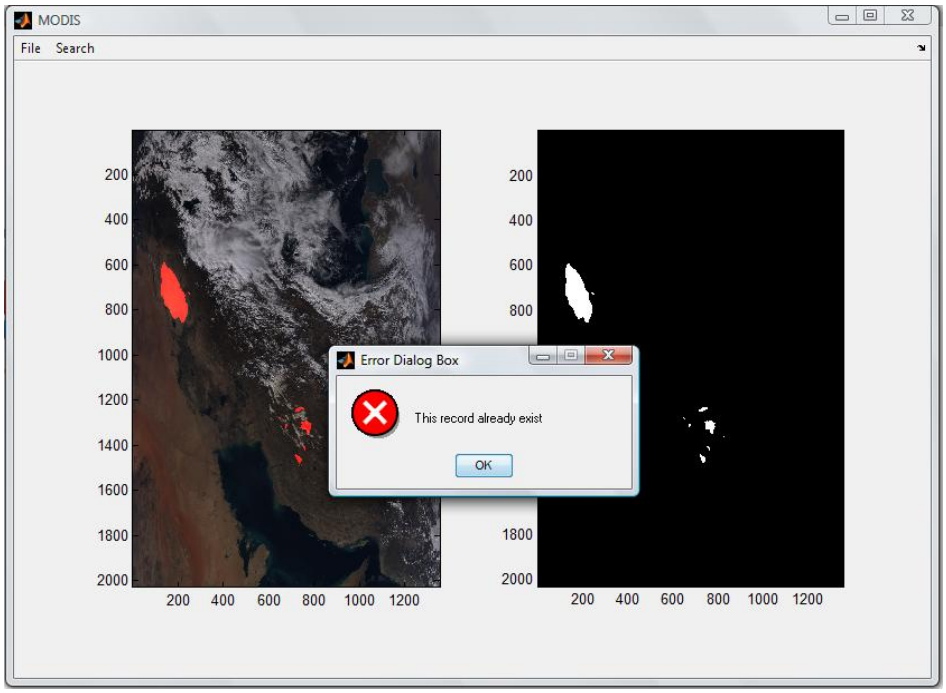

Figure 6-9 The result if the metadata of the image aleady exists

If the administrator clicks on the Clear Window menu item, or uses the keyboard shortcut Ctrl + C, the system will remove all the elements in the main interface window and the result will be as shown in Figure 6.3.

The system is closed down by clicking on the Exit menu item, or by using the keyboard shortcut Ctrl + E.

The second class of procedure available to the administrator is the metadata search function. Thus, if the administrator clicks on the Search menu, the menu items will apper as shown in Figure 6.10.

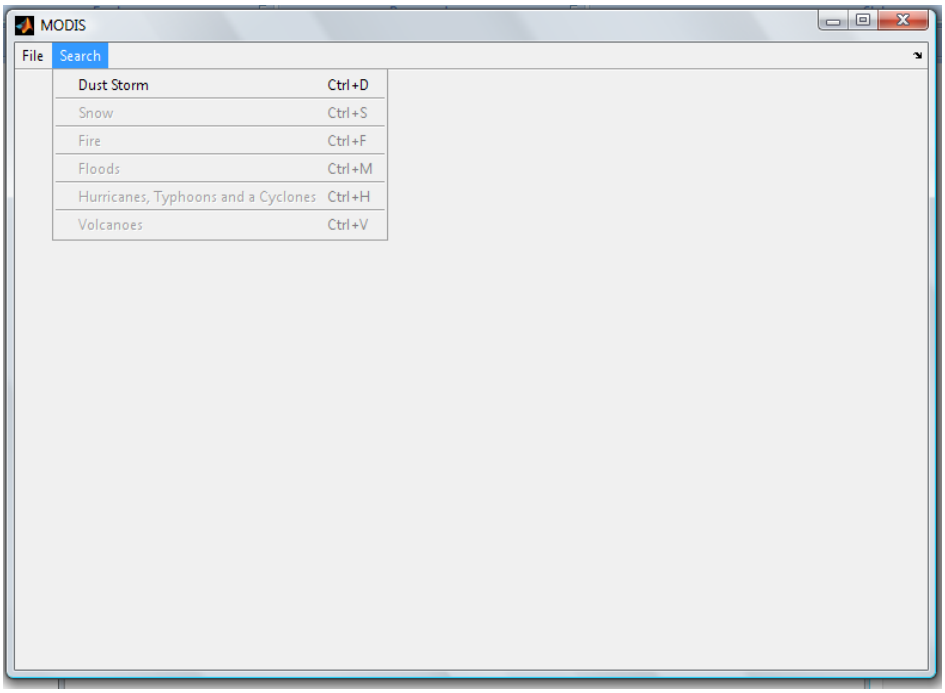

Figure 6-10 The Search menu of the administrator package interface

The search menu includes many items, however only the dust storm option is available currently. If the administrator selects this option, a search window will appear allowing the administrator to search through the dust storm database as shown in Figure 6.11.

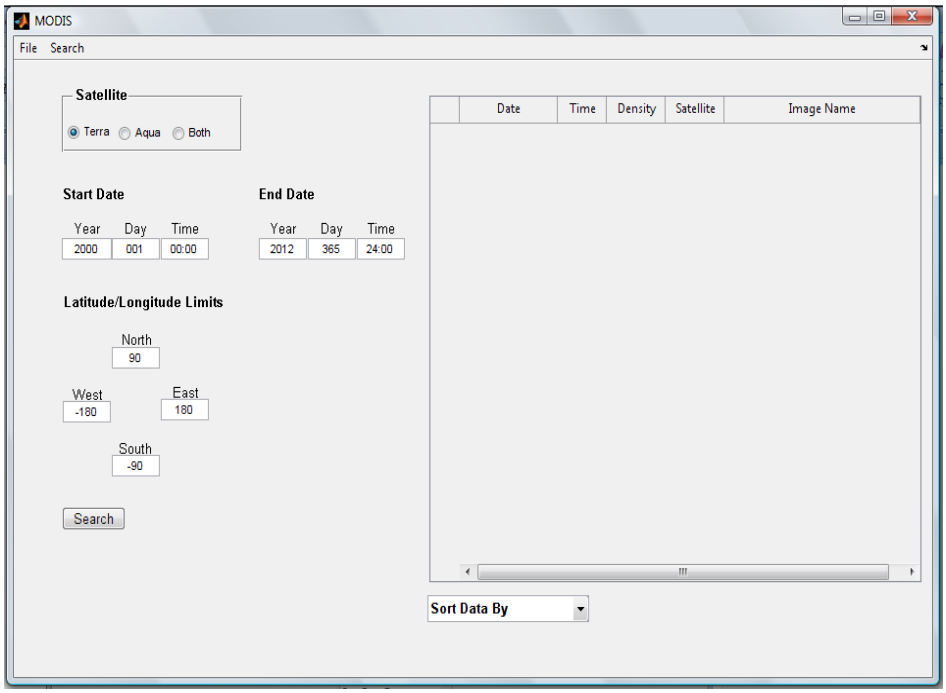

Figure 6-11 Database Searching window

From the database search window, the administrator is able to choose which satellite to display data (from Terra, Aqua or both), and to input the period of time for analysis. If one of these fields is left empty, or if a character is accidentally entered, then the system will display an error message as shown in Figure 6.12.

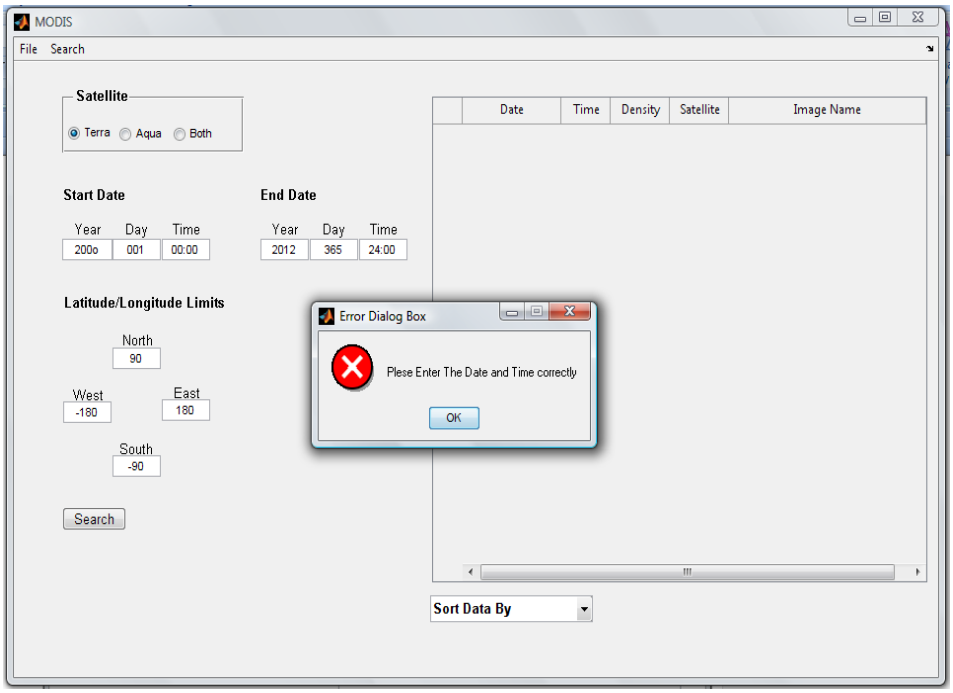

Figure 6-12 Error message caused by leaving text empty or entering a character

If the start date is after the end date, the administrator will receive an error message as shown in Figure 6.13.

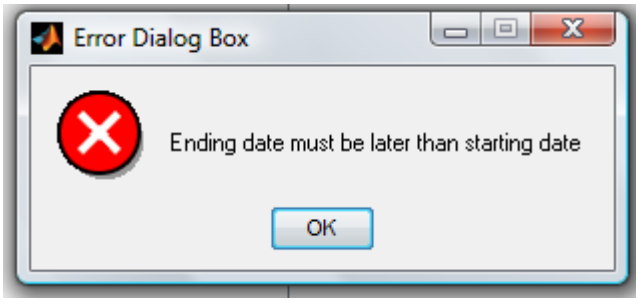

Figure 6-13 Error message when the start date is after the end date

If the administrator does not enter the date or the time in the correct format (for example, entering three digits in the year field instead of four) then an error message will appear as shown in Figure 6.14.

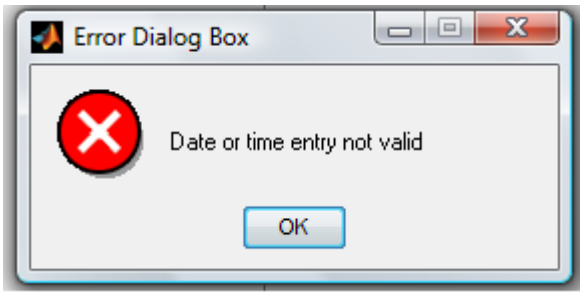

Figure 6-14 Error message caused by entering incorrect format for date or time

If the entered hours are fewer than 0 or greater than 24, the system will generate an error message as shown in Figure 6.15.

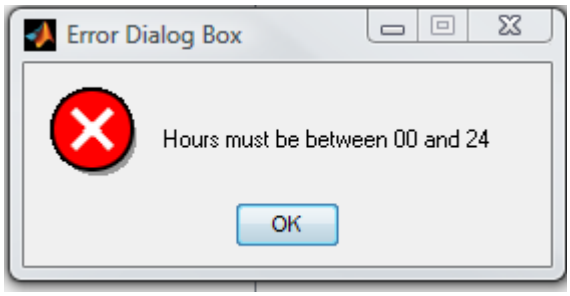

Figure 6-15 Error message caused by an incorrect hours format

If the entered minutes are fewer than 0 or greater than 60, the system will generate an error message as shown in Figure 6.16.

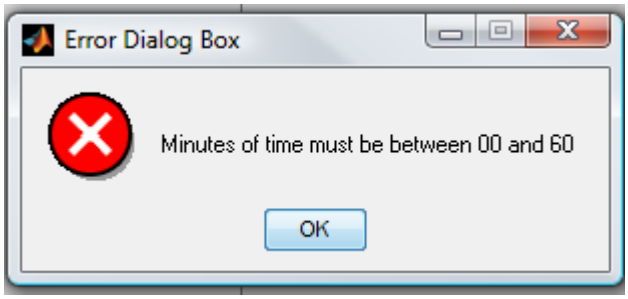

Figure 6-16 Error message caused by an incorrect minutes format

The latitude and the longitude of the search area are then input. If the search is global then the latitude is between -90 and 90 for south and north respectively and the longitude is between -180 and 180 for west and east respectively. If the inputs of the latitude and the longitude are outside of this

range, the administrator will receive one of the messages shown in figures 6.17 and 6.18.

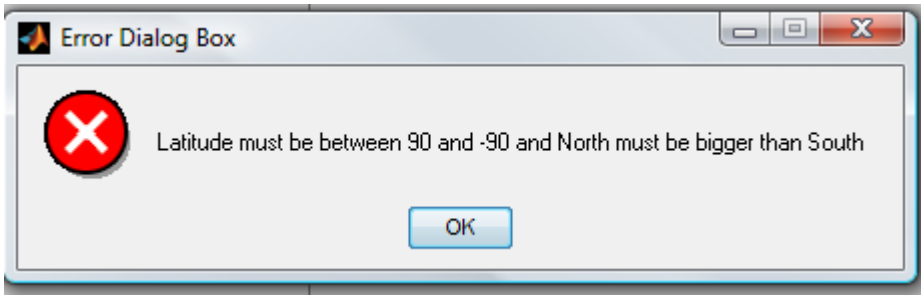

Figure 6-17 Error message caused by an incorrect Latitude value

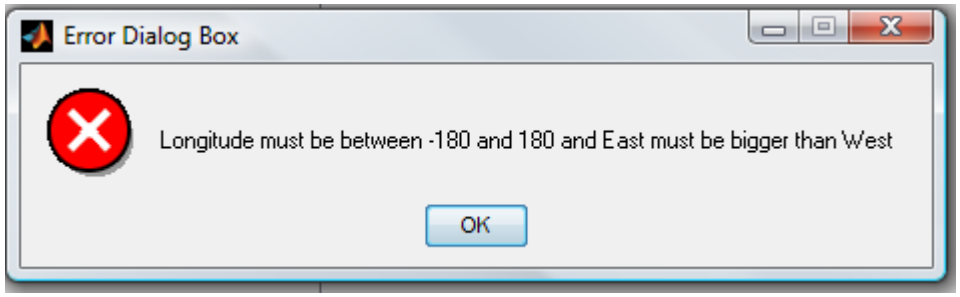

Figure 6-18 Error message caused by an incorrect Longitude value

If all required fields are entered correctly and the search push button is activated, the system will retrieve the required metadata from the database and the result will be as shown in Figure 6.19. The administrator can then choose to display the data by both date and time or by individual satellite or by the density of dust storm.

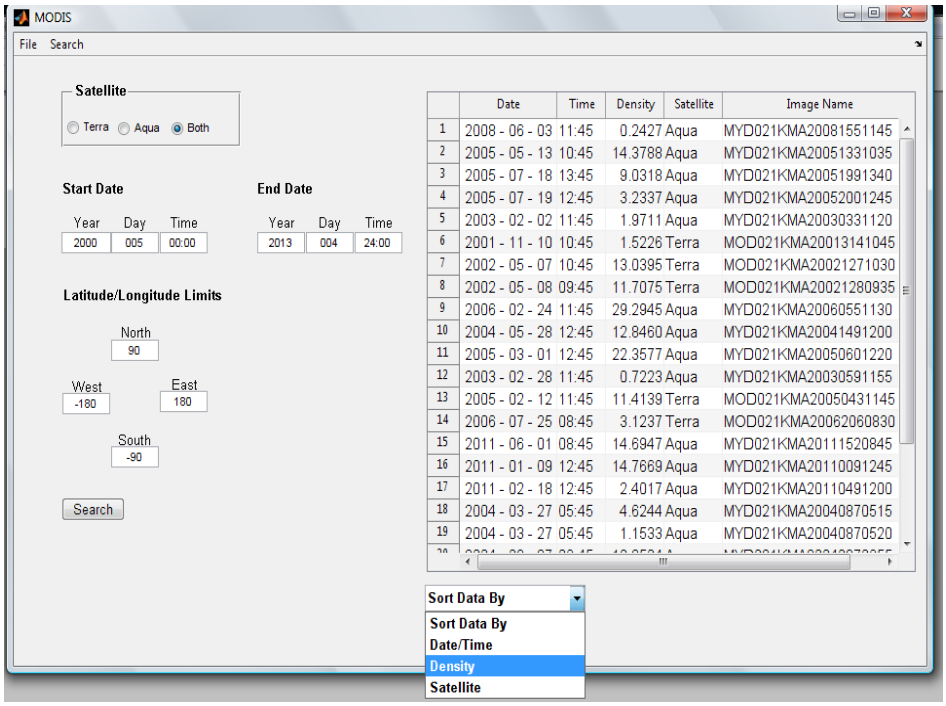

Figure 6-19 The system showing dust storm metadata retrieved from the database

6.4.2. USER PACKAGE

The user package behaves in the same manner as the administrator package, except that the user cannot load new data to the database. To ensure this, the Load File menu item is inactive. The user interface will be as shown in Figure 6.20.

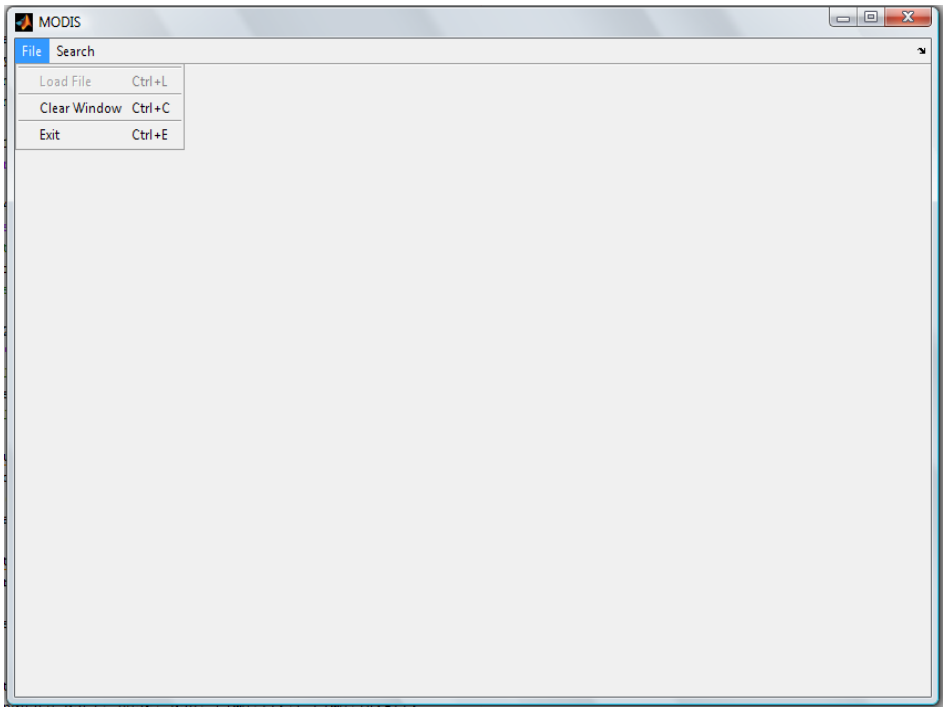

Figure 6-20 The file menu of the user package interface where the Load File menu item is not active

6.5 CHAPTER CONCLUSION

This chapter presents the author's automated system for dust storm detection from both day and night data, using a feed forward neural network. The feature vector used for pixel classification consists of the BT of band 31, together with the four BTDs (20-31), (23-31), (29-31) and (32-31). The system is able to detect the presence of dust storms from MODIS data and classify the MODIS images into categories containing dust data or not containing dust data. The automated system takes the form of two main packages. First is the administrator package, which has two primary functions: the extraction of the dust storms metadata from the MODIS data and the saving of this metadata in the database; the retrieval of the dust storm metadata from the database. The user package has only one primary function, the retrieval of dust storm metadata from the database.

CHAPTER SEVEN

7. CONCLUSIONS AND SUGGESTIONS FOR FURTHER WORK

7.1 INTRODUCTION

This thesis presents new algorithms for the efficient detection of dust storms and the classification of the contents of MODIS images. In addition an automatic system for updating a new dust storm database created by the author has been presented. Section 7.2 provides overall conclusions and Section 7.3 provides detailed summary and conclusions. Section 7.4 presents the main contributions to the field of dust storms detection. Suggestions for future work are given in Section 7.5.

7.2 OVERALL CONCLUSIONS

Since there was no efficient technique for dust storm detection over different ground surfaces, and there was limited availability of ground truth data that could be used for testing detection, monitoring and predicting dust storms, work addressing these concerns was conducted. The main achievements presented in this thesis are several new methods for automatic detection of dust storms, and a new system to generating a dust storm database using MODIS data. These made use of previous dust storm research and supporting previous highly developed technologies, including image processing and machine learning. The algorithms and techniques developed were implemented and

tested on many years of data from several geographical regions in order to assess the validity of the research results. Furthermore, since a decision tree classification technique is used by the MODIS team to generate the MODIS cloud mask product, a comparison has been made between using a decision tree and a neural network for classifying the contents of MODIS images into six classes.

The application and findings presented in this thesis are significant because the new algorithms are more effective compared to the previous ones and in detecting dust storms over different ground surfaces[69]. In addition, one of the techniques provides very good performance detecting dust storm at night. Also a real-time system for monitoring dust storms can be developed based on this work. Finally, the automated system of generating MODIS dust storm database could be the catalyst of further studies.

However, the work presented in this thesis still has some limitations. Weak dust storms over the water have not been detected properly and this work has not attempted to detect other important natural hazards such as fires, volcanoes, floods and other types of storms. Also this automated system is limited to tracking dust storms, and is limited to using MODIS data.

7.3 DETAILED CONCLUSION AND SUMMARY

In this thesis the major endeavour is related to the utilization, development and integration of different science aspects and technologies such as image processing, associated search algorithms, remote sensing and artificial intelligent concepts to design a new and optimized automated system that can detect dust storms from MODIS images globally, during both day and

night. The automatic dust storm detection using MODIS data was addressed by developing several algorithms and techniques after analysing the emissivities and the brightness temperatures of several MODIS image contents. Although all the methods developed provided good performances; the FFNN method using four BTDs and BT of band 31 provided the best performance for detecting dust storms during both day and night. Overall performance was shown to be superior to other published methods presented in this thesis. The novelty and biggest advantages of the new automated technique for dust storm detection, is that it can detect dust storms during the night in differing geographical regions and generate a MODIS dust storm database. However, the detection of dust storms during the night over water is still limited. For this reason more features could be added to improve the detection of dust storms over water and further, to include more natural hazards classes such as fire, smoke, floods, volcanoes, tornados, cyclones and hurricanes.

Finally, the adaptive thresholding technique should be compared with the global thresholds methods used in Chapter 3 to see if this would improve their results.

A detailed summary of this thesis chapter by chapter, including conclusions, is as follows.

- The aim of Chapter 2 is to assess the previous methods used for dust storms detection which used various instruments and satellite images. The chapter is divided to three main sections. Because much of the previous work uses MODIS data, the first section provides an overview of the MODIS instrument and its satellites, the properties of the MODIS data, the MODIS

products and applications provided and information on how to access this data. Information about previous studies on dust storm detection over different surfaces using different instruments is presented in the second section of this chapter. The third section provides information on previous studies on the classification of satellite images using different methods and concludes that the artificial neural network is an effective tool commonly used for classifying satellite images. The literature survey shows that a significant amount of previous work has investigated the detection of dust storms. However the achieved detection performances are still limited, as both dust storms and sandy lands share some characteristics, leading to difficulty in separating dust storms and sandy land. Dust storms also share some characteristics with low clouds and shadow which also leads to difficulty in separation. The detection of dust storms at night is still also limited due to low night-time temperatures, with all previous methods concentrating on using the BT for the detection of dust storms at the night. Moreover, there is no single method that is suitable for the detection of dust storms over different surfaces. For this reason more work is needed to improve the detection of dust storms, and to generate an automatic system that can be used for dust storm detection over different surfaces and during both day and night. Also, there are no ground truth data available that can be used for validation. The only way to provide ground truth data for dust storms is to use manual detection of dust storms.

- The aim of the work presented in Chapter 3 was to analyse the brightness temperature of MODIS image objects for generating the best brightness temperature difference to distinguish between dust storms and sandy land.

Two threshold methods have been used for dust storms detection. The first (in Section 3.2) uses the brightness temperature difference from bands 23 and 31, with Normalized Difference Dust Index. The BTD from bands 23 and 31 is used to distinguish dust storm with cloud from other surface content whereas the NDDI is used for distinguish between dust storm and cloud. The results show this method for dust storm detection is moderately effective but it can detect some low clouds and shadows as dust storm. Also this method is unable to detect weak dust storms over water or dust storms at night because of the use of the NDDI. The second method (in Section 3.3) uses BTDs from bands 23 and 31 and bands 31 and 32 with thresholds of 5.5K and 0K respectively. The results show that this method is much better than the first for detecting dust storms over land and sandy land by reducing the false detection of non-dust storm pixels. However, this method is also unable to detect dust storms reliably over water. The biggest advantage of this method is that it can detect dust storms at night. However, thresholds of -1K for both BTDs are needed to detect dust storm during the night, which are different to those used in the day. Thus, there is a need to improve the detection of dust storm over water and to develop an automated method that can detect dust storms over different surfaces and at both day and night.

- The aim of work presented in Chapter 4 was to explore the use the Artificial Feed-Forward Back-Propagation Neural Network for improved dust storm detection without relying on explicit thresholds. In this chapter two set of features have been used with an FFNN to classify dust storm pixels. The two BTDs from bands 23 and 31 and bands 31 and 32 and the reflectance

of the three bands 1, 3 and 4 have been used in the first method to generate the feature vector. The results show that this neural network is able to detect dust storms over different type of surfaces and is much better than the previous threshold methods for dust storm detection over different types of surface, but it is unable to detect dust storms at night because of the use of the reflectance bands. The second method was developed to detect dust storms at night by using the four BTDs from bands 20 and 31, bands 23 and 31, bands 29 and 31 and bands 31 and 32 and the BT from band 31 as the feature vector. This method was effective for detecting dust storms over different type of surface and during both day and night as well. The final work described in this chapter (in Section 4.4), used the second neural network and a set of thresholds on its output to generate a dust storm mask which indicates discrete probabilities of an image pixel being dust storm.

- The aim of the work presented in Chapter 5 was to make a comparison between the use of a decision tree (as chosen by the MODIS team for their cloud mask product) and an FFNN to classify MODIS images into six classes: cloud, dust storm, water, vegetation, land and snow. The features used in both methods include BTDs from bands 23 and 31 and bands 31 and 32 and NDDI, NDVI and NDSI. During training, both methods gave essentially the same performance, but when new data was used, the neural network was found to be more effective than the decision tree. Furthermore, both methods are much faster than waiting for the cloud mask results to become available. The neural network and decision tree are better than the cloud mask method for dust storm detection. A limitation of both methods

(decision tree and neural network) is that they can only be used during the day.

- The aim of the work presented in Chapter 6 was to generate an automated MODIS dust storm database system. This chapter describes an automated system for dust storms detection, from both day and night data, using the feed forward neural network. The feature vector used for pixel classification is the same as the second one in Chapter 4. The system managed to detect the dust storms from MODIS data and classify the content of MODIS images into dust or not-dust categories. The automated system consists of two main packages. First is the administrator package which has two primary functions. One is the extraction of dust storm metadata from the MODIS data and saving this metadata in the database. The second administrator function is the retrieval of metadata from the database. The user package has only one primary function, which allows the user to retrieve the metadata from the database.

7.4 CONTRIBUTIONS

A summary of the contributions presented in this thesis is as follows.

- Development of a new brightness temperature difference method using bands 23 and 31. This is effective in distinguishing between dust storms and sandy land.
- Development of a new algorithm for dust storm detection using the threshold method. The threshold method was implemented using the BTD from bands 23 and 31 and the NDDI. This algorithm was used to detect dust storms during the day.

- Development of a new dust storms detection algorithm using thresholds which is able to work during both day and night. This threshold algorithm used BTDs from bands 23 and 31 and bands 31 and 32.
- Development of a new dust storm detection method using a neural network classifier. This technique uses five features: BTDs from bands 23 and 31 and bands 31 and 32, and reflectance of bands 1, 3 and 4. This technique is very effective for the detection dust storms during the day but is unable detect dust storms during the night.
- Development of another new dust storm detection method using a neural network classifier. This technique is used five features: BTDs from bands 20 and 31, bands 23 and 31, bands 29 and 31 and bands 31 and 32 and the BT from band 31. This technique is very effective and better than the previous techniques for detection dust storms, and is able to detect dust storms during both day and night.
- Making a comparison between decision tree and neural network methods for classifying MODIS images. The neural network was much better than the decision tree when they were both applied to new data.
- Development of a new automated system for dust storms detection which generates a MODIS dust storm database. This automated system allows operation by either an administrator, who can build the database or a general user, who can only access the database.

7.5 SUGGESTIONS FOR FURTHER WORK

The research presented in this thesis provides a strong foundation for future work in the field of dust storms detection. The main suggestions for the future work are as follows.

- The neural network method used for dust storm, detection during day and night could be developed further by exploring the addition of more bands in the feature set to improve its ability to detect dust storms particularly over water. The use of a Cascade Correlation neural network could also be explored to improve the quality of dust storm detection.
- The method described in Section 4.3 for detecting dust storms could be used, together with data for wind direction and wind speed, to develop a new system for monitoring and tracking dust storms.
- The method described in Chapter 5 for classifying MODIS images could be developed further to include more classes such as fire, volcanic cloud, shadow and the cloud class itself could be divided into several sub-class levels. To do this, appropriate features to discriminate each of these new classes would have to be found.
- The database system described in Chapter 6 could be further developed to include other natural hazards such as fire, smoke, floods, volcanoes, tornados, cyclones and hurricanes. This would first require the completion of the previous suggestion.

REFERENCES

[1] J. J. Qu, *et al.*, "Asian Dust Storm Monitoring Combining Terra and Aqua MODIS SRB Measurements," *Geoscience and Remote Sensing Letters, IEEE,* vol. 3, pp. 484-486, 2006.

[2] S.-c. Liu, *et al.*, "Detection of Dust Storms by Using Daytime and Nighttime Multi-spectral MODIS Images," in *Geoscience and Remote Sensing Symposium, 2006. IGARSS 2006. IEEE International Conference on*, 2006, pp. 294-296.

[3] *Global alarm : dust and sandstorms from the world's drylands / supported by the Government of the Netherlands, Asia Regional Coordinating Unit Secretariat of the United Nations Convention to Combat Desertification ; [editors, Yang Youlin, Victor Squires and Lu Qi]*. Bangkok :: Asia RCU, UNCCD, 2002.

[4] Y. Shao and C. H. Dong, "A review on East Asian dust storm climate, modelling and monitoring," *Global and Planetary Change,* vol. 52, pp. 1-22, 2006.

[5] A. Slingo, *et al.*, "Observations of the impact of a major Saharan dust storm on the atmospheric radiation balance," *Geophysical Research Letters,* vol. 33, pp. n/a-n/a, 2006.

[6] A. S. Goudie, "Dust storms: Recent developments," *Journal of Environmental Management,* vol. 90, pp. 89-94, 2009.

[7] DI Mei, *et al.*, "A Dust Storm Process Dynamic Monitoring WIith Multi-Temporal MODIS Data," *The International Archives of the Photogrammetry, Remote Sensing and Spatial Information Sciences,* vol. XXXVII. Part B7, pp. 965-970, 2008.

[8] W. Kaiping, *et al.*, "Detection of Sand and Dust Storms from MERIS Image Using FE-Otsu Alogrithm," in *Bioinformatics and Biomedical Engineering, 2008. ICBBE 2008. The 2nd International Conference on*, 2008, pp. 3852-3855.

[9] T. Han, *et al.*, "Automatic detection of dust storm in the northwest of China using decision tree classifier based on MODIS visible bands data," in *Geoscience and Remote Sensing Symposium, 2005. IGARSS '05. Proceedings. 2005 IEEE International*, 2005, pp. 3603-3606.

[10] W. T. Preesan Rakwatin, and Yoshifumi Yasuoka, "IMPROVE PERFORMANCE OF AQUA BAND 6," in *Asian Conference on Remote Sensing (ACRS)*, 2006.

[11] Christopher O. Justice, *et al.*, "The Moderate Resolution Imaging Spectroradiometer (MODIS): land remote sensing for global change research," *IEEE Transactions on Geoscience and Remote Sensing,* vol. 36, pp. 1228-1249, July 1998 1998.

[12] S. Frazier. (Accessed on 23 April 2012). *MODIS Website*. Available: http://modis.gsfc.nasa.gov/about/

[13] E. Masuoka, *et al.*, "Key characteristics of MODIS data products," *Geoscience and Remote Sensing, IEEE Transactions on,* vol. 36, pp. 1313-1323, 1998.

[14] X. Xiaoxiong, *et al.*, "An overview of MODIS calibration and characterization and lessons learned," in *Geoscience and Remote Sensing Symposium,2009 IEEE International,IGARSS 2009*, 2009, pp. IV-17-IV-20.

[15] A. Savtchenko, *et al.*, "Terra and Aqua MODIS products available from NASA GES DAAC," *Advances in Space Research,* vol. 34, pp. 710-714, 2004.

[16] J. Xiong and K. Simpson. (1999, Accessed on 5 June 2013). *MODIS Calibration General Information* [GIF]. Available: http://mcst.gsfc.nasa.gov/calibration/information

[17] M. Nishihama., *et al.*, "MODIS Level 1A Earth Location: Algorithm Theoretical Basis Document Version 3.0," August 26 1997 1997.

[18] G. N.Toller*., et al.*, "MODIS Level 1B Product User's Guide For Level 1B Version 6.1.0 (Terra) and Version 6.1.1 (Aqua)," MODIS Characterization Support Team (MCST)2009.

[19] X. Xiong*, et al.*, "Status of the MODIS level 1B algorithms and calibration tables," in *Geoscience and Remote Sensing Symposium, 2005. IGARSS '05. Proceedings. 2005 IEEE International*, 2005, pp. 2231-2234.

[20] A. T. Isaacman*, et al.*, "MODIS Level 1B calibration and data products," in *Earth Observing Systems VIII*, San Diego, CA, USA, 2003, pp. 552-562.

[21] J. Koziana*, et al.*, "MODIS atmospheric data products at the Goddard Earth Sciences DAAC," in *Geoscience and Remote Sensing Symposium, 2001. IGARSS '01. IEEE 2001 International*, 2001, pp. 1708-1710 vol.4.

[22] M. D. King*, et al.*, "Cloud and aerosol properties, precipitable water, and profiles of temperature and water vapor from MODIS," *Geoscience and Remote Sensing, IEEE Transactions on,* vol. 41, pp. 442-458, 2003.

[23] K. I. Strabala, *MODIS cloud mask user's guide*. Madison, WI.: University of Wisconsin--Madison, 2005.

[24] N. Steven D.Miller, Monterey, CA; and T. F. Lee, "Desert dust storms as detected by Meteosat and SeaWiFS multispectral imagery," in *11th Conference on Satellite Meteorology and Oceanography*, 2001.

[25] J. Pat S. Chavez*, et al.*, "Monitoring dust storms and mapping landscape vulnerability to wind erosion using satellite and ground-based digital images," in *Using geospatial technologies to understand dryland dynamics*, 2002, pp. 1092-5481

[26] S. Janugani*, et al.*, "Directional analysis and filtering for dust storm detection in NOAA-AVHRR imagery," in *Proceedings of the society of photo-optical instrumentation engineers (SPIE)*, 2009, pp. 73341G–73341G-12.

[27] N. Iino*, et al.*, "Detection of Asian dust aerosols using meteorological satellite data and suspended particulate matter concentrations," *Atmospheric Environment,* vol. 38, pp. 6999-7008, 2004.

[28] J. K. Roskovensky and K. N. Liou, "Differentiating airborne dust from cirrus clouds using MODIS data," *Geophys. Res. Lett.,* vol. 32, p. L12809, 2005.

[29] N. Guo*, et al.*, "Quantitative identification dust and sand storm using MODIS data," in *Geoscience and Remote Sensing Symposium, 2005. IGARSS '05. Proceedings. 2005 IEEE International*, 2005, pp. 3630-3633.

[30] P. Zhang*, et al.*, "Identification and physical retrieval of dust storm using three MODIS thermal IR channels," *Global and Planetary Change,* vol. 52, pp. 197-206, 2006.

[31] D. P. Duda*, et al.*, "The Continuous Monitoring of Desert Dust using an Infrared-based Dust Detection and Retrieval Method," in *Remote Sensing of Clouds and Aerosols: Aerosols*, 2006.

[32] O. S. Hansell R, Liou K, Roskovensky J, Tsay S, Hsu C, Ji Q, "Simultaneous detection/separation of mineral dust and cirrus clouds using MODIS thermal infrared window data," *GEOPHYS RES LETT,* vol. 34, p. 5, 2007 Jun 9 2007.

[33] J. Huang*, et al.*, "Detection of Asia dust storms using multisensor satellite measurements," *Remote Sensing of Environment,* vol. 110, pp. 186-191, 2007.

[34] X. Hao and J. J. Qu, "Saharan dust storm detection using moderate resolution imaging spectroradiometer thermal infrared bands," *Journal of Applied Remote Sensing,* vol. 1, pp. 013510-9, 2007.

[35] Y.Gao and J.F.Mas, "A Comparison of the Performance of Pixel Based and Object Based Classifications over Images with Various Spatial Resolutions," *Medwell Online Journal of Earth Sciences,* vol. 2, pp. 27-35, 2008

[36] X. Li and W. Song, "Dust Storm Detection Based On MODIS Data " in *International Conference on Geo-spatial Solutions for Emergency Management and the 50th*

Anniversary of the Chinese Academy of Surveying and Mapping Beijing, China, 2009, pp. 169-172.

[37] L. Xiaojing*, et al.*, "Estimating the greatest dust storm in eastern Australia with MODIS satellite images," in *Geoscience and Remote Sensing Symposium (IGARSS), 2010 IEEE International*, 2010, pp. 1039-1042.

[38] P. Rivas-Perea*, et al.*, "Automatic Dust Storm Detection Based on Supervised Classification of Multispectral Data," in *Soft Computing for Recognition Based on Biometrics*. vol. 312, P. Melin*, et al.*, Eds., ed: Springer Berlin Heidelberg, 2010, pp. 443-454.

[39] L. Yang and L. Ronggao, "A thermal index from modis data for dust detection," in *Geoscience and Remote Sensing Symposium (IGARSS), 2011 IEEE International*, 2011, pp. 3783-3786.

[40] F. Yi-da*., et al.*, "The Analysis of Typical Dust Storm in Northern China Using Remote Sensing Data," *Advance in Earth Sciences,* vol. 17, pp. 289-294, 2002.

[41] H. El-Askary*, et al.*, "Introducing new approaches for dust storms detection using remote sensing technology," in *Geoscience and Remote Sensing Symposium, 2003. IGARSS '03. Proceedings. 2003 IEEE International*, 2003, pp. 2439-2441 vol.4.

[42] H. El-Askary*, et al.*, "Enhancing dust storm detection using PCA based data fusion," in *Geoscience and Remote Sensing Symposium, 2005. IGARSS '05. Proceedings. 2005 IEEE International*, 2005, pp. 1424-1427.

[43] H. El-Askary*, et al.*, "Dust storms detection over the Indo-Gangetic basin using multi sensor data," *Advances in Space Research,* vol. 37, pp. 728-733, 2006.

[44] A. T. EVAN*, et al.*, "Development of a new over-water Advanced Very High Resolution Radiometer dust detection algorithm," *International Journal of Remote Sensing,* vol. Vol. 27, pp. 3903–3924, 2006.

[45] I. Genkova*, et al.*, "Saharan dust motion extraction from MSG-SEVIRI," in *European Organization for the Exploitation of Meteorological Satellites (EUMETSAT), Darmstadt, Germany,*, 2008.

[46] B. Chen*, et al.*, "Detection of dust aerosol by combining CALIPSO active lidar and passive IIR measurements," *Atmospheric Chemistry and Physics,* vol. 10, pp. 4241-4251, 2010.

[47] M. Q. Alkhatib*, et al.*, "Automated detection of dust clouds and sources in NOAA-AVHRR satellite imagery," in *Image Analysis and Interpretation (SSIAI), 2012 IEEE Southwest Symposium on*, 2012, pp. 97-100.

[48] Aykut Akgün*, et al.*, "Comparing Different Satellite Image Classification Methods: An Application In Ayvalik District,Western Turkey," Istanbul, Turkey, 2004.

[49] R. Gamanya*, et al.*, "An automated satellite image classification design using object-oriented segmentation algorithms: A move towards standardization," *Expert Systems with Applications,* vol. 32, pp. 616-624, 2007.

[50] ZHONGDONG YANG*, et al.*, "High-Spatial-Resolution Surface and Cloud-Type Classification from MODIS Multispectral Band Measurements," *Journal of Applied Meteorology,* vol. 42, pp. 204-226, 2003.

[51] M. Nadir Kurnaz*, et al.*, "Segmentation of remote-sensing images by incremental neural network," *Pattern Recognition Letters,* vol. 26, pp. 1096-1104, 2005.

[52] Pooja A P*, et al.*, "Classification of RS data using Decision Tree Approach," *International Journal of Computer Applications,* vol. 23, pp. 7-11, 2011.

[53] P. S. a. L. Malathi, "Classification and Segmentation in Satellite Imagery Using Back Propagation Algorithm of ANN and K-Means Algorithm " *International Journal of Machine Learning and Computing,* vol. 1(4), pp. 422-426, 2011.

[54] J. Xiong. (Accessed on 5 June 2013). *How can I extract temperature from the L1B data product?* Available: http://mcst.gsfc.nasa.gov/forums/how-can-i-extract-temperature-l1b-data-product

[55] G. N.Toller, *et al.*, "MODIS Level 1B Product User's Guide For Level 1B Version 6.1.0 (Terra) and Version 6.1.1 (Aqua)," MODIS Characterization Support Team (MCST)2003.
[56] M. Chacon-Murguía, *et al.*, "Dust Storm Detection Using a Neural Network with Uncertainty and Ambiguity Output Analysis Pattern Recognition." vol. 6718, ed: Springer Berlin / Heidelberg, 2011, pp. 305-313.
[57] P. Picton, *Neural Networks*: Palgrave, 2000.
[58] S. S. Haykin, *Neural Networks and Learning Machines*: Pearson Education, 2008.
[59] S. Huang, *et al.*, *Neural network control: theory and applications*: Research Studies Press, 2004.
[60] D. K. Hall and B. Stees. (1999, Accessed on 13/06/2012). *MODIS Snow and Ice Global Mapping Project*. Available: http://modis-snow-ice.gsfc.nasa.gov/
[61] E. El-ossta, *et al.*, "A new Approach for the detection of Dust Storms Using Multi-spectral MODIS bands," presented at the Mosharaka International Conference on Communications, Computers and Applications Amman Jordan, 2009.
[62] Kokalj Ž, Oš, Tir K., "Land cover mapping using Landsat satellite image classification in the Classical Karst - Kras region," *Acta Carsologica,* vol. 36, pp. 433-440, 2007.
[63] M. S. Pang-Ning Tan, Vipin Kumar. (2006, Accessed on 30/09/2012). *Introduction to Data Mining*. Available: http://www-users.cs.umn.edu/~kumar/dmbook/index.php
[64] K. Xu, *et al.*, "Unsupervised Satellite Image Classification Using Markov Field Topic Model," *Geoscience and Remote Sensing Letters, IEEE,* vol. 10, pp. 130-134, 2013.
[65] A. Abdelhalim and I. Traore, "A New Method for Learning Decision Trees from Rules," in *Machine Learning and Applications, 2009. ICMLA '09. International Conference on*, 2009, pp. 693-698.
[66] S. Platnick, *et al.*, "The MODIS cloud products: algorithms and examples from Terra," *Geoscience and Remote Sensing, IEEE Transactions on,* vol. 41, pp. 459-473, 2003.
[67] V. V. Salomonson and I. Appel, "Development of the Aqua MODIS NDSI fractional snow cover algorithm and validation results," *Geoscience and Remote Sensing, IEEE Transactions on,* vol. 44, pp. 1747-1756, 2006.
[68] G. Ou and Y. L. Murphey, "Multi-class pattern classification using neural networks," *Pattern Recognition,* vol. 40, pp. 4-18, 2007.
[69] E. El-ossta, *et al.*, "Detection of Dust Storms Using MODIS Reflective and Emissive Bands," *Selected Topics in Applied Earth Observations and Remote Sensing, IEEE Journal of,* vol. PP, pp. 1-6, 2013.

APPENDIX A

1. OVERVIEW OF MODIS INSTRUMENT

The CD-ROM attached to this thesis contains useful information about MODIS instrument.

2. CODE OF AUTOMATED MODIS DUST STORM DATABASE SYSTEM

The CD-ROM also contains the code of dust storm detection and the automated MODIS dust storm database system.